The Design and Construction of an Active-Target Detector for the Study of the $^{20}Ne(\alpha,\alpha')^{20}Ne^*$ Reaction

by

Johann Wiggert Brümmer

Thesis presented in partial fulfilment of the requirements for the degree Master of Science in the Department of Physics at the University of Stellenbosch.

Department of Physics
University of Stellenbosch
Private Bag X1, Matieland 7602, South Africa

Supervisor: Prof. Paul Papka
Department of Physics
University of Stellenbosch

December 2015

Declaration

By submitting this thesis electronically, I declare that the entirety of the work contained therein is my own, original work, that I am the sole author thereof (save to the extent explicitly otherwise stated), that reproduction and publication thereof by Stellenbosch University will not infringe any third party rights and that I have not previously in its entirety or in part submitted it for obtaining any qualification.

December 2015

Abstract

The Design and Construction of an Active-Target Detector for the Study of the ^{20}Ne(α,α')^{20}Ne* Reaction

J.W. Brümmer

Department of Physics
University of Stellenbosch
Private Bag X1, Matieland 7602, South Africa

Thesis: MSc (Physics)

December 2015

The existence of an excited 3α resonant state in ^{12}C, which is crucial for the thermonuclear fusion of carbon in red giant stars, was predicted by Fred Hoyle in 1954. Since the experimental observation of the Hoyle state in 1957, studies have evolved to examine α-decay processes in other light nuclides such as ^{8}Be and ^{16}O. Populating α-cluster states and observation of the subsequent decay becomes difficult for α-conjugate nuclei heavier than ^{12}C. A study of ^{20}Ne carried out using the ^{22}Ne(p,t)^{20}Ne* reaction revealed a candidate for a 0^+ 5α state at 22.5 MeV known as the ^{20}Ne Hoyle analogue. The state is near the 5α decay threshold of 19.17 MeV. Characterising this state is non-trivial. The branching ratio of the decay path to the 5α channel is expected to be very low. An active-target detector was developed to study the break-up of the 5α state populated by the ^{20}Ne(α,α')^{20}Ne* reaction. It is designed to be a high-efficiency detector in order to measure reactions with low-energy reaction products and low cross sections. An active-target detector is a detector where the target also acts as the detection medium.

The Gaseous Active-TargEt Ancillary Unit (GATEAU) that was designed and built for this project is versatile; it has the potential to study clustering in other gas targets such as ^{16}O, ^{18}O, ^{21}Ne, ^{22}Ne and ^{36}Ar. It can also be used for the detection of low-energy particles decaying from astrophysically important resonances. Active-target detectors are generally used in the context of radioactive ion beams (RIBs) due to the characteristically low beam intensities and the nature of the reactions. The printed circuit board (PCB) of the detector has 5 sectors, each with 16 signal wires alternating with 17 guard wires. A high-voltage terminal opposite the PCB creates an electric field,

establishing an active detection region to detect drift electrons that result from decay particles moving through the active region.

An active-target detector was designed, built and successfully tested in order to study the 22.5-MeV 0^+ 5α cluster state in ^{20}Ne using the ^{20}Ne(α,α')^{20}Ne* reaction. Full kinematic track reconstruction is possible allowing determination of particle energies and positions in order to establish the interaction point within the gas cell. Over the past few years, the GATEAU detector has been developed and successfully tested with a ^{226}Ra α-particle source. A proposal for an in-beam test has been accepted by the iThemba LABS programme advisory committee (PAC). This will test the limits of the detector regarding background count rates and detection of low-energy α-particles. The (α,α') reaction will be used to look at states in ^{12}C, ^{16}O and ^{20}Ne.

Uittreksel

Die Ontwerp en Konstruksie van 'n Aktiewe-Teiken Detektor vir die Studie van die ^{20}Ne(α,α')^{20}Ne* Reaksie

J.W. Brümmer

Departement Fisika
Universiteit van Stellenbosch
Privaatsak X1, Matieland 7602, Suid-Afrika

Tesis: MSc (Fisika)

Desember 2015

Die bestaan van 'n opgewekte, 3α-groep toestand in ^{12}C, wat noodsaaklik is tydens die vervaardiging van koolstof in verouderde sterre, is deur Fred Hoyle in 1954 voorspel. Sedert die eksperimentele waarneming van die Hoyle toestand in 1957 het studies verder ontwikkel om ander α-groep toestande te ontdek in ^{8}Be en ^{16}O. Om α-groep toestande in nukliedes swaarder as ^{12}C op te wek en hul daaropvolgende verval waar te neem, is 'n uitdaging. 'n Studie van ^{20}Ne wat uitgevoer is met die ^{22}Ne(p,t)^{20}Ne* reaksie het 'n moontlike kandidaat vir die 0^+ 5α toestand by 22.5 MeV uitgewys. Hierdie toestand word na verwys as die ^{20}Ne Hoyle analoogtoestand. Die waargenome toestand is naby die 5α verval-drumpel van 19.17 MeV. Om hierdie toestand te karakteriseer is nie triviaal nie. 'n Aktiewe-teiken detektor is gevolglik ontwikkel om verval vanaf die 5α toestand, wat deur die ^{20}Ne(α,α')^{20}Ne* reaksie opgewek word, op te spoor. Die detektor is ontwerp om lae-energie verval deeltjies, wat 'n lae kansvlak het, te kan waarneem met 'n hoë effektiwiteit. Die term "aktiewe-teiken detektor" word omvattend gebruik om alle detektors te beskryf waar die gas teiken ook as die opsporingsmedium benut word.

Die Gaseous Active-TargEt Ancillary Unit (GATEAU) detektor wat vir die doel van hierdie projek ontwerp en gebou is, is veelsydig aangesien dit ook die vermoë het om groep toestande in verskeie ander nukliedes te bestudeer, byvoorbeeld ^{16}O, ^{18}O, ^{21}Ne, ^{22}Ne en ^{36}Ar. Dit kan ook gebruik word in die deteksie van lae-energie deeltjies wat uit toestande verval wat belangrik is in astrofisika studies. Aktiewe-teiken detektors word dikwels benut vir studies wat RIB bundels gebruik as gevolg van die lae-energie aard van die vervaldeeltjies en die lae energie van RIB bundels. Die detektor se stroombaan

bord bestaan uit vyf sektore, elk met 16 seindrade wat afgewissel word met 17 hoogspanningsdrade. ‘n Hoogspanningsterminaal teenoor die stroombaan bord fasiliteer ‘n elektriese hoogspanningsveld. Hierdie area staan bekend as die aktiewe area. Dit word gebruik om elektrone op te spoor deur die vervaardiging van elektron-ioon pare soos verval deeltjies deur die detektor se gas en elektriese veld beweeg.

Volledige rekonstruksie van die kinematika van die α-deeltjie spore kan gedoen word om sodoende elke deeltjie se energie en interaksie punt vas te stel. Gedurende die afgelope paar jaar is die GATEAU detektor ontwerp en suksesvol getoets met ‘n ^{226}Ra α-deeltjie bron. ‘n Voorlegging aan die iThemba LABS program aanbevelings-komitee is gedoen en bundel tyd is toegeken om die detektor te toets met ‘n 200-MeV α-bundel. Die bundel tyd sal gebruik word om GATEAU se lae-energie deteksie vermoë te bepaal. Die (α,α’) reaksie sal ook benut word om verskeie opgewekte toestande in ^{12}C, ^{16}O en ^{20}Ne te bestudeer.

Acknowledgements

With your permission, the author will use the first-person personal pronoun for this section in order to personally address and thank those that have dedicated their time and effort towards this project.

A project of this nature is not completed without assistance. Many people have contributed to this study and have my sincere gratitude in helping me complete a very interesting study. First and foremost, I would like to acknowledge the extraordinary input from Professor Paul Papka whom I am grateful and proud to call my supervisor. I would like to thank him for his continued patience, support and enthusiasm. It has always been a great pleasure to work with him as there has been lots of laughter and fun along the way ☺. The next few years as a PhD student with him as my supervisor will most certainly be memorable.

I am forevermore indebted to the knowledgeable Dr Philip Adsley. His contributions toward this thesis, the GATEAU in-beam sort code and my general edification have been incalculable. A big thank you to the captain of the K600 team, Dr Retief Neveling, who has helped with the TRACK and Garfield simulations as well as helping me understand the mystical and wonderful ways of the K600 magnetic spectrometer.

I am thankful to the additional collaborators and K600 team members, namely Drs Smit, Pellegri, Marín-Lámbarri and Pesudo and Mr. Kevin Li for having me as part of the team. Thanks to Zaid Dyers, Gerhard Louwrens, Christo van Tubbergh and everyone at the iThemba LABS workshop that supplied me with the necessary equipment to complete the detector build.

Thanks to iThemba LABS and the Stellenbosch University physics department for providing me with unequalled access to scientific journals and the opportunity to study such an interesting field at world-class establishments. I also acknowledge and greatly appreciate the sustained financial contributions and support from SANHARP and the NRF.

Most importantly, I would like to express my deepest gratitude to my parents Danie and Lynette, my sister Suné and my beloved pet Liefie for their everlasting support and unconditional love.

"When I went to school, they asked me what I
wanted to be when I grew up.
I wrote down "happy".
They told me I didn't understand the assignment
and I told them they didn't understand life."

John Lennon

Contents

List of Figures

List of Tables

Chapter 1
Scientific Motivation

Ipsa scientia potestas est.
Knowledge itself is power.

Sir Francis Bacon - *Meditationes Sacrae*

The phenomenon of α-particle clustering exists, in particular, in light, N = 4n (α-conjugate) nuclei that lie on the N = Z line of stability in the chart of nuclides. The ^{4}He nucleus is informally known as an α-particle. It has two protons and two neutrons that form shell closures in the $1s_{1/2}$ neutron and proton orbitals. The result is that the ^{4}He nucleus is doubly magic and consequently very stable and relatively inert. It has a high binding energy (BE) per nucleon of ~7.0 MeV [1] which is the primary reason for the existence of α-clustering in light nuclides and α-particle decay in heavy nuclides.

The study of α-cluster states and α-conjugate nuclei became a prominent field of interest in nuclear physics upon the observation of the Hoyle state in 1957 [2]. The discovery was made three years after its existence had been predicted by Sir Fred Hoyle in 1954 [3]. The famous Hoyle state is the 0_2^+ 3α state in ^{12}C. This particular state is anthropically relevant as it facilitates the production of ^{12}C in red giant stars. ^{12}C forms via a two-step process referred to as the 3α reaction [4].

$$^{4}\text{He} + {}^{4}\text{He} \rightleftharpoons {}^{8}\text{Be}\ (+93.7 \pm 0.9\ \text{keV})$$

$$^{8}\text{Be} + {}^{4}\text{He} \rightleftharpoons {}^{12}\text{C}^{*} \rightarrow {}^{12}\text{C}+\gamma\ (+278 \pm 4\ \text{keV})$$

$$\therefore\ {}^{4}\text{He} + {}^{4}\text{He} + {}^{4}\text{He} \rightleftharpoons {}^{12}\text{C}^{*} \longrightarrow {}^{12}\text{C}+\gamma\ (+372 \pm 4\ \text{keV}).$$

The 3α reaction occurs late in the life cycle of aging, red giant stars as supplies of hydrogen are depleted and helium becomes the prevalent isotope within the core of the star. The 4α and 5α radiative capture reactions become a possibility as the stellar core temperature and density increases [5]. These processes take place via (α,γ) reactions in ^{12}C(α,γ)^{16}O and ^{16}O(α,γ)^{20}Ne [6] and exploit the 4α and 5α states in ^{16}O and ^{20}Ne,

respectively. The existence of these particular cluster states is consequently important given that they act as pathways to produce the heavier elements that are vital to life.

The 5α ^{20}Ne state has been theoretically predicted to exist near its corresponding decay threshold at 19.17 MeV [7]. The Ikeda diagram is shown in Figure 1.1 and illustrates the corresponding decay thresholds for various α-cluster states in N = 4n, α-conjugate nuclei. The 5α state has orbital angular momentum and nuclear parity $J^{\pi} = 0^{+}$. Populating and detecting 5α decay from the candidate 22.5-MeV state is non-trivial. Previous studies have probed this Hoyle analogue only to encounter difficulties in the detection of all five α-particles [8].

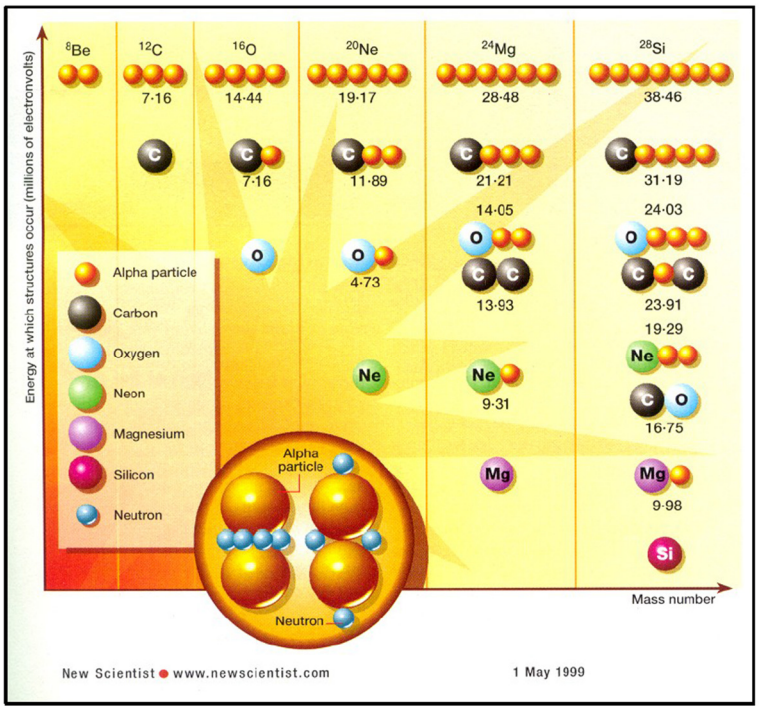

Figure 1.1: Ikeda diagram of N = 4n nuclides [7, 9]. The decay threshold (given in MeV) for α-conjugate nuclei is often located near the corresponding α state. The diagram can be extended to include ^{32}S, ^{36}Ar and ^{40}Ca. However, the α-cluster structures for these nuclides remain largely unknown.

Studies have examined the α-cluster states for ^{8}Be, ^{12}C and ^{16}O. However, the α structure of heavier N = 4n nuclides remains largely unknown. Heavier nuclides including ^{32}S, ^{36}Ar and ^{40}Ca may have α-cluster structures. However, it becomes increasingly difficult to experimentally investigate states around ever higher threshold energies since more decay channels become open.

During 2012 experiment PR196 was conducted at iThemba LABS to probe the nuclear structure of ^{20}Ne in order to search for low-spin states above the 5α break-up threshold. The experiment used the ^{22}Ne(p,t)^{20}Ne* reaction. In doing so, it populated a variety of states including T = 0, 1, 2 isospin states. Consequently, the study discovered six narrow, low-spin states at high excitation energies which are indicated in blue in Figure 1.2 [10, 11].

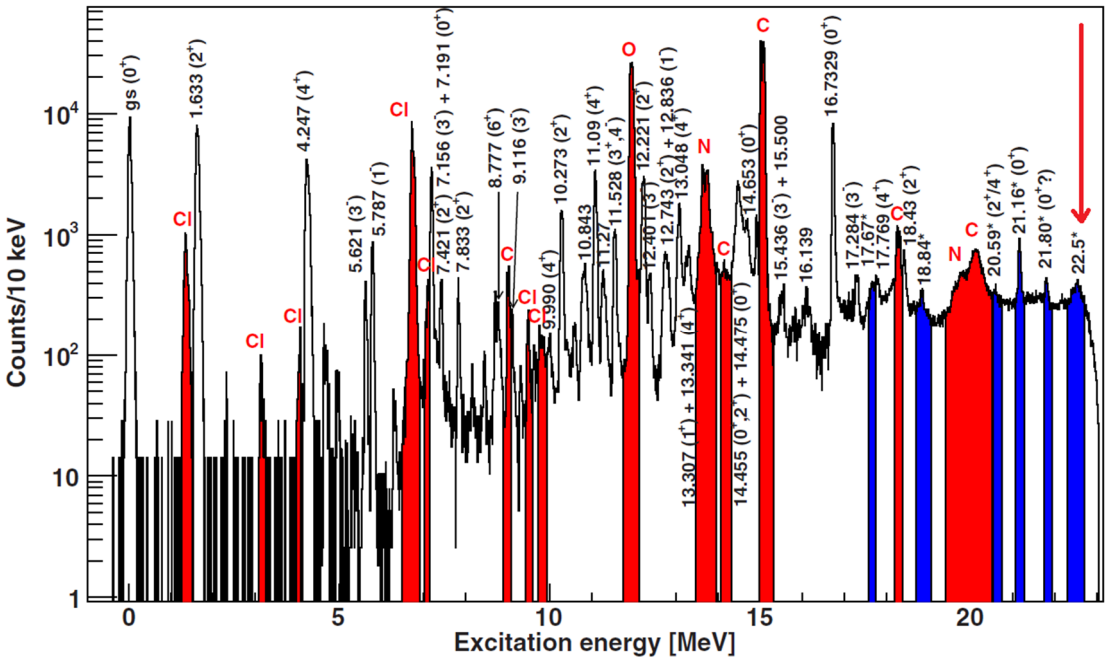

Figure 1.2: Excitation energy spectrum of ^{20}Ne from the ^{22}Ne(p,t)^{20}Ne* reaction [10, 11]. Contaminant states, that were introduced due to the 6-µm thick Aramid ($C_{14}O_2N_2Cl_2H_8$) windows of the gas cell, are indicated in red.

A candidate for the 5α cluster state was identified at 22.5 MeV, indicated by the red arrow in Figure 1.2. Five of the six discovered states could be interpreted using the Shell Model (SM). However, the SM was unable to interpret the state located at 22.5 MeV. Given the known limitations of the SM and its inability to accurately predict clustering in nuclei [12], the peak at 22.5 MeV was classified as a possible candidate for the 5α ^{20}Ne Hoyle analogue [10]. The general necessity of renormalization within the SM leads it to underestimate the short range interactions between nucleons; it is, therefore, not entirely suitable for the prediction of clustering in nuclei [12]. However, calculations performed with antisymmetrized molecular dynamics (AMD) [13, 14] and fermionic molecular dynamics (FMD) [15] have been successful in predicting clustering in light nuclei, including ^{20}Ne.

The ground state of ^{20}Ne is prolate. Moreover, the ground-state structure resembles that of a quadrupole ellipsoid [16]. This type of deformation creates conditions that are conducive to clustering. The reason for this is due to the closed shell of neutrons and protons of the constituent clusters. The Ikeda diagram shows that ^{20}Ne has the lowest threshold energy for single α-particle clustering. The reason is that the constituent nuclei, ^{16}O and ^{4}He, are both doubly magic. As stated previously, ^{4}He has a double magic nuclear configuration and this is also true for ^{16}O. The ^{16}O nucleus has 2+4+2 neutrons and 2+4+2 protons forming shell closures within the $1s_{1/2}$, $1p_{3/2}$ and $1p_{1/2}$ orbitals. Degeneracies that occur at filled nuclear orbitals give rise to conditions that are favourable for clustering and have been verified by AMD and FMD calculations [13, 14, 15]. The ^{20}Ne nucleus is therefore often regarded as the best example of clustering

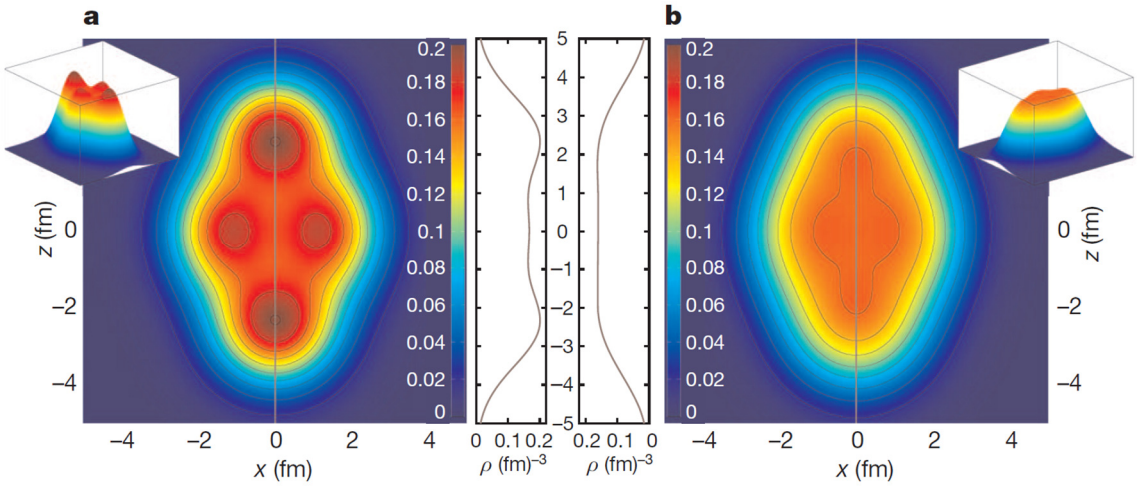

Figure 1.3: Energy-density functionals (EDFs) of the ^{20}Ne ground state [18]. The right-hand side image was produced using the Skyrme model and the left-hand side image was produced using the DD-ME2 models [18]. The density is given in units of fm^{-3}.

in light nuclei [17]. The deformation can be viewed in light of energy-density functionals (EDFs) as shown in Figure 1.3. It clearly shows the quadrupole-ellipsoid nature of the ground state.

Experiment PR231 was conducted in October 2014 at the iThemba LABS K600 magnetic spectrometer to investigate the ^{20}Ne* → ^{16}O + α decay via the ^{20}Ne(α,α') reaction. The experiment used an internal ^{20}Ne gas cell with the scattering chamber to mount four ancillary silicon detectors. Four, W1-type Double Sided Silicon Strip Detectors (DSSSDs) were used. However, DSSSDs are not suited for reaction products with a low-energy threshold like the 5α state. The reason is that the decay α-particles had to travel through the ^{20}Ne gas target and the dead layer of the silicon detectors for PR231. This experiment also highlighted why a specialised ancillary detector and gas cell is necessary for exotic, low-energy decays. Alpha particles decaying from the candidate 22.5-MeV state are expected to have a mean energy of ~650 keV given a 19.17-MeV decay threshold [7].

This thesis can be seen as a deviation from typical studies since it is purely concerned with the active-target detector development and the accompanying aspects thereof. The Gaseous Active-TargEt Ancillary Unit (GATEAU) is the detector system that was designed and built for this project. An active-target detector is a detector where the target also acts as the detection medium. Previous active-target detectors were investigated at the outset of this study to understand the typical methods used to design and construct this type of detector and to understand problems that may typically occur. The nature of the reaction in question was investigated to determine the detection capabilities that GATEAU has to possess in order to successfully detect, classify and characterise the 5α state. This led to a problem-specific design of the detector system. Subsequent simulations were used to test the feasibility thereof. Necessary alterations were made to the detector concept and the design of various components were finalised.

The principle of time projection chambers (TPCs) as they are applied to active-target detectors is well-suited to do charged particle spectroscopy with low-energy resolution. Active-target detectors are an ideal experimental tool to address the low cross section and low-energy reaction products encountered when studying the $^{20}Ne(\alpha,\alpha')^{20}Ne^*$ reaction. Successfully classifying the 22.5-MeV state will lead to the search for α-cluster states being extended to ^{36}Ar with GATEAU.

An active-target detector was designed, built and successfully tested in order to study the 22.5-MeV 0^+ 5α cluster state in ^{20}Ne. The detector will be used to probe the 5α state and completely characterise the nature thereof. The principle of time projection chambers have been investigated and various active-target detectors will be discussed and compared. The thesis will discuss the simulations used to probe the feasibility of the task at hand and the methods used to execute the detector build. Finally, the initial detector tests will be examined and discussed along with the upcoming in-beam run and possible future experiments.

Chapter 2
Introduction to Time Projection Chambers and Active Targets

"No man should escape our universities without knowing how little he knows."

J. Robert Oppenheimer

The principle of time projection chambers has been applied to active-target detectors for the past decade. It has enabled the study of nuclear reactions under severely limiting constraints with regards to cross section and low-energy reaction products. The time projection chamber (TPC) principle will be discussed along with its relation to active-target detectors. Furthermore, past implementations of these experimental techniques will be investigated as well as how they can be used to solve the problem at hand.

2.1 The Time Projection Chamber Principle

The Gaseous Active-TargEt Ancillary Unit (GATEAU) can simultaneously be regarded as a time projection chamber (TPC) and active-target detector. Active-target detectors are an extension of TPCs. This can be achieved by using the detection gas as the target as well. GATEAU has the ability to reconstruct particle tracks as ionising radiation passes through the detection medium for full kinematic reconstruction. The detection medium is always a gas in the case of TPCs as signals originate from the movement of charged particles through the gaseous medium. The basic principle of TPCs is illustrated in Figure 2.1.

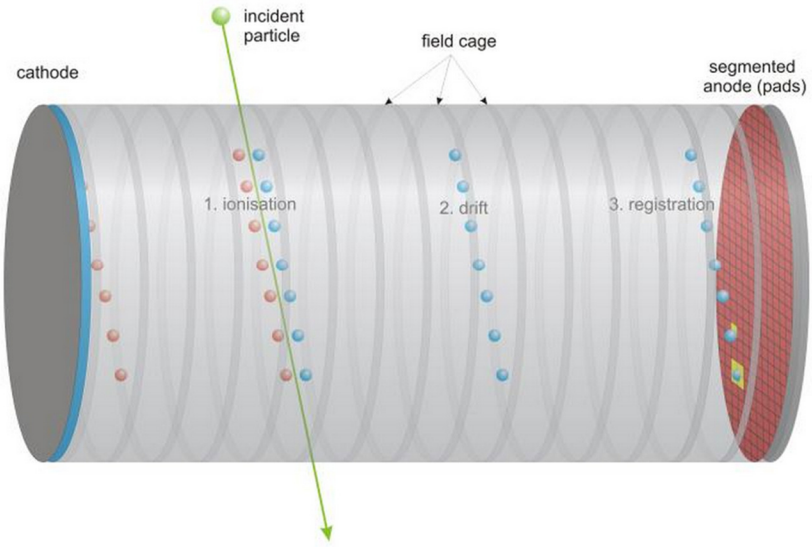

Figure 2.1: Illustration of the basic principle of a TPC [19]. The ALICE detector at CERN, which has a TPC detector component amongst others, is a well-known example [20]. Ionisation, drift and signal registration forms part of the general sequence of a TPC event.

A standard TPC has four fundamental features: detection gas, a segmented detection anode, a field cage and a high-voltage (HV) cathode. The cathode is placed opposite to the anode to establish a net electric field. Both typically have similar geometrical and design features which are necessary in order to have a homogeneous electric field between the two components. Electric field homogeneity is an important feature of TPCs so that particle tracks may be replicated accurately. The field cage consists of multiple charged wires around the electric field boundary. Hence, the detection region of the TPC is the gas-filled area that is enclosed by the field cage, anode and cathode. The anode is segmented for the purpose of position sensitivity in order to reconstruct the particle track [21].

A standard TPC event occurs when ionising radiation passes through the detection medium and interacts electromagnetically with the gas. Primary ionisation, in the form of ion pairs, is created along the particle path and start to separate due to the electric field. Drift electrons will start to move toward the anode and are detected as they avalanche near it. The slope of the particle track implies that the different drift electrons will have variable distances to travel to the anode depending on their position along the particle track and will therefore be detected at different times. The particle track within the chamber is therefore projected in time onto the anode. Standard TPCs used in nuclear physics perform optimally when detecting heavy charged particles such as fission fragments and other heavy nuclides given that they possess the greatest ability to ionise the detection gas [22].

A TPC can either be an avalanche detector or a proportional counter depending on the type of segmented anode that is used. GATEAU will use the principle of electron avalanche since drift electrons will accelerate under influence of the electric field as they approach the wire-structure PCB. The acceleration will cause an ever greater

amount of electrons to be liberated from their atomic orbitals through multiple collisions. The electric field strength is roughly constant throughout a TPC chamber except near the wire-structure where the electric field strength increases quickly as it is proportional to 1/r. This is the primary reason that electron avalanching occurs within a few radii of the anode signal wires. In contrast, proportional counters relate the signal that is detected to the amount of charge that is deposited, which in turn is related to the particle energy. Silicon detectors are a well-known example of this phenomenon. In general, ionisation chambers can also be used as proportional counters and are often implemented in δE-E telescopes.

Precise reconstruction of particle trajectories through the TPC is needed to identify them and their associated momenta. Particle momentum is inferred from the shape of the reconstructed tracks in the presence of a magnetic field. The segmented anode can only reconstruct the particle track on the basis of the detection points. A certain number of points are therefore needed to constitute a track. A reconstructed path is then fitted to the points on the basis of collinearity, assuming a homogeneous drift field. In the case where a particle beam passes through the TPC the track is extrapolated to intersect the beam path. The locus of the nuclear interaction point is determined in this way.

A specific particle momentum and identity will give rise to a specific ionisation density in the detection medium. The ion pairs of the particle track will move at a constant velocity to the anode, assuming that the electric field is constant and homogeneous between the anode and cathode. Ionisation energy loss per unit distance should be considered when particle identification is done. The ionisation density and energy that particles lose in the detection gas also serves as an identifier. It is evident that a highly homogeneous electric field has to exist to identify particles and accurately determine their energy. Steps were taken to ensure that this is true for GATEAU and these developments are discussed throughout chapter 6.

Another element that some TPCs have, which is not included in Figure 2.1, is a Frisch grid. The use of a Frisch grid is illustrated in the MAYA detector schematic of Figure 2.13. Frisch grids are implemented in order to eliminate induced currents in the detector anode caused by the movement of charge through the detection medium, between the HV cathode plane and the segmented anode [21]. A Frisch grid is typically made of a conductive material and takes the form of a metal grid. It is generally kept at a fixed potential or grounded and placed close to the anode. Charge moving between the cathode and grid is not able to induce a current in the anode thus eliminating the possibility of fictitious signals. Only the electrons that are able to pass through the grid will generate a signal [22]. Another advantage is that signals of a better quality are produced. The GATEAU standalone test (see section 6.1) did not include the use of a Frisch grid. The GATEAU signals result from avalanching. The effect of moving charge is therefore not seen until the drift electrons are close to the anode and starts to avalanche. This eliminates the need for a Frisch grid.

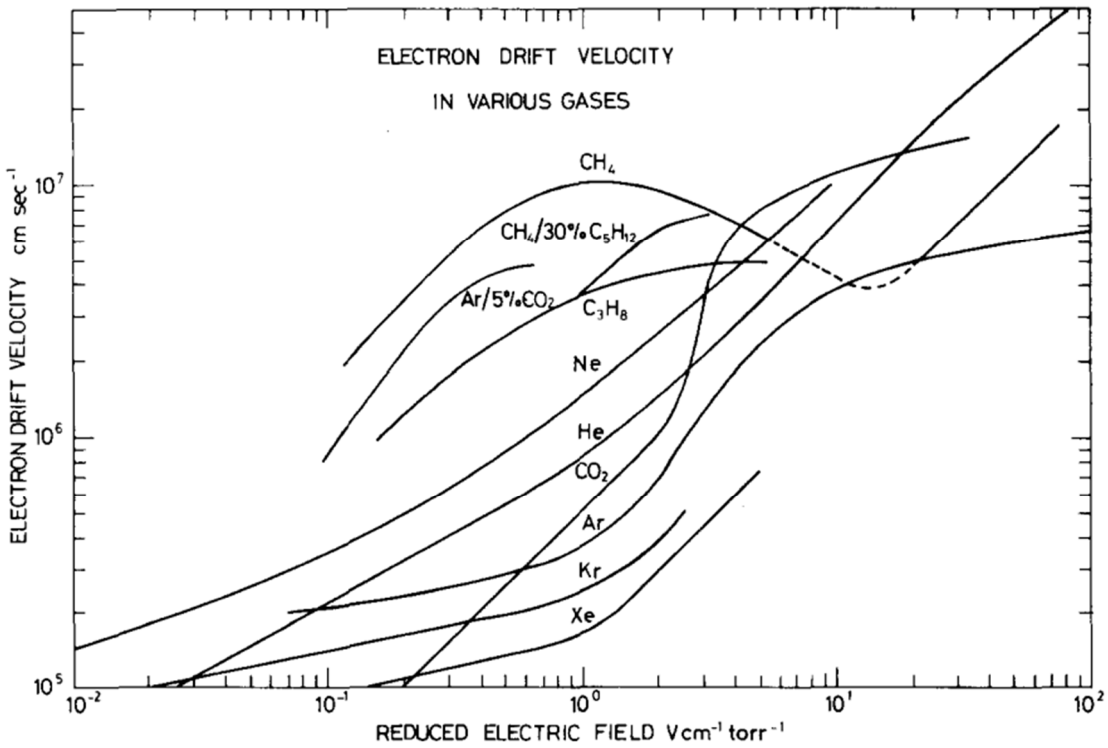

Figure 2.2: Electron drift velocities for various gasses and gas mixtures. An increase in electric field causes the electron drift velocity to increase with the exception of a few that reach saturation. The standalone detector test used an Ar/CO_2 mixture whereas in-beam runs will use a Ne/CO_2 mixture.

Two important parameters of the TPC gas are the electron drift and diffusion. Each gas species will have a characteristic electron drift velocity and diffusion coefficient. Diffusion is governed by the random, thermal motion of electrons in the gas. Electron drift velocities are governed by various parameters including the temperature and reduced electric field, i.e. v_{drift} is proportional to the ratio between electric field strength and gas pressure (E/p) [22]. The drift velocity is pressure dependent since the pressure dictates the time between ionisation collisions. Drift velocities are constant at a fixed reduced electric field except near the detection anode where electron acceleration and avalanching occurs.

Figure 2.3 to Figure 2.5 illustrate variations in drift velocity and gaseous diffusion for different Ne/CO_2 compositions [23] at 50 mbar. The variation of drift velocity with temperature is shown in Figure 2.6 specifically for the 90% Ne to 10% CO_2 case [24]. A mixture of 90% Ne to 10% CO_2 has been used as standard in various TPC detectors that use neon as a detection gas, such as ALICE. This fact, along with data from the graphs in Figure 2.3 to Figure 2.6, justifies quenching the in-beam neon target for GATEAU with 10% CO_2 (the quenching effect is explained in section 3.1). During the standalone GATEAU tests (see section 6.1.1), it was found that an electrical field of up to 600 V/cm could be maintained at in-beam gas pressures of 20-50 mbar without electrical discharge.

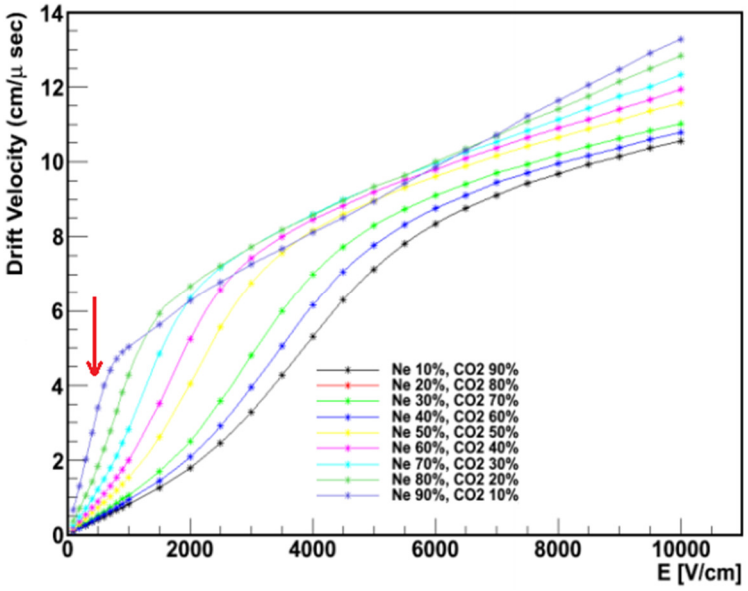

Figure 2.3: Dirft-velocity graph for various Ne/CO_2 compositions. The graph for the 90% Ne to 10% CO_2 is indicated by the red arrow approximately at the 500 V/cm value. It can be seen that the drift velocity increases rapidly for small electric fields for the 90/10 mixture. This is one of the reasons that it is regularly used since it can be difficult to maintain substantial electric fields in a low-pressure gas detector without electrical discharge. The in-beam voltage of ~500 V/cm will result in a drift velocity of ~3.5 cm/μs [23].

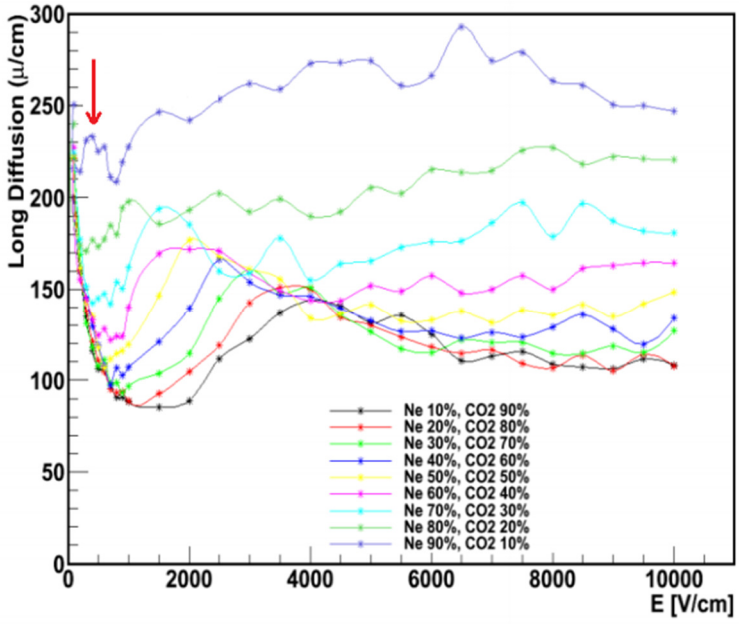

Figure 2.4: Longitudinal diffusion coefficients for various Ne/CO_2 compositions. The graph for the 90% Ne to 10% CO_2 is indicated by the red arrow approximately at the 500 V/cm value. Gaseous diffusion is an important parameter because an increase in diffusion limits the accuracy of gas detectors. Diffusion is usually one of the criteria when choosing detection gas species since it controls some of the inherent TPC detection capabilities. However, free choice of detection gas is often not possible when working with active-target detectors [23].

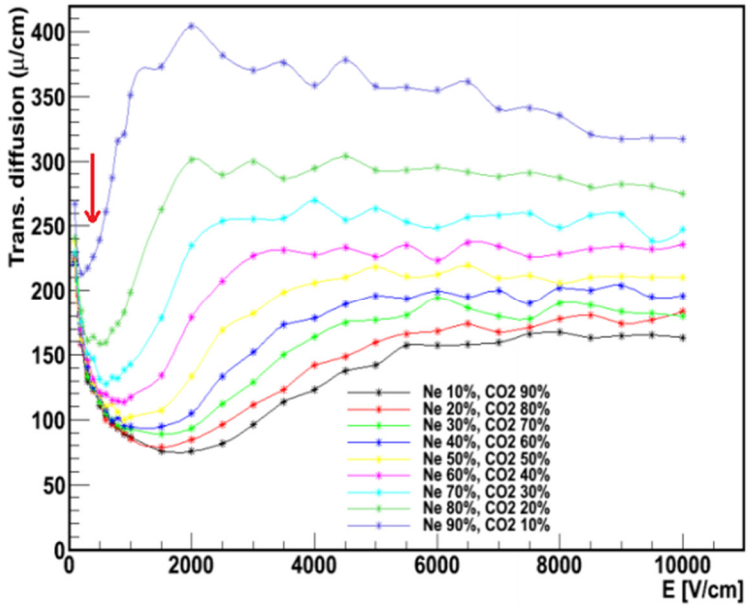

Figure 2.5: Transverse diffusion coefficients for various Ne/CO_2 compositions. The graph for the 90% Ne to 10% CO_2 is indicated by the red arrow approximately at the 500 V/cm value. Transverse diffusion is due to the lateral displacement of electrons within a gas due to their random, thermal motion [23].

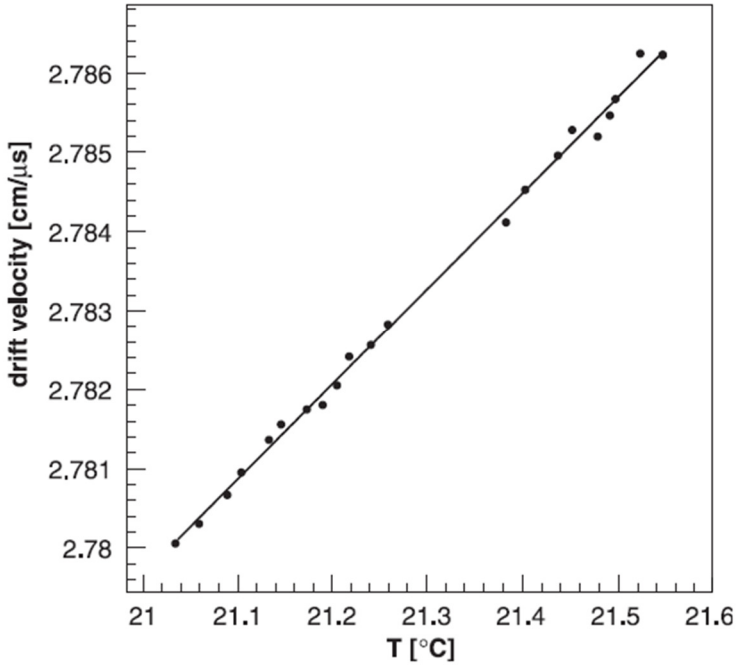

Figure 2.6: Drift velocity dependence on ambient temperature for 9.82% CO_2 in Ne. The measurement was taken with an electric field strength of 400 V/cm [24] at 50 mbar. The dependence is, to a good approximation, linear. Experimental temperatures are generally kept constant for TPCs. However, small variations, as in the graph, are possible should the gas pressure fluctuate marginally.

Momentum resolution and the detection rate capability of a TPC are governed by the detection gas species. However, the drift gas is mostly fixed for GATEAU given that it is an active-target detector. A low-diffusion drift gas with large ion mobility and small elementary charge increases the momentum resolution of a TPC and facilitates high-rate detection [25].

The Ar/CO_2 and Ne/CO_2 gas mixtures used for the standalone and in-beam tests, respectively, require a high drift field (greater than 400 V/cm at 1 atm used for the ALICE TPC [26]) to have acceptable drift times which is needed to have the lowest possible detector dead time. An important fact to keep in mind is that GATEAU is an avalanche detector and not a proportional counter. Parameters like gas gain (ratio between initial and final number of drift electrons) for the Ne/CO_2 mixture is therefore not relevant, except for when saturation is reached.

An important detection principle is summarised by the Shockley-Ramo (SR) theorem: the signal in biased detectors is due to the movement of charge and not as a result of charge collection at an electrode. This statement is conditional but still relevant in TPCs. The SR theorem describes how energy is converted from a bias supply to moving charge in a detector [27]. Consider the following scenario that may exist in a TPC: ionising radiation creates a free charge q at point x within the detection region. A charge Q is induced on an electrode by the movement of q where Q is amplified at the electrode and converted into a detector signal. This series of events can be translated into a GATEAU event. An incident α-particle interacts with the neon gas and creates many ion pairs. The movement of drift electrons from the separation of ion pairs can be equated to q. This causes variations in the induced charge Q at the signal wires of the GATEAU printed circuit board (PCB) where the charge q is donated and consequently discharges the electrode or signal wire. The SR theorem describes a way of calculating the induced charge on detector electrodes and is valid for stationary space charges as well as vacuum tubes [28]. The theorem is not only relevant to TPCs but also applicable to silicon detectors and other instruments where charge separation and collection is the primary mode of detection.

The Shockley-Ramo theorem quantifies the induced charge Q and induced electrode current *i* as [27]:

$$Q = -q\varphi_0(x), \tag{1}$$

$$i = q\vec{v}E_0(x). \tag{2}$$

The instantaneous velocity of the free-moving charge q is given by $\vec{v}$. The weighting potential and weighting field at the immediate location, x, of charge, q, is symbolised by $\varphi_0(x)$ and $E_0(x)$, respectively. The calculations are valid when there is no appreciable magnetic field within the volume of the space charge and if it can be assumed that the electric field of charge, q, propagates instantaneously [29]. Therefore, the problem of calculating an induced charge can be simplified to a problem of electrostatics at each moment of charge movement where the instantaneous position of q is always x.

2.2 Preceding Active-Target Developments

Various active-target developments have been completed over the last decade. This is largely due to the implementation of new radioactive ion beam (RIB) facilities since the detectors are well-suited for the low-intensity beams produced by RIBs [30]. The exotic reactions that result from RIB experiments suffer from low-energy reaction products and low cross sections which can be dealt with by the implementation of TPCs in general. Some of the active-target developments are shown in Figure 2.7.

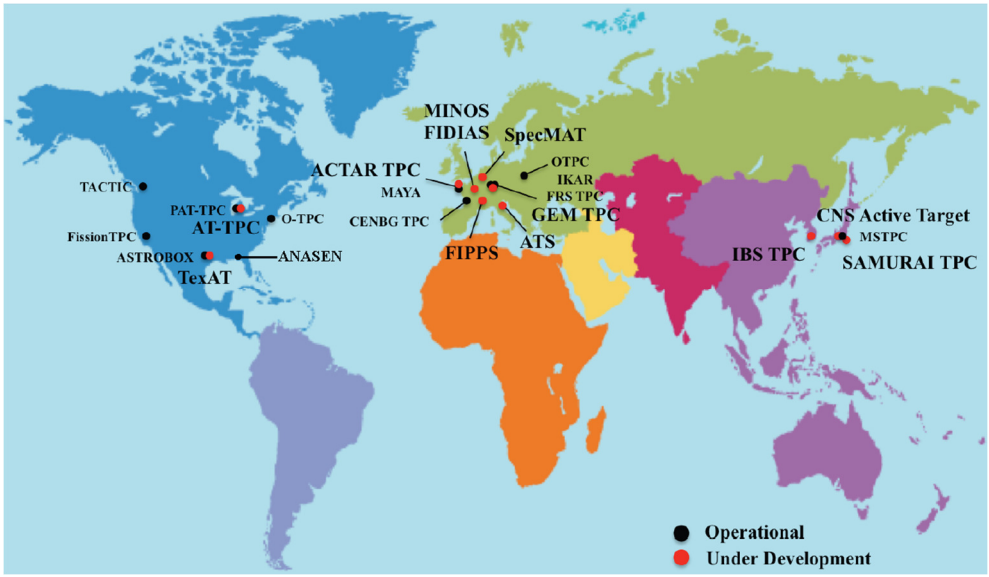

Figure 2.7: Global map of various active-target and TPC facilities. Active-target and TPC detector systems that are operational are indicated in black whilst those that were under development upon [31] being written, are indicated in red. IKAR was designed for studies related to high-energy physics and is the first active-target detector ever built.

The previous detector developments were also regarded as progress towards a better understanding of the TPC principle as it is applied to active-target detectors in order to improve upon them. Consequently, new developments have been started over the past two years to replace older versions. Chief among which is the French SPIRAL2 RIB facility at GANIL, Caen. A new TPC project was commissioned in February 2014 and aims to have a testable prototype by 2019. This will be the successor to the MAYA detector (see section 2.2.2) that was used at the SPIRAL RIB facility, also at GANIL. The budget of this development is roughly €1 300 000 [32]. This serves to illustrate the potential for these types of detectors and that initial detector developments like MAYA are regarded as milestones towards improving the implementation of active-target detection systems. However, GATEAU is potentially of great experimental use even with a significantly smaller budget. GATEAU can also be regarded as a consequence of the proposed RIB facility to be built at iThemba LABS. This study will yield insights that may prove useful when the RIB accelerator is operational and specialised detectors are needed for the experiments. Each detector discussed in this section is unique in its method of detection and in turn fundamentally different from GATEAU. The TACTIC, MAYA and ANASEN detector systems will be discussed and compared.

2.2.1 TACTIC

The TRIUMF Annular Chamber for the Tracking and Identification of Charged particles, or TACTIC, was jointly developed by the University of York and TRIUMF. It was specifically designed for the identification of reaction products decaying from astrophysical resonances that have low-energy reaction products and low cross sections [33]. The detector enables measurements of differential cross sections over a large solid angle with high geometrical detection efficiency. A simplified illustration of the detector is shown in Figure 2.8.

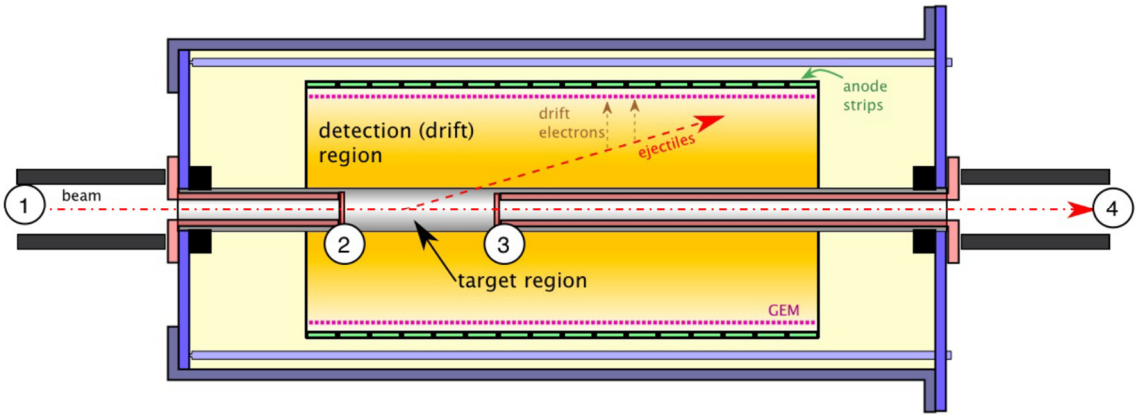

Figure 2.8: Schematic of the TACTIC cylindrical ionisation chamber illustrating the four primary regions of the assembly [33]. The beam (1) enters the ionisation chamber at (2) and exits at (3) before completely passing out of the detector assembly at (4). When a nuclear reaction of interest takes place the ejectiles will move out of the target region and into the detection region and ionise the gas. Drift electrons move radially outward whereas GATEAU drift electrons will drift longitudinally with regard to the beam axis.

Drift electrons are not produced while the ejectile moves from the parent nucleus through the target region. The point of nuclear reaction is inferred by extrapolation of detected particle tracks to find the reaction locus. The detector windows at (2) and (3) are 1-µm thick, aluminised Mylar or SiN. TACTIC uses gas electron multipliers (GEMs) for proportional amplification to aid detection. The TACTIC GEM component is made of a 50-µm thick polyimide(4,4'-oxydiphenylene-pyromellitimide) [34] foil (more commonly known as Kapton) that is coated on both sides with copper, with small holes throughout the structure. The GEM can achieve significant electric-field gradients through the holes with a relatively small potential being applied, as shown in Figure 2.9. The GEMs are located before the azimuthally segmented TACTIC detection anode so that the small signals are amplified. It is used in place of a Frisch grid [35]. When GATEAU was designed the possibility of using GEMs was eliminated due to cost. Another drawback of using them is that the detector gas pressure, gas flow rate and GEM voltage has to form part of the dataset given that the GEM response varies according to these three factors and will in turn influence the detector signal readout [33].

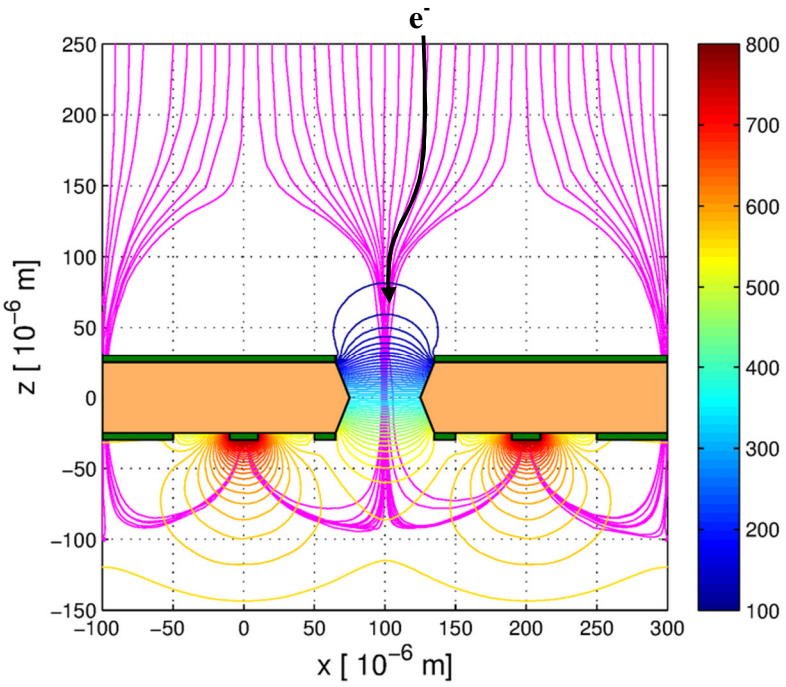

Figure 2.9: Garfield simulation of the electric field lines in a GEM [36]. The electric field that a GEM generates between the terminals (in blue) amplifies the expected small signals that TACTIC has to detect. As the primary drift electons pass through the GEM hole structure under influence of the drift field, they start to avalanche toward the anode but proportionality is conserved. After GEM amplification, the electrons move on to the TACTIC anode. The drift field is shown in purple and the amplified field is shown in yellow. A typical drift-electron track is indicated by the black arrow.

TACTIC has two cylindrical wire barrels that act as the guard wires. These wire cylinders maintain a homogeneous radial electric field within the detector. The guard wire configuration is shown in Figure 2.10.

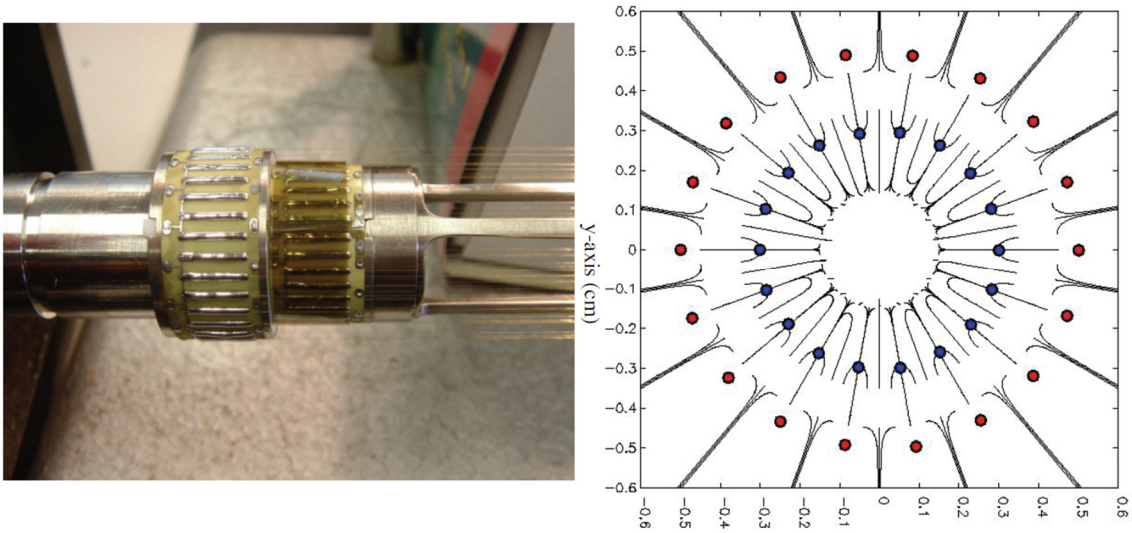

Figure 2.10: TACTIC guard wire configuration [33]. The inner wire cylinder has a diameter of 10 cm with a potential of -1800 V and the outer cylinder has a diameter of 12 cm with a potential of -2000 V. They are electrically isolated from each other and the chamber while serving as a boundary for the target region. TACTIC can achieve high beam intensities, which is an a-typical feature in active-target detectors, due to the guard wire configuration.

The guard wire configuration allows for higher beam intensities (up to 10^8 pps) since ionisation that is caused by the beam passing through the active-target region is contained. Any unrelated charged particles will, therefore, not enter the drift region. Certain active-target detectors that are designed for RIB experiments, like MAYA described in section 2.2.2, stop the low-intensity RIB beam completely within the detector volume. This implies that all of the beam particles and scattered particles from the nuclear reactions are tracked and this is an important limitation with regards to detector dead-time. The TACTIC detection limit is set by elastic scattering events rather than the beam intensity. The implications of elastic scattering with regards to GATEAU are discussed in section 6.2.2.

2.2.2 MAYA

The MAYA active-target detector was built for the SPIRAL radioactive ion beam (RIB) facility at GANIL. It is a high-efficiency, 4π solid angle detector to overcome the low-energy thresholds and relatively low cross sections (~mb) for experiments using RIBs to study areas of the nuclear chart away from the line of stability. The SPIRAL accelerator can reach energies up to 25 MeV/nucleon [32]. MAYA is significantly different from TACTIC in various aspects like its geometric design and detection method. MAYA uses a segmented cathode in the form of a honeycomb structure for charge detection. However, the main difference is that the low-intensity beam (~10^3 pps) is stopped completely within the active detection region. Each particle flight path through the detector is tracked on an event-by-event basis which limits the detector count rate. The parameters of the detector, like detection gas and entrance window, can be changed according to the needs of the experiment and the reaction of interest thus improving experimental flexibility. The internal detector design is shown schematically in Figure 2.11.

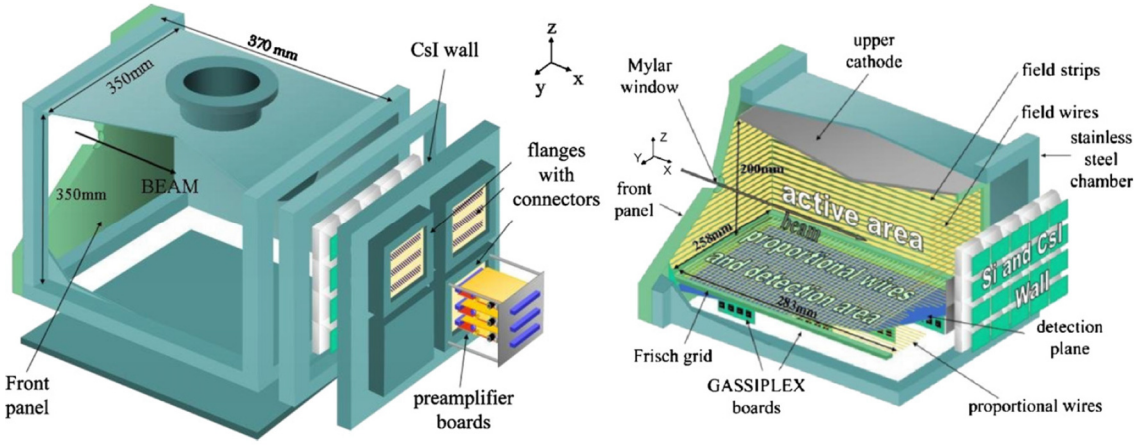

Figure 2.11: Internal structure of the MAYA active-target detector [37]. The detection gas and detector entrance window can be changed according to experimental preferences. MAYA uses silicon and CsI detectors in addition to the segmented cathode for particles that are not stopped within the active volume. The detector has a beam entrance with a 1.3-cm diameter. A 6-μm thick Mylar window is generally used and can maintain an internal gas pressure of up to 3 bar. This increases the effective target thickness whilst maintaining energy resolution.

A steel skeleton forms the basis of the detector. The volume within the steel chamber is 28.3 cm long, 25.8 cm wide and 20 cm high. The 14.6-L detector volume constitutes the active detection region wherein the target gas is located. The MAYA design enables the use of combustible gasses like hydrogen and isobutane as well as other gasses, depending on the nature of the experiment. The detector has four main components: (1) a beam entrance and (2) a wall of ancillary detectors as well as (3) a high-voltage (HV) cathode and (4) segmented detection cathode. The beam entrance is located on the front panel while the ancillary-detector wall is mounted outside the detector on the downstream panel.

MAYA has an ancillary-detector wall, apart from its active-target capabilities, for δE-E identification. The wall can host 20, 700-μm thick, 5 x 5 cm^2 silicon strip detectors (SSDs) and 20, 1-cm thick, 5 x 5 cm^2 caesium iodide (CsI) detectors that are positioned behind the silicon-detector wall. The ancillary detectors are mainly used to detect light, highly-energetic recoil nuclei and scattered particles that are not stopped within the active detection region, like protons or tritons [32].

A high-voltage steel cathode forms part of the top detector panel and is responsible for establishing the drift field. A potential of -10 kV to -15 kV is applied between the HV cathode and the Frisch grid for a maximum field strength of ~75 kV/m. The potential depends on the target-gas pressure and low-energy detection threshold needed for a particular experiment [37].

The bottom panel has three components, namely an electrically grounded Frisch grid, an anode and a segmented cathode. The Frisch grid is located ~20 cm below the HV cathode and is used to prevent false signals being induced in the segmented detection pads. The anode, which is located 8.5 mm underneath the Frisch grid, is a plane of 32, 50-μm diameter gold-plated tungsten wires that run perpendicular to the beam direction. The anode can also use 5-, 10- or 20-μm diameter wires that are spaced 2-2.3 mm apart. The wires have an applied potential of -1 kV to -5 kV which also depends on the detection gas pressure and low-energy detection threshold needed for a particular experiment [37]. The anode is used to amplify signals from low energy-loss particles. It consequently decreases the low-energy detection threshold of MAYA. The segmented cathode has a honeycomb structure and is designed for charge collection. It is ~10 mm below the proportional wire plane. The structure of the cathode is shown in Figure 2.12.

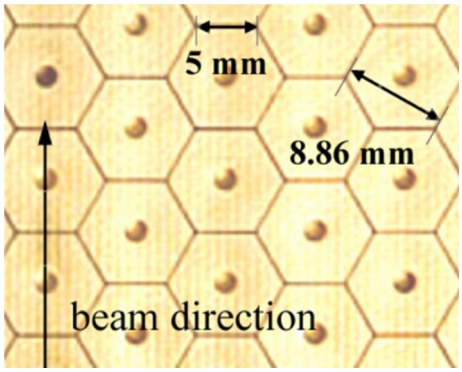

Figure 2.12: Honeycomb structure of the segmented cathode in MAYA. Each side of the hexagonal pads is 5 mm long. A total of 32 rows and 32 columns segment the detection plane into 1024 pads. The cathode plane is connected to CERN GASSIPLEX PCBs. Each PCB provides amplification and signal shaping to 16 pads [38].

Electric field homogeneity is achieved by mounting printed circuit boards (PCBs) inside the detector on the side and upstream panels. The PCBs consist of multiple copper field strips that are 3-mm wide and 1-mm apart.

Energy and time-of-flight (TOF) are the two main quantities measured during MAYA experiments. The energy measurements stem from signals from the cathode. A small drift chamber is located upstream from MAYA and functions as a beam detector. It provides the event start signal and, along with MAYA, produces a TOF signal. Figure 2.13 shows an illustration of the p(^{11}Li, ^{9}Li)t experiment performed with MAYA. The results are shown in Figure 2.14.

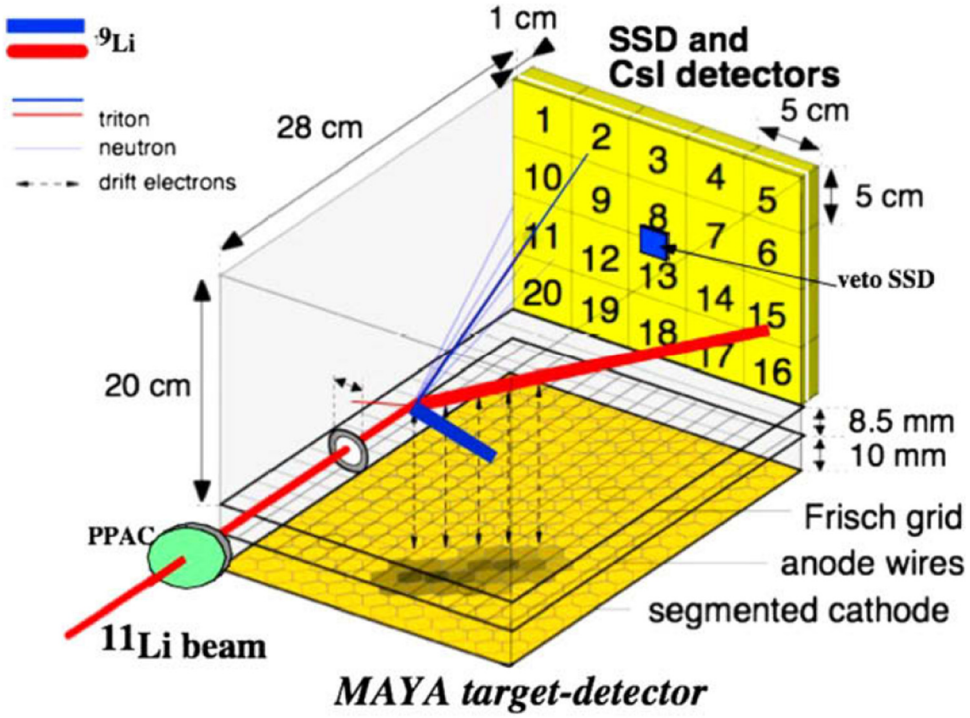

Figure 2.13: Illustration of the MAYA active-target TPC development. The detector is designed for the study of exotic nuclear decays using the SPIRAL RIB facility at GANIL [32].

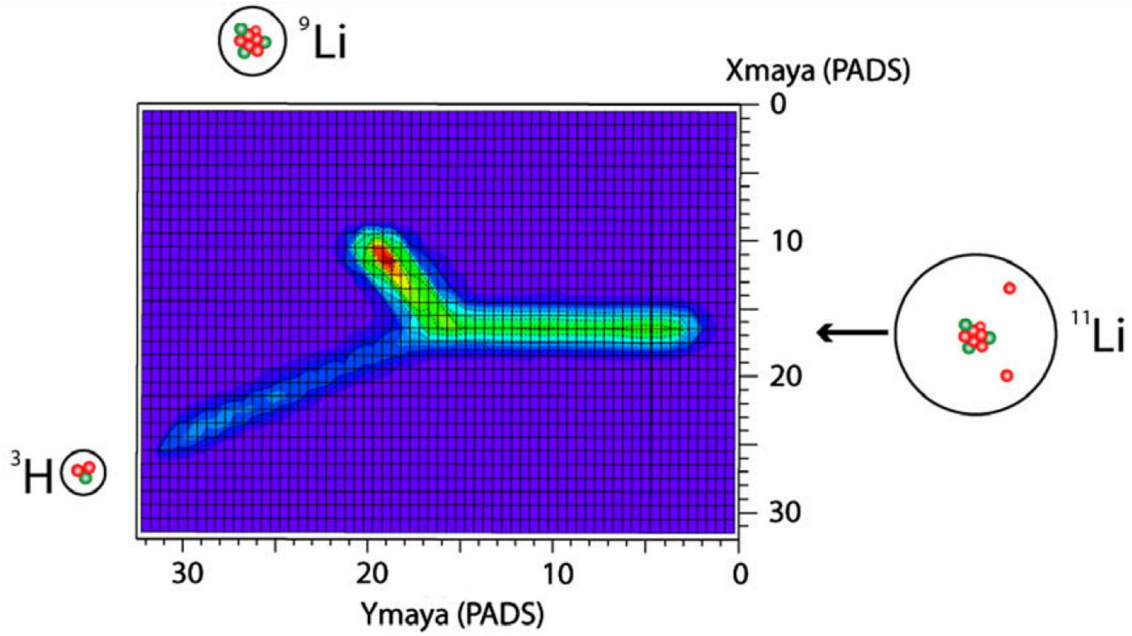

Figure 2.14: Results from the p(^{11}Li, ^{9}Li)t MAYA experiment at 3.6 MeV/nucleon. MAYA was designed for binary reactions with exotic nuclei for inverse kinematic experiments. The figure illustrates that the detector stops the secondary beam and reaction products entirely within the active detection region. The colour intensity of each detection pad corresponds to the number of drift electrons collected [38].

The experiment was performed to elucidate the halo structure of the ^{11}Li nucleus by way of a two-neutron pick up reaction performed in inverse kinematics. The ^{11}Li nucleus is a paradigm example of halo structure in light nuclides. The experiment was performed using isobutane (C_4H_{10}) as the detection gas, at a pressure of 350 mbar resulting in an effective target thickness of 4.3 mg/cm^2 [32]. From this example it is evident that active-target detectors can be used to study interesting nuclear phenomena under difficult experimental conditions.

2.2.3 ANASEN

The Array for Nuclear Astrophysics and Structure with Exotic Nuclei (ANASEN) is an active-target detector that was developed and built at Florida State University (FSU). It was primarily designed for the study of astrophysically relevant resonances with the RESOLUT RIB facility at FSU and ReA3 at Michigan State University (MSU). ANASEN can be regarded as a composite of TACTIC and MAYA. It has a cylindrical geometry and three inner wire cylinders that run parallel to the beam axis, similar to TACTIC, but uses silicon strip detectors (SSDs) and CsI detectors for particle tracking and identification like MAYA [39]. Another important difference is that ANASEN does not track the particles of interest as TACTIC or MAYA. It reconstructs the particle tracks from two intersection points at the central position-sensitive proportional counter (CPSPC) and position-sensitive silicon-barrel array (PSSBA). A simple illustration of the detection principle is shown in Figure 2.15.

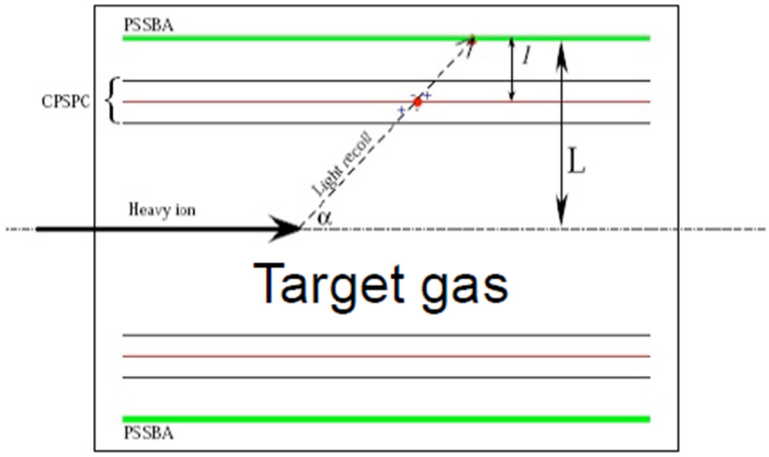

Figure 2.15: Basic illustration of the ANASEN detection method. Recoil nuclei and scattered particles are detected by an annular array of SSDs and CsI detectors after being detected by the proportional counter wire cylinder [40].

The cylindrical geometry of ANASEN is used to mount three, annular ancillary-detector arrays. Each array has 12, 1-mm thick super-X3 type SSDs. The SSDs have a surface area of ~70 cm^2 with position resolution $\delta x < 1$ mm and energy resolution $\delta E < 100$ keV. Each SSD has a CsI detector directly behind it. The CsI detectors are 2-cm thick [40]. Each one of the annular detector arrays can be removed to optimise the setup in accordance with the experiment. A 3D CAD drawing of the ANASEN setup is shown in Figure 2.16. A photo of the detector is shown in Figure 2.17 where one of the three annular arrays have been removed thus exposing the inner wire cylinder structure.

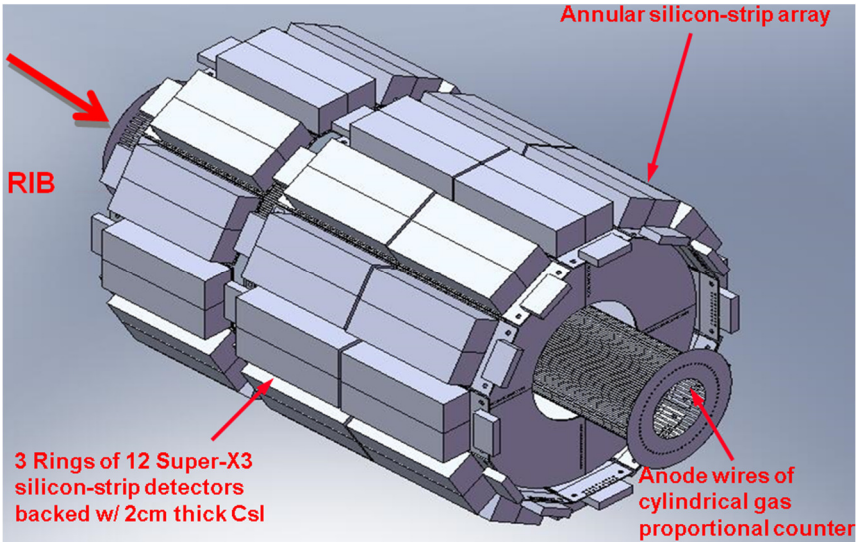

Figure 2.16: CAD drawing of the ANASEN experimental setup. The detector has three, annular ancillary-detector arrays. The arrays consist of SSDs and CsI detectors. The beam entrance and exit is indicated along with the internal wire-cylinder configuration. An entrance window made of 2-μm thick titanium is generally used. The detector is versatile and the entrance and exit windows can be changed as well as the detection/target gas [39].

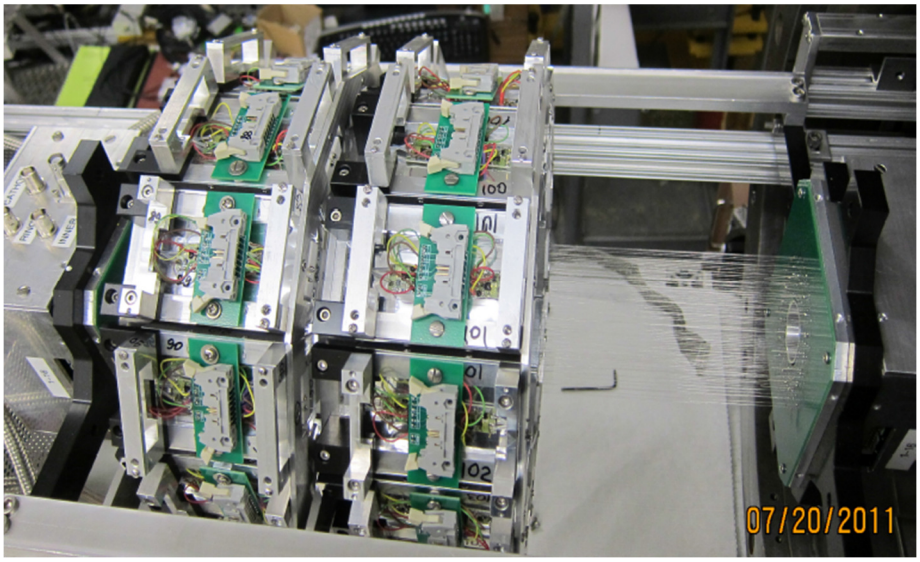

Figure 2.17: Photo of the outer structure of ANASEN. Removing the first annular ancillary-detector array reveals the inner wire cylinder structures. The region between the wire cylinders and the ancillary detectors constitutes the active region of ANASEN [40].

ANASEN has three wire cylinders to assist detection. The inner and outer cylinders constitute the shielding electrodes. They are positively biased to prevent unwanted charged particles (mostly electrons) from entering the active detection region and causing false signals. The shielding electrodes allow ANASEN to work with relatively high RIB currents up to 10^4 pps [39]. The guard-wire cylinders are shown in Figure 2.18. The anode wire cylinder, located between the inner and outer guard-wire cylinders, is used as a proportional counter and surrounds the beam axis. The cylinder has 19, 43-cm long anode wires made of a 7-µm thick diamond/carbon fibre mixture [40]. The downstream detection panel of ANASEN has a QQQ-type silicon-detector array. Each one of the four detectors covers a quadrant. Another array that can be used on the downstream panel has 6, standard X3-type silicon detectors (as used in the PSSBA) backed by 16, 2.5-cm thick trapezoidal CsI detectors.

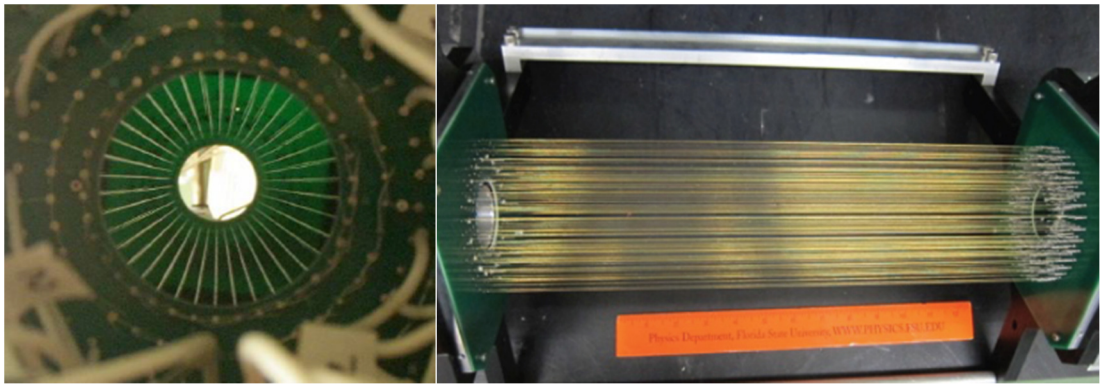

Figure 2.18: Guard-wire cylinders used for ANASEN. This component is similar to the guard wire design in TACTIC and is likely due to the cylindrical detector design. It is used to confine unwanted charged particles and prevent them from entering the active region [40]. The inner guard wire cylinder is shown on the left. The entire wire setup is shown on the right. The annular silicon-detector arrays are mounted around these wire structures.

Many other active-target detection systems have also been successfully developed but will not be discussed here. Most of these systems are variations on a similar theme [41, 42, 43] given that they have analogous detector components such as those used in TACTIC, MAYA and ANASEN.

The Gaseous Active-TargEt Ancillary Unit (GATEAU) has a cylindrical geometry within the small-angle mode scattering chamber (see section 3.2 and 6.1). However, unlike TACTIC and ANASEN, the electric field will not be applied radially. GATEAU is designed to detect drift electrons moving under the influence of a longitudinal drift field. An inherent drawback to GATEAU is the mounting unit. TACTIC, MAYA and ANASEN are dedicated detection units and each can be added to their respective beam lines as a single entity.

2.3 Probing the 5α State with the ^{20}Ne(α,α')^{20}Ne* Reaction

Inelastic α-particle scattering is used because of its particular spin and isospin selectivity implying that mostly $\Delta S = 0$ and $\Delta T = 0$ excitations are observed [44]. In contrast, inelastic proton scattering can excite $\Delta S = 1$ and $\Delta T = 1$ modes in addition to those excited by inelastic α-particle scattering. A two-neutron transfer reaction was used to perform the ^{22}Ne(p,t)^{20}Ne* experiment [10, 11] and its ability to excite various spin and isospin states is precisely why it was possible to observe a candidate for the 0^+ 5α ^{20}Ne state. However, in order to probe α-particle decay from the 22.5-MeV state, selectivity is required given the overwhelming amount of states and decay modes that may otherwise be encountered.

Various angular momentum transfer values (ΔL) are possible for states with a given spin and isospin. In the quest of identifying low-spin states, low angular momentum transfer reactions are preferred, e.g. $\Delta L = 0, 1$ [44]. As discussed earlier, various states were discovered in ^{20}Ne as shown in Figure 1.2. These states were discovered because the 17-23 MeV excitation energy region was investigated for the first time with high energy resolution at forward angles and 0° [11]. A ^{20}Ne(α,α')^{20}Ne* experiment at 0° will also be performed because of the high selectivity for low-spin states so that the 0^+ 5α state may sufficiently be populated.

The $\mathcal{M}\left(0^+_n\text{-}0^+_1\right)$ isoscalar monopole transition matrix element is proportional to the $E0$ transition matrix element $M(E0, 0^+_n\text{-}0^+_1)$ [45] for states with total isospin T = 0. The relation is given as:

$$\begin{aligned} \mathrm{M}\left(E0, 0^+_n\text{-}0^+_1\right) &\equiv \langle 0^+_n| \sum_{i=1}^{N} \frac{1+\tau_{3i}}{2} (\boldsymbol{r}_i\text{-}\boldsymbol{R}_{\mathrm{c.m.}})^2 \ |0^+_1\rangle \\ &= \frac{1}{2}\mathcal{M}\left(0^+_n\text{-}0^+_1\right). \end{aligned} \tag{3}$$

The summation is generalised for nuclides with N nucleons. For ^{20}Ne, the sum is allowed to run from 1 to 20. In general, $\boldsymbol{r}_i$ denotes the coordinate of each nucleon (i = 1, 2,…, 20 for ^{20}Ne) and $\boldsymbol{R}_{\mathrm{c.m.}}$ is the centre of mass of the nucleus. The isospin of the

nucleus is given by τ_{3i} with an isospin projection of -½ for neutrons and +½ for protons. The quantum mechanical *E*0 operator for transitions from a nuclear ground state to an excited T = 0 state is consequently proportional to the root mean square (RMS) radius of the particular state [46]. Therefore, the $l = 0$ (α,α') reaction is a good probe for states with a total isospin of T = 0 [44] since the excitation is proportional to the RMS radius of the excited state.

The density distribution of nucleons within a given nucleus can be calculated by antisymmetrized molecular dynamics (AMD) [12]. However, AMD generally underestimates the extent to which the density distribution dissipates for nuclides with large radii. The reason for this is that the AMD framework is a type of bound-state approximation [12]. The (α,α') reaction is also a good isoscalar probe for the 5α state since the beam α particles are isoscalar.

The α-particle beam energy for the ^{20}Ne(α,α')^{20}Ne* reaction will be E_{lab} = 200 MeV. In general, the excitation energy is ~20% of the beam energy but this is an upper limit [44]. Therefore, to study resonances with high excitation energies like 22.5 MeV, higher beam energies will be needed than were used in [10]. Another reason is that it is also preferable not to have the state of interest located at the edge of the focal plane (see Figure 1.2). The energy limit for α particles is 200 MeV at iThemba LABS.

If the ^{20}Ne(α,α')^{20}Ne* reaction succeeds in populating the 5α state, it is not guaranteed that the desired α decay will be observed easily. However, this is accounted for in the design of the detector. GATEAU is a charged-particle tracking detector with high solid angle coverage (close to 4π) to increase its detection efficiency. This is the primary motivation for the double end-cap setup (see Figure 6.9).

Chapter 3
The K600 Magnetic Spectrometer

> "If you can't explain it simply, you don't understand it well enough."
>
> Albert Einstein

Magnetic spectroscopy is a powerful tool in the field of cluster studies and nuclear physics in general. The K600 magnetic spectrometer, used in coincidence with various ancillary detectors like GATEAU, is well-suited for charged particle spectroscopy on α-conjugate nuclei. It is necessary to investigate the fundamental principles of the spectrometer since GATEAU is specifically designed as an ancillary detection unit for the K600. The K600 is one of only two high-energy resolution spectrometers able to operate at 0°, with the other at the Research Centre for Nuclear Physics (RCNP) in Osaka, Japan. The K600 is a copy of the spectrometer design from the Indiana University Cyclotron Facility (IUCF) [47]. Its name is related to the energy constant of the spectrometer given by:

$$K = \frac{mE}{q^2}, \tag{4}$$

where m is the mass number of the particle transported to the focal plane, E the beam energy in MeV and q is the charge-state of the particle. For 200 MeV-protons (m = 1, q = 1) and α particles (m = 4, q = 2) K = 200 while for tritons (m = 3, q = 1), K = 600. The energy constant is related to the 2.1 m nominal bend radius in high-dispersion mode [48] that the spectrometer can achieve. In contrast, the Separated-Sector Cyclotron (SSC) particle accelerator at iThemba LABS is nominally K = 200.

The main function of the spectrometer is to momentum-analyse scattered particles, with the primary detection principle of the spectrometer based on the concept of magnetic rigidity. The K600 modus operandi is to separate scattered particles based on their magnetic rigidity in order to generate a focal plane position spectrum by way of multi-wire vertical drift chambers (see section 3.1).

Magnetic rigidity is symbolised by $\vec{R}$:

$$\vec{R} = \frac{1}{\sqrt{1-v^2/c^2}} \frac{m\vec{v}c}{q} = \gamma \frac{m\vec{v}c}{q} = \frac{\vec{p}c}{q}, \tag{5}$$

where q is the charge, $\vec{p}$ the momentum of the scattered particles and c the light speed constant. The Lorentz factor is given by γ. All variables are in SI units [48]. Magnetic rigidity is more commonly expressed as $R = B\rho$, where B is the magnetic field in Tesla and the gyroradius ρ is in meters. The general layout of the spectrometer in 0° mode, which will be used for the GATEAU in-beam test, is shown in Figure 3.1. The K600 can also accommodate relatively large laboratory angles, up to $\theta_{lab} = 87°$.

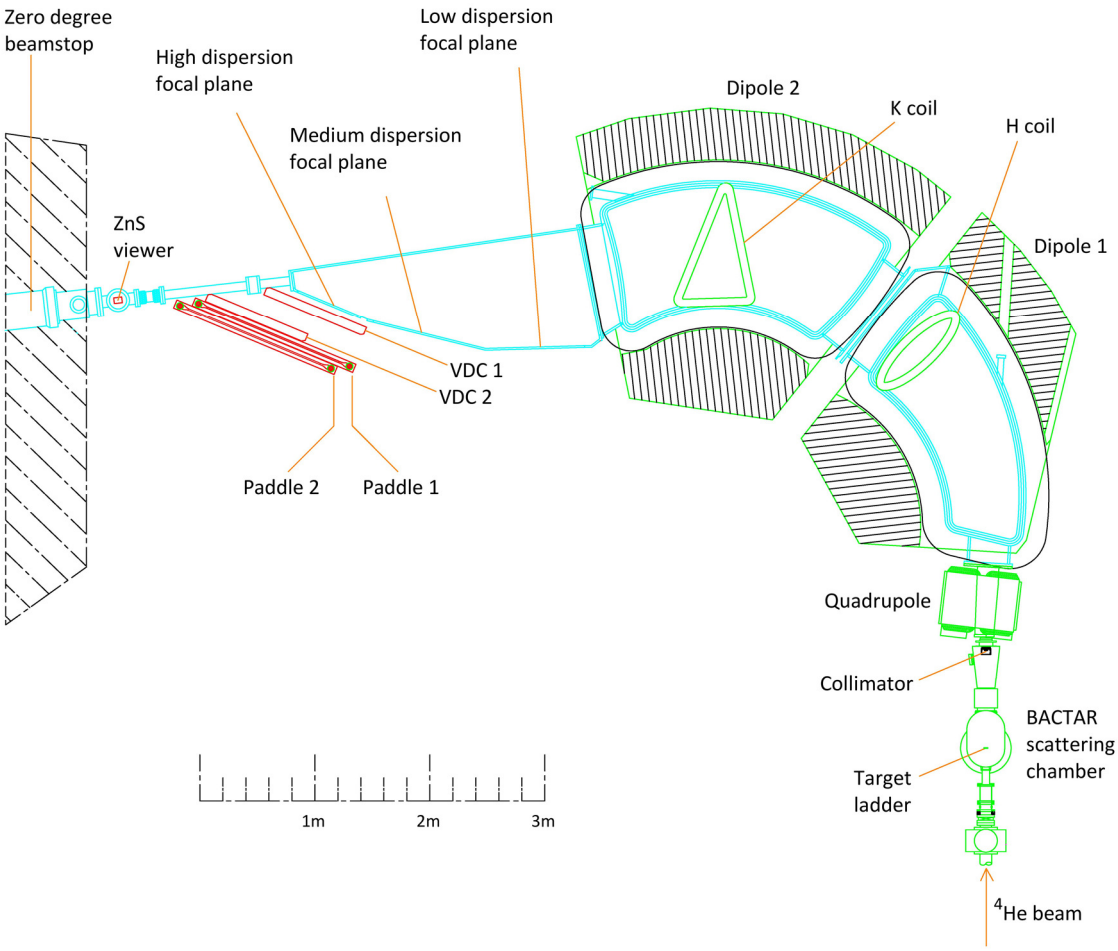

Figure 3.1: The K600 magnetic spectrometer setup for zero degree measurements ($\theta_{scat} < 2°$) with the small-angle mode scattering chamber. A typical particle flight path through the spectrometer is approximately 8 meters [47, 49].

Nuclear reactions of interest generate scattered particles that enter the spectrometer aperture along with the unscattered beam (for 0° measurements). Unscattered beam particles are transported through the spectrometer to a Faraday cup located in the wall of the K600 vault. The unscattered beam is stopped before the quadrupole when in small-angle mode. Particle transport through the spectrometer is facilitated by five magnets with varied abilities. The spectrometer has a quadrupole-dipole-dipole, or QDD setup

(B_{max} = 1.64 T), with two internal trim coils (H and K). The quadrupole is used to focus the beam of scattered particles that enters the spectrometer whereas the dipole/bending magnets enable variations in momentum dispersion which is achieved by altering the relative magnetic fields of the dipoles [48]. The function of the trim coils is to focus scattered particles onto the focal plane which can be done by adjusting the current in the coils thus changing the magnetic field. Some of the main spectrometer components are shown in Figure 3.2.

The high-dispersion focal plane is used for inelastic scattering experiments with the spectrometer in small-angle mode or zero-degree mode. For experiments with finite angle measurements ($\theta_{scat} > 5°$) the focal plane is moved to the medium-dispersion position. Energy deposition in the focal plane detectors and the particle Time-of-Flight (TOF) relay all of the necessary information of an experiment. Particle identification is done by means of a TOF versus scintillation energy spectrum [10]. The scintillation energy is the energy deposited in the plastic scintillator detectors that form part of the K600 focal plane detector system (see section 3.1). The TOF is determined by the time difference between the scintillation trigger signal and the RF signal of the beam pulse [11]. Beam pulse selection allows for a lower period between beam pulses to clean coincidence spectra since the RF signal and scintillation signal clearly delimit the time window for coincidences.

Figure 3.2: The small-angle mode scattering chamber is shown located in the beamline of the K600 magnetic spectrometer. The collimator carousel (1), quadrupole magnet (2) and first dipole magnet (3) can be seen in succession after the small-angle mode chamber (4). The 0° mode is favoured for reactions where $\Delta L = 0, 1$ transitions prevail, i.e. where low angular momentum transfers dominate which is ideal in the identification of low-spin states. This can be used to populate low-spin states selectively in excitation regions that have mostly high-spin states. This holds true for for α-conjugate nuclei making the setup useful for α-cluster studies [48].

3.1 The VDC and Plastic Scintillator Focal Plane

The K600 vertical drift chambers (VDCs) are used to generate the focal plane position spectra whereas the plastic scintillators are used to generate the TOF spectrum and DAQ trigger. GATEAU is based on the design and detection principles of the K600 VDCs since it is relatively easy and inexpensive to build such detectors. Similarities exist between the two detection systems regardless of their differing geometries. Two VDCs and two plastic scintillator detectors constitute the focal plane of the K600 magnetic spectrometer at 0°. The VDCs are multi-wire drift chambers since they are made of multiple signal and guard wires, with the particle track crossing more than one wire.

Each VDC has an X-wire plane and a U-wire plane. The horizontal focal plane position of scattered particles is determined by the X wire plane whereas the vertical focal plane position is given by the X and U wire plane. The X plane has 198, 20-µm diameter signal wires alternating with 199, 50-µm diameter guard/field wires, spaced 4 mm apart, with the wires at 0° relative to the scattering plane. A total of 143, 20-µm diameter signal wires alternating with 144, 50-µm diameter guard/field wires, also 4

mm apart, constitute the U wire plane. The wires are at an angle of 50° relative to the scattering plane [48].

The angle of the wires of the U plane is to improve the vertical position resolution of the VDCs. It is needed since precise measurements of the horizontal and vertical components of the particle tracks are needed to accurately determine the particle scattering angle in 0° mode. Each VDC has three, 27-µm thick aluminium cathode planes, each with a potential of -3600 V. This may vary depending on the beam type and energy. The X and U wire planes are positioned between the cathode planes. The cathodes and wire planes are 8 mm apart [48]. A CAD drawing of a VDC is shown in Figure 3.3.

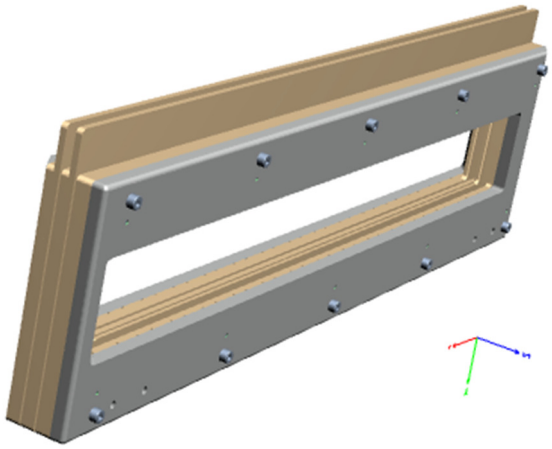

Figure 3.3: CAD drawing of the VDC chamber structure [49]. Planes extending out of the structure represent the X and U wire plane, each in between two HV cathode planes.

Both VDCs have two 25-µm thick Mylar windows to isolate the detector volume and retain the 90% Ar to 10% CO_2 detection gas mixture, which is maintained at 1 atmosphere. Inert CO_2, with a lower ionisation potential than Ar, is used as an internal quenching agent. Ar^+ species (resultant from particle detection) will have a tendency to transfer its positive charge to CO_2 given the difference in ionisation potential [50]. The positively charged quench gas will drift towards the cathode instead of neutralised Ar. Dissociation of the positively charged, molecular structure of CO_2 is thus preferred to the discharge of a free electron from the cathode surface. This will prevent charge build-up in the detector given adequate levels of CO_2 in the gas composition. As a result, arcing and unwanted background signals from secondary electron drift [50] will be prevented. Typical drift speeds in the VDCs are approximately 4-6 m/µs with a drift time of 133-200 ns for a distance of 8 mm between a cathode and wire plane [48]. A simulation of the detection principle is shown in Figure 3.4.

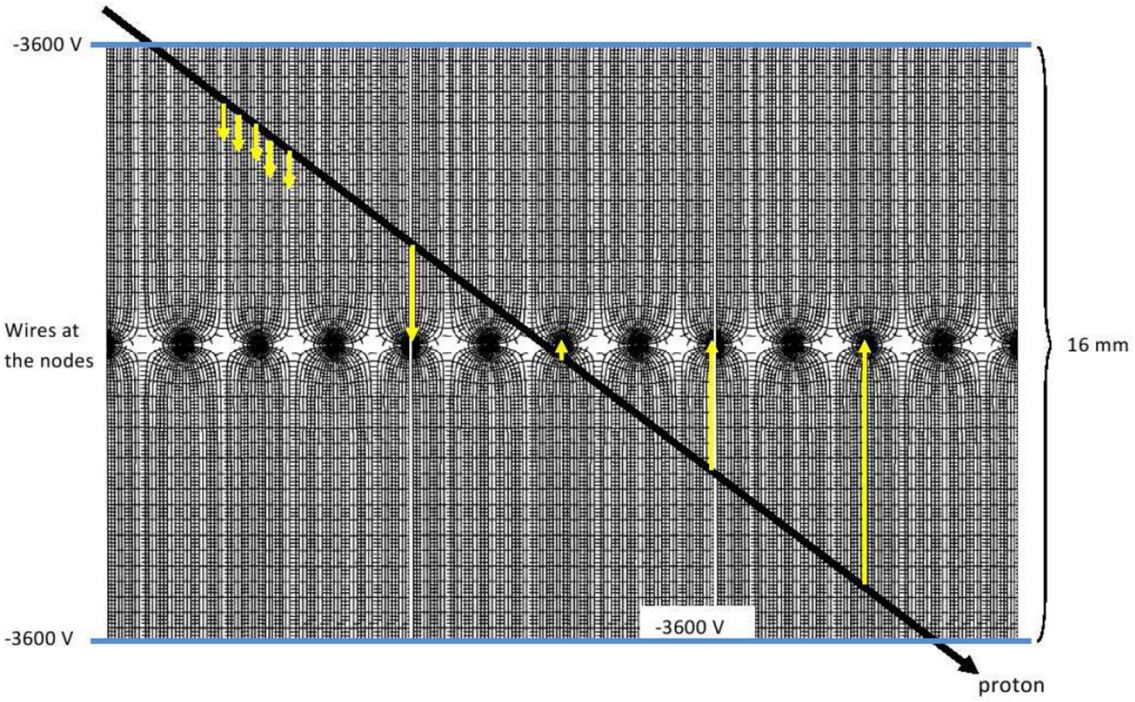

Figure 3.4: Garfield simulation of the K600 VDC field lines. An event is superimposed on the field lines to illustrate the detection principle. Drift electrons move toward signal wires as high-energy ionising radiation passes through the detection gas. The other nodes represent the field/guard wires [48]. Two of the three cathode planes are shown since one wire plane was simulated to produce this figure.

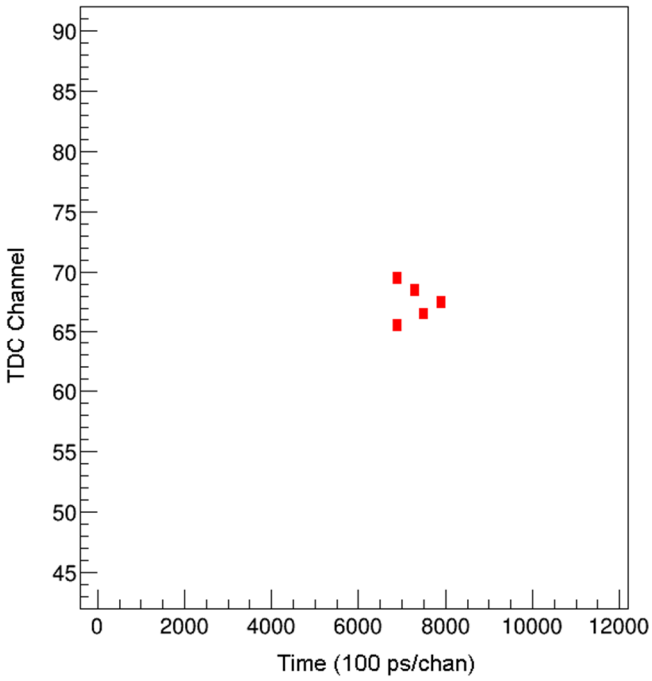

Figure 3.5: Typical VDC event taken from the K600 ^{24}Mg(α,α') experiment with E_{lab} = 200 MeV. Acceptable events take the shape of a V due to the different drift times that are illustrated by yellow arrows in Figure 3.4.

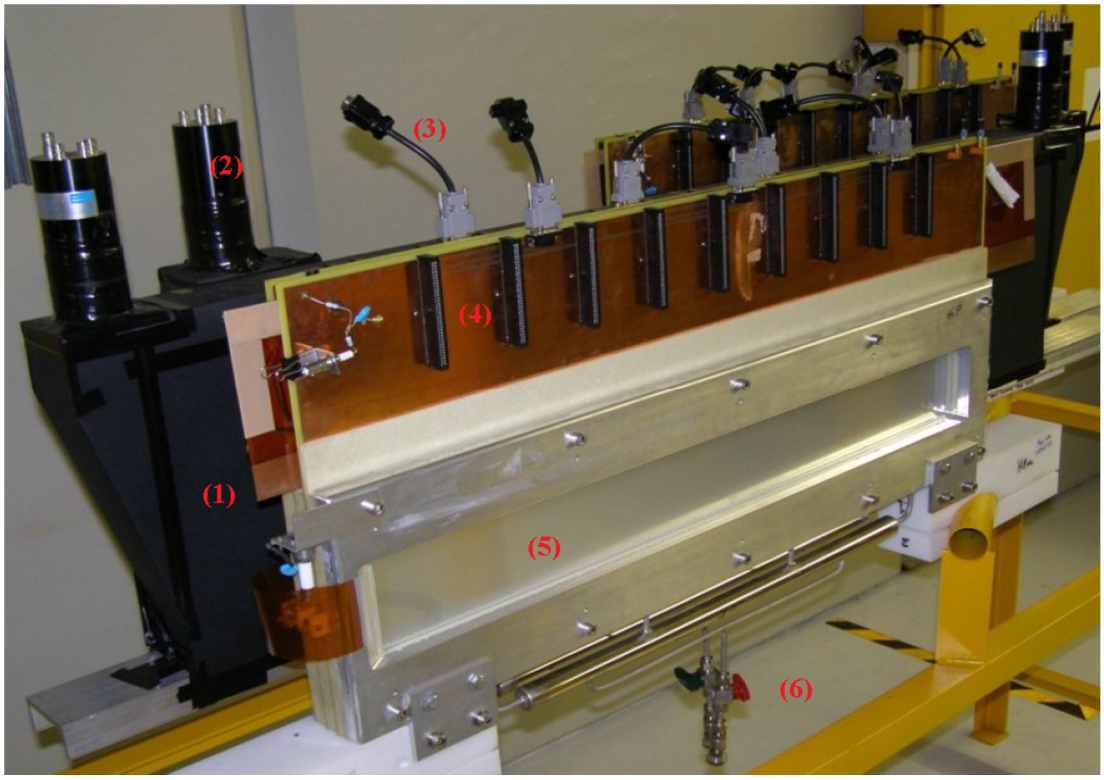

Figure 3.6: Photo of the K600 focal plane detection system. Each scintillator detector (1) has two photomultiplier tubes (2). VDC preamplifier power is supplied by various 9-pin serial connectors (3) with various card edge connectors (4) for the Technoland preamplifier cards. The VDC detection region is enclosed in 25-µm thick Mylar microfilm (5). The detection gas is circulated within the VDC through a gas inlet and outlet (6).

Each U-wire plane has nine, 16-channel Technoland preamplifier units with thirteen units for each X plane. The detection regions of the VDCs are separated from the internal spectrometer vacuum area by a 8 x 68 cm^2, 70-µm thick polyimide(4,4'-oxydiphenylene-pyromellitimide) [34], or Kapton, window.

The two plastic scintillator detectors will play a fundamental part during the in-beam test since GATEAU does not have a data acquisition system (DAQ) trigger. The plastic scintillation material of each detector has a 1219.2 x 101.6 mm^2 surface area. One scintillator has a ½ inch (12.7 mm) thickness and the other has a ¼ inch (6.35 mm) thickness [48]. The scintillators are wrapped in aluminium foil and black paper to prevent light from entering the detector. Scintillation signals are sent via light guides, angled at 90° for spatial considerations, to a photomultiplier tube (PMT) at each end of the detector. An event is only registered if both ends of the detector register a signal.

3.2 The Small-Angle Mode Scattering Chamber

A part of this study included the assembly of the small-angle mode scattering chamber in January 2014 after it had been designed in 2013 by prof. Papka. The chamber was also leak tested. It forms an integral part of the GATEAU detection system as it was designed to accommodate the detector components. The chamber was designed for

various small-angle mode, K600 spectrometer experiments that also use silicon and γ-ray detectors. The chamber size was a compromise between the maximum number of silicon detectors that can be mounted and the distance between the target and external γ-ray detectors. The chamber is made entirely out of aluminium to limit the amount of activation. The 3-mm thick aluminium walls were chosen to minimise γ-ray attenuation for experiments that use γ-ray detectors in coincidence with the spectrometer. The chamber entrance has a ~6-cm diameter and the exit has a ~14-cm diameter. The sizes are comparatively small to limit the amount of beam halo that can enter the chamber and to have a clean focal plane spectrum by limiting unwanted scattered particles from entering the spectrometer.

The shell structure of the chamber allows the walls to be easily removed to simplify experimental setting up within the chamber. Multiple gas-pipe inlets and outlets make it ideal to be converted into a gas cell. A total of 20 Lemo feedthroughs and 6 HV BNC connector feedthroughs allow the chamber to be used with different types of ancillary detectors. An inherent disadvantage of the chamber is that it can only operate at 0° and 4°. The standard K600 scattering chamber has a sliding seal that allows it to access any angle from 0°-7° and 7°-90°. Figure 3.7 and Figure 3.8 show the inner and outer structure of the new scattering chamber, respectively.

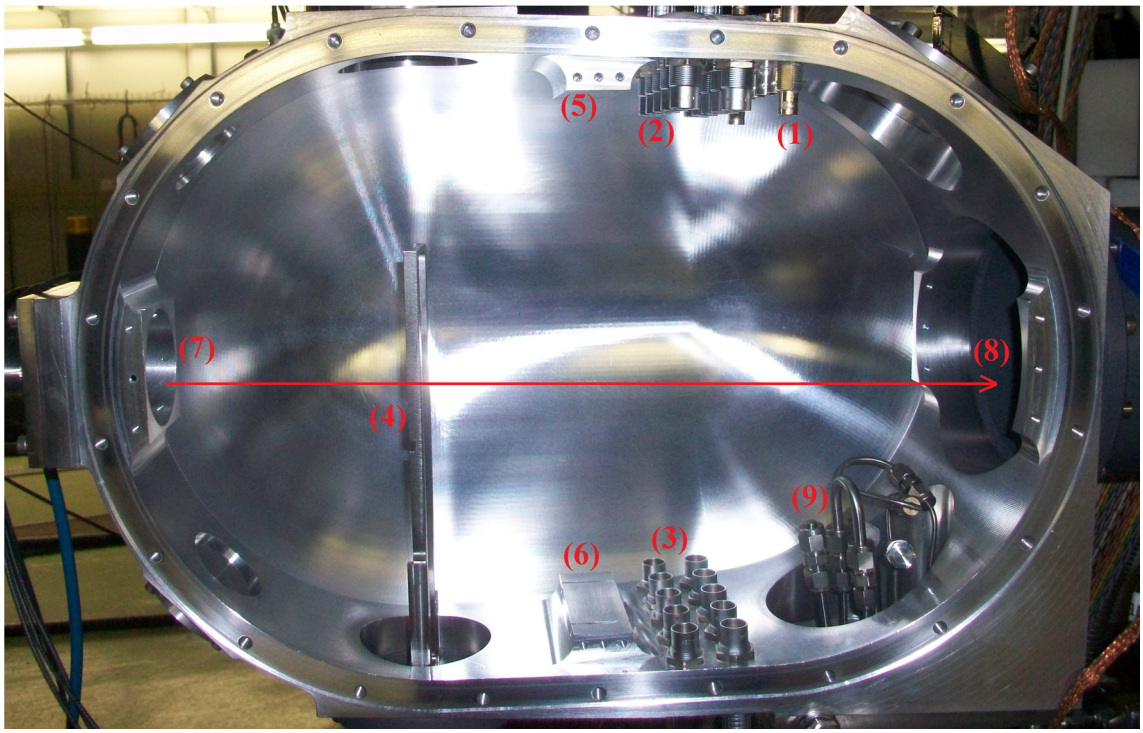

Figure 3.7: Internal view of the small-angle mode scattering chamber. It has 5 HV BNC feedthrough connectors (1) and 20 Lemo feedthrough connectors (2, 3). The target ladder (4) is located in the scattering plane. Various mounting points (5-8) can be used to mount ancillary detectors inside. Small-diameter steel pipes (9) run through the chamber and out to the steel base in order to pump gas in/out of the vacuum region. The beam direction is indicated by the red arrow.

GATEAU was designed to be mounted inside the chamber. The detector PCB will be indirectly attached to (5) and (6) with the chamber entrance and exit windows being

indirectly attached to (7) and (8). The data cables from the PCB will connect to the inner parts of (2) and (3) with the preamplifiers connecting to the outer parts of (2) and (3).

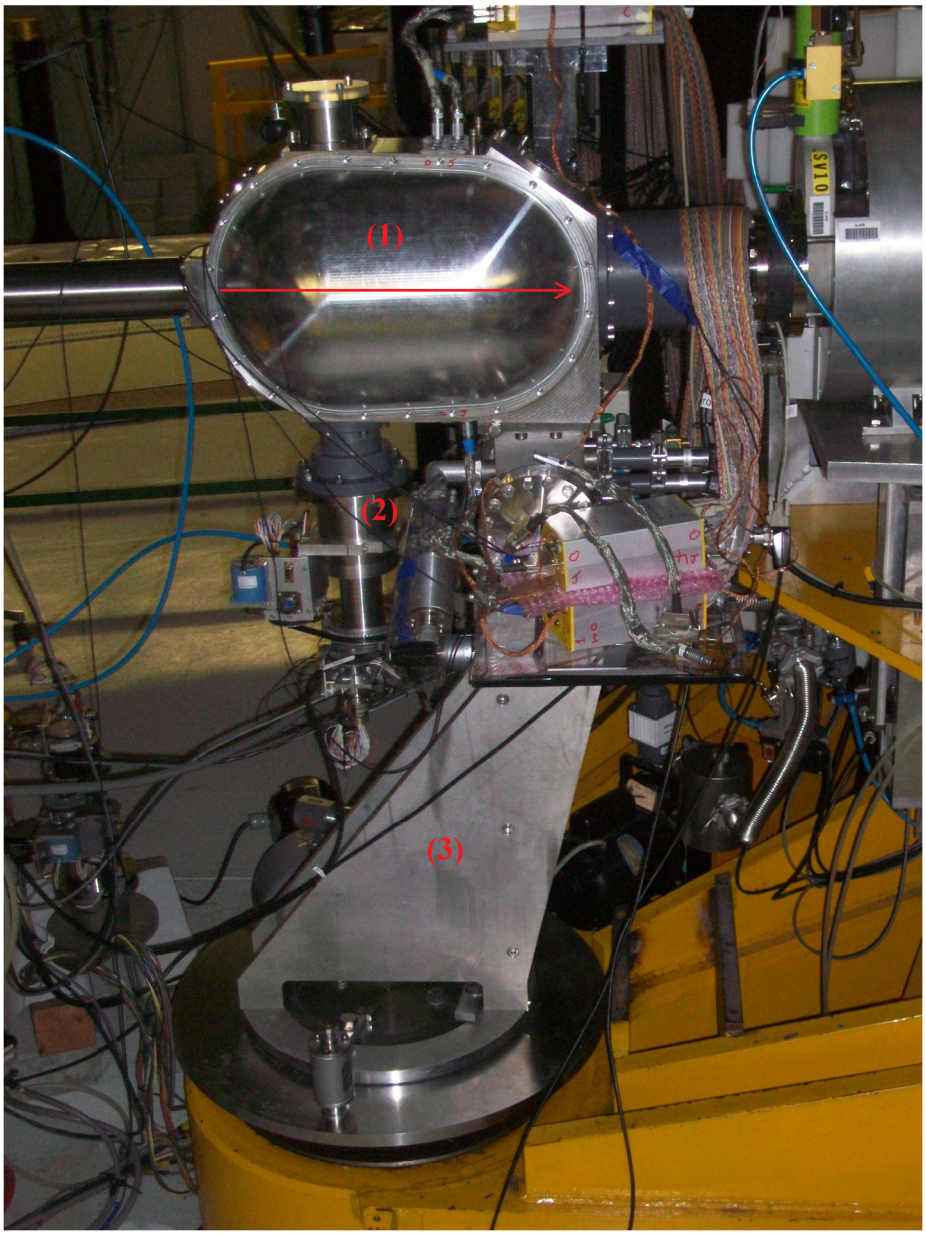

Figure 3.8: The small-angle mode scattering chamber in the K600 magnetic spectrometer beam line. The detachable, aluminium walls (1) of the chamber have an oval shape and sit on the chamber frame. The chamber can accommodate the use of a target ladder mechanism (2) and has a detachable steel base (3). The beam direction is indicated by the red arrow.

The steel base has two different flanges to attach 170 L/s turbo pumps. Various DN25 connectors are also featured that are used to connect the chamber to numerous vacuum gauges, valves and inlet/outlet fluid pipes.

Chapter 4
Detector Design and Simulation

> "Physics is the only profession in which prophecy is not only accurate but routine."
>
> Neil Degrasse Tyson

A problem specific solution, in the form of a wire-chamber PCB, was formulated so that GATEAU would be capable of addressing the experimental challenges of the $^{20}Ne(\alpha,\alpha')^{20}Ne^*$ reaction. Various factors were considered when the PCB shape and structure had to be designed. It was known that the design should not only allow the problem to be addressed in full, but that it should also be feasible and easily executable. The detector should be flexible enough to accommodate various applications so that it may be used in future for experiments which may not have been possible otherwise and have not yet been proposed.

In order to examine the feasibility of GATEAU, various simulations were carried out to investigate the unknown factors of building this particular type of active-target detector for the first time. It should be noted that these simulations cannot comment on the absolute functionality of the detector. They are merely executed in order to discover and demonstrate that there is a high degree of feasibility to the detector concept. Conversely, the simulations were also performed to exclude any variations in the design that would not have been functional. The Garfield calculations were deemed to be most relevant and are included in this chapter.

4.1 GATEAU PCB Design

The primary consideration for the detector PCB was for it to have multiple sectors, each with as many signal wires as possible. It was decided that each sector would have 16 signal wires, and therefore 17 guard wires, since it was compatible with the preamplifier specifications as each Technoland unit (see section 4.2) can accommodate 16 inputs. The multi-wire structure implies a large number of signal tracks. Using standard CAD

freeware [51] it was found that, should the design be a single-layer PCB structure, the dead area of the detector would be too large. The PCB was converted to a multi-layer design using Altium PCB design software [52] with assistance from [53]. The final design is shown in Figure 4.1. For reference, the inner signal wire is connected to signal track (or trace) 1 and the outer signal wire is connected to signal track 16. Sharp corners were avoided in the design to prevent concentrated electric fields being established that may lead to electrical discharge to any electrical ground connection, i.e. arcing. The column of soldering pads on the PCB constitutes the dead area of the detector and acts as the boundary between adjacent sectors.

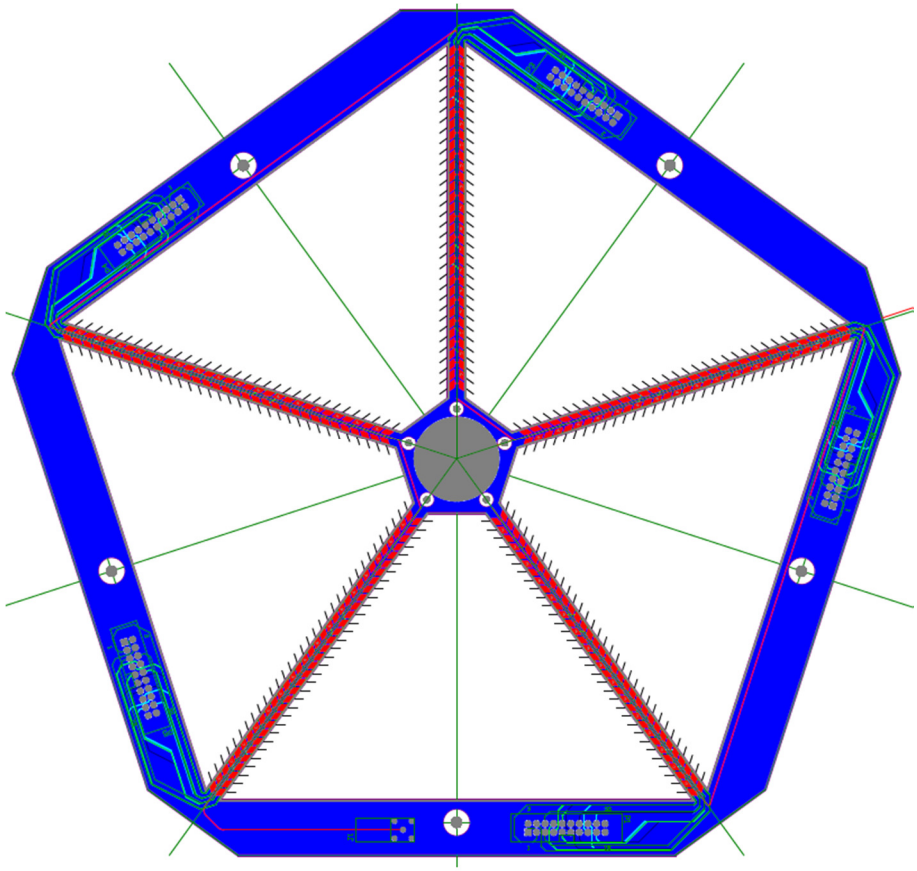

Figure 4.1: Design layout of the GATEAU PCB structure. Blue areas specify regions with a conformal coating, which is the origin of the green PCB colour (see section 5.1). It is so named since it conforms to the topology of the circuit board design. Its main function is to protect the PCB from water and chemical contaminants. Light-blue traces symbolise signal tracks to connector pins whereas the red trace indicates the HV track.

The multi-layer structure and multiple signal and guard wires complicate the internal PCB design. Electronic crosstalk and impedance matching of signal traces were necessary. Crosstalk is a side-effect of the inherent capacitance and inductance of the PCB tracks. Track capacitance is the ability of the tracks to store an electrical charge. Track inductance is the ability of a current in a track to induce an unwanted signal in a neighbouring track, known as crosstalk [54]. Inductance and capacitance for the PCB signal tracks were calculated [53] and depend on signal track lengths. Signal trace/track

length is defined in this case as the distance from the signal-wire landing pad to the corresponding IDC connector pin. Inductance and capacitance increase with increasing track length and were determined to be in the range of 16.15-63.97 nH and 6.11-24.21 pF, respectively. Track lengths range from 42.97 mm (outer signal wire) to 170.25 mm (inner signal wire). The internal structure of the PCB is shown in Figure 4.2.

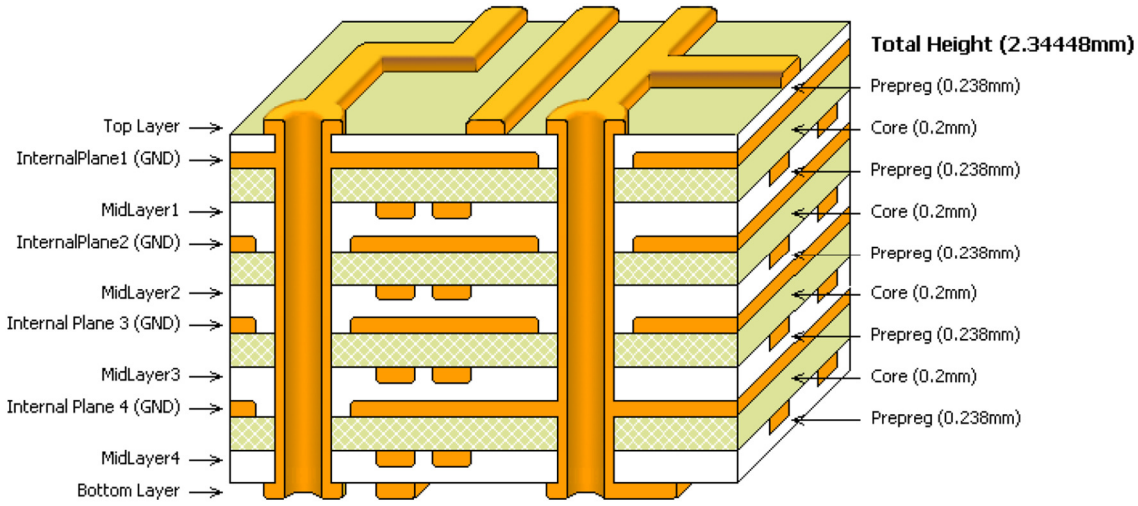

Figure 4.2: Internal, multi-layer structure of the GATEAU PCB [53]. The PCB has a total of 10 layers, with four signal tracks located within each midlayer. The total height is equavalent to the thickness of the PCB. A thickness of 2.34 mm makes the PCB strong enough to withstand the physical tension that will be applied by the 80 signal wires and 85 guard wires once soldered onto their respective landing pads.

The PCB has ten layers: a top and bottom layer along with four signal layers (midlayer 1-4) and four ground layers. Each signal layer has four signal tracks that are spaced 1.27 mm apart. Ground layers are placed in between the signal layers to achieve a higher track separation and to restrict crosstalk, as the induced electric field will couple to the ground plane rather than the signal tracks. Crosstalk can informally be defined, within the context of this study, as the phenomenon of unintended signal generation due to the flow of an electric current in adjacent signal tracks. Crosstalk is mainly generated by signal track impedance. Therefore, it depends on the distance between tracks (1.27 mm) and the distance that adjacent tracks run parallel to each other. The bottom layer functions as a ground plane. The top layer contains the HV trace and the landing pads for the guard and signal wires.

From calculations [53], the highest amount of crosstalk takes place between signal tracks 2 and 3, with the greatest parallel track distance at 140 mm. The crosstalk coupling coefficient was -50.5 dB. Signal tracks 15 and 16, with the lowest parallel track distance of 11.5 mm, had a crosstalk coupling coefficient of -72.2 dB. The calculation was performed using “UltraCAD Crosstalk Calculator” software.

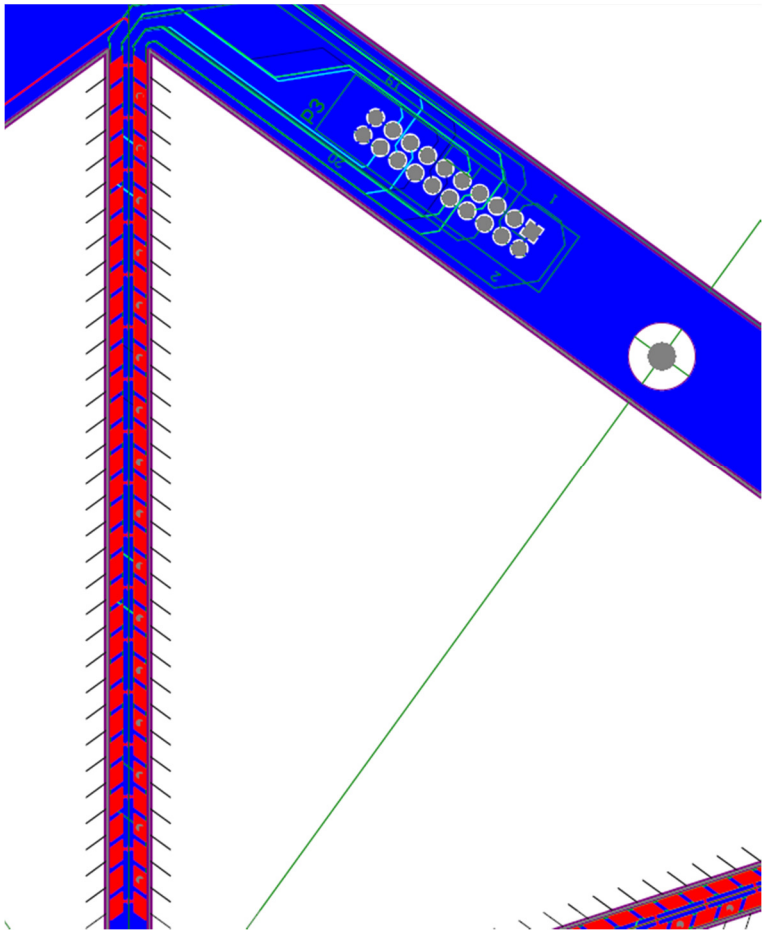

Figure 4.3: Close-up view of a PCB sector. Corners of the signal and guard wire landing pads were rounded in the design to prevent possible arcing. The right column of landing pads for each sector are regarded as anchoring pads since there are no signal or guard traces that flow from or to them, in contrast with the figure. They only serve as physical connection points for the signal and guard wires.

The measure of an electronic circuit to resist a change in current when a voltage is applied is called electronic impedance. Impedance matching refers to the process of equilibrating the signal track impedance with that of the Technoland preamplifier cards (see section 4.2). However, it was not possible for the PCB since the preamplifier cards have an impedance of ~300 Ω which was not possible to replicate in the signal tracks. The solution was to calculate the maximum allowed distances that the signals could travel before encountering impedance discontinuities [53]. Mismatches in impedance occur at impedance discontinuities and cause signal reflections that will give signal transmission irregularities, like ringing, where the same signal reflects multiple times through the transmission medium. A discontinuity will exist when the rise/fall time of the signal is less than, or equal to, the transmission time [50]. The transmission time is related to the signal transmission length which can be defined as the PCB signal track length plus the data cable length that connects the PCB to the Technoland preamplifier. The minimum allowed rise/fall time for the cards is 5 ns. The maximum cable lengths were calculated for 5 ns and 10 ns and applied to the experimental setup.

4.2 Preamplifier-Connector PCB Design

GATEAU is a modified, derivative version of the K600 VDC detectors. It was consequently possible to use a similar preamplifier design for GATEAU as is used for the VDCs. A total of 22 Technoland units are used for the X- and U- wire planes. The same preamplifier-connector PCB design was adopted, with the design having been modified to accommodate a total of 5 Technoland units [55], one for each GATEAU PCB sector. A diagram of the preamplifier design and how it relates to a Technoland unit is shown in Figure 4.4.

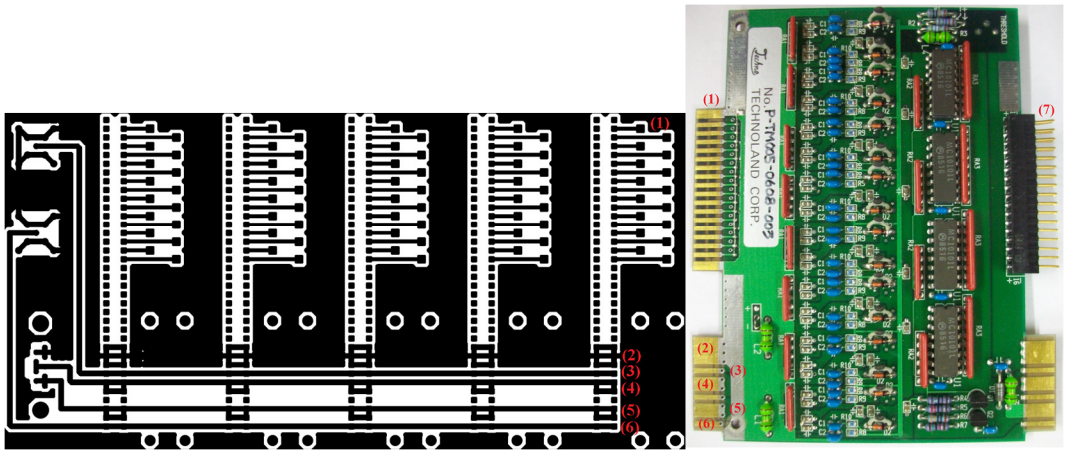

Figure 4.4: Diagram of the traces in the preamplifier-connector design. A photo of the Technoland preamplifier unit is shown to indicate the correlation between the two circuit boards. The Technoland unit has sixteen signal contacts (1) and a main ground contact (2) to the preamplifier PCB. The pulser contact (3), -5V contact (4), +5V contact (5) and threshold contact (6) are indicated. The amplified signal output is transmitted via a 34-pin connector (7).

Each GATEAU preamplifier-connector PCB hosts five Technoland units. They are individual 16-channel preamplifiers capable of providing signal amplification for the signal wires of one GATEAU sector. The preamplifier is powered by a ±5 V DC input via a 9-pin serial connector. Threshold and pulser signals are supplied by 5-pin BNC Lemo connectors. The centre pin of each connector supplies the signal. The outer four pins are connected to the ground. A full description of the components used to build the GATEAU preamplifier-connector PCB is given in section 5.2. The pulser Lemo connector is used to introduce an electronic signal to the preamplifier for testing. The threshold Lemo connector is used to connect to an EDA47 Wire Chamber Threshold Supply. The threshold supply is responsible for signal discrimination by means of differentiating between the signal pulse heights, in volts. The diagram in Figure 4.5 illustrates the effect and purpose of using a threshold supply unit.

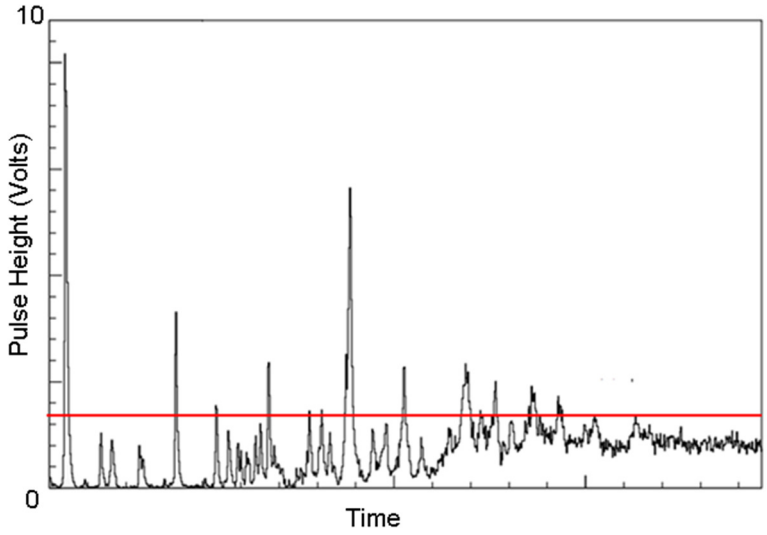

Figure 4.5: Wire chamber threshold supply diagram. The spectrum is only used illustratively to explain the function of a threshold supply. The EDA47 Wire chamber Threshold Supply unit is able to discriminate between electronic signals of a pulse height between 0-10 V. The red line in the figure symbolises a selected threshold. If the threshold is lowered, the preamplifier would accept pulses in the noise. If the threshold is increased significantly, many of the real events would not be detected.

4.3 Garfield: Electric Field Simulations

Garfield is a FORTRAN77 program developed at CERN for the simulation of electric and magnetic fields [56]. It was used to simulate the GATEAU PCB wire structure and the electric fields that exist within the confines of the PCB and cathode. An initial simulation that was developed to determine the breakdown voltages (voltage limit where the detector will electrically discharge) was unsuccessful as Garfield is not designed to calculate breakdown voltages. However, it is reasonable to anticipate that arcing may most likely occur at areas where the electric field is concentrated. This could easily be seen from the 3D simulations of individual PCB wire sections. The simulations assumed a potential of -500 V on the guard wires with the signal wires grounded. The wires in the simulation run parallel to each other with a distance of ~3-4 mm between adjacent signal and guard wires. Arcing from the guard wires to the signal wires was also a concern since it would result in fictitious data signals and would render the electric field established by the guard wires obsolete.

The Garfield simulations correctly suggested that arcing would not occur since no arcing related to a functional PCB was encountered during tests. Arcing only originated from a faulty high-voltage cable within the chamber and from the PCB when a wire strand broke. Arcing should only occur, therefore, when a fault has developed.

The simulations are based on the wire-structure of the PCB design. Garfield can simulate solid objects as well as charged wires. These two functions were combined to make a composite that consists of the GATEAU PCB with various guard and signal wires imposed upon it. It should be noted that Garfield is a single-threaded program. Therefore, the program was limited in the amount of charged wires that could be

simulated. For instance, the three-dimensional plot shown in Figure 4.9 was generated by inverting a square, 10^4-element matrix. As a result, the wire-structure PCB that is shown in Figure 4.6 only has twelve guard wires and eleven signal wires since larger wire sectors resulted in the simulation running for three days without any results. The signal wires are grounded while the guard wires had a potential of -500 V.

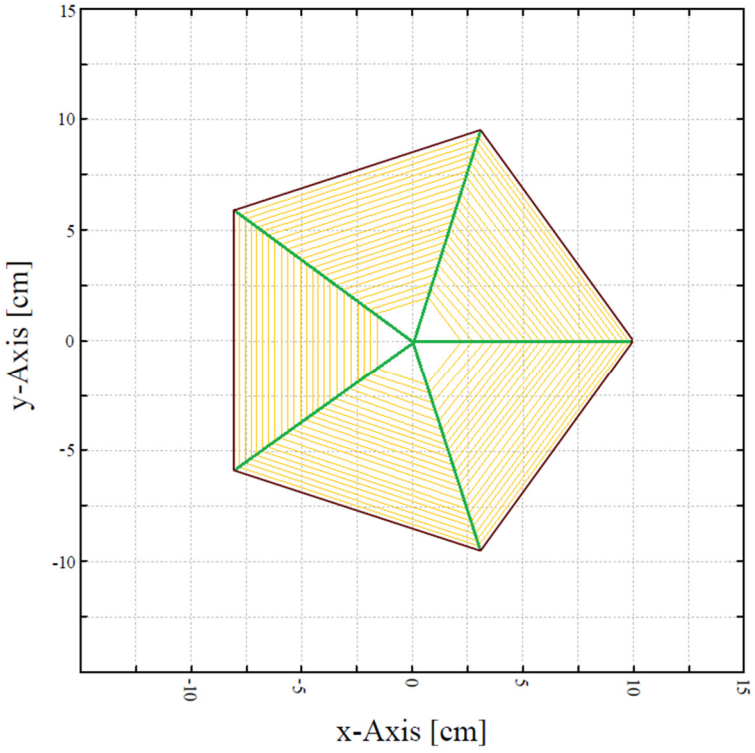

Figure 4.6: Simulated GATEAU PCB wire-structure. The simulation was carried out by imposing multiple signal wires and charged guard wires onto a solid frame. The solder pads of the PCB were not simulated. This construction served as the basis for some of the other simulations.

One of the main concerns that had to be addressed was whether the guard wires would electrically discharge to the signal wires given the wires are ~3 mm apart. The first step was to simulate the electric field lines of a 20-µm diameter guard wire. A cross-sectional view of this simulation is shown in Figure 4.7. However, simulating the field strength of an individual wire in isolation was not sufficient to address the potential arcing problem. Figure 4.8 shows a close-up view of the electric field lines when multiple guard and signal wires are simulated. It also shows the amplification and drift regions of the detector given the current parameters. The solitary red line that moves from the drift region to the amplification region in Figure 4.8 symbolises a drift electron moving under the influence of the electric fields of the detector when close to the PCB. The gas mixture used in the simulations was 90% Ne with 10% CO_2. The in-beam drift field will be ~500 V/cm for a pressure of 20-50 mbar. Given the dimensions of the active region, i.e. the cathode and anode being 10 cm apart, the simulated potential on the cathode was 5000 V. However, this was altered for simulations with different detection gasses and different active regions.

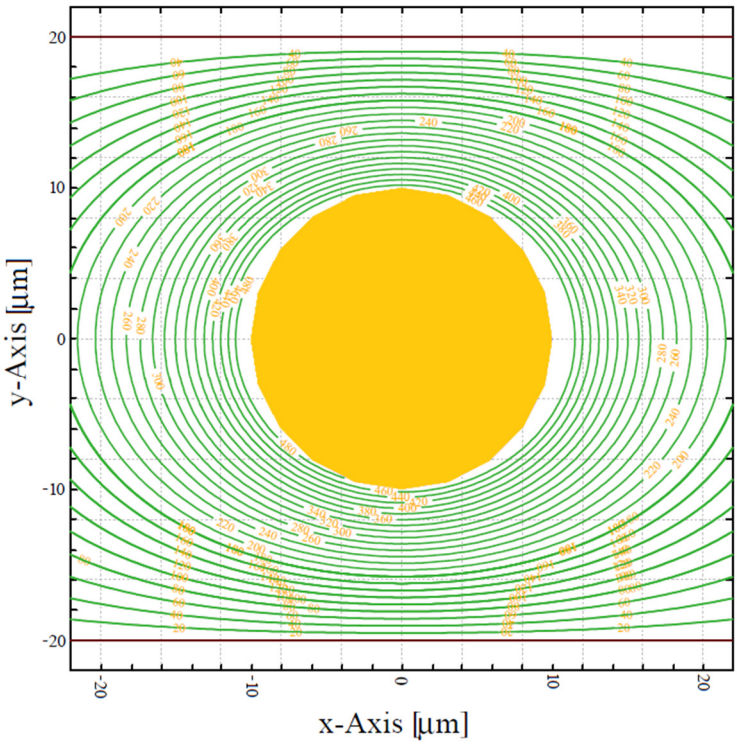

Figure 4.7: Simulated electric field lines of an individual guard wire. The field lines form equipotential contours, with the potential of each contour indicated. It can be seen that the electric field is relatively strong close to the wire and that it slightly weakens further away. The absence of radial symmetry can be attributed to the influence of adjacent wires.

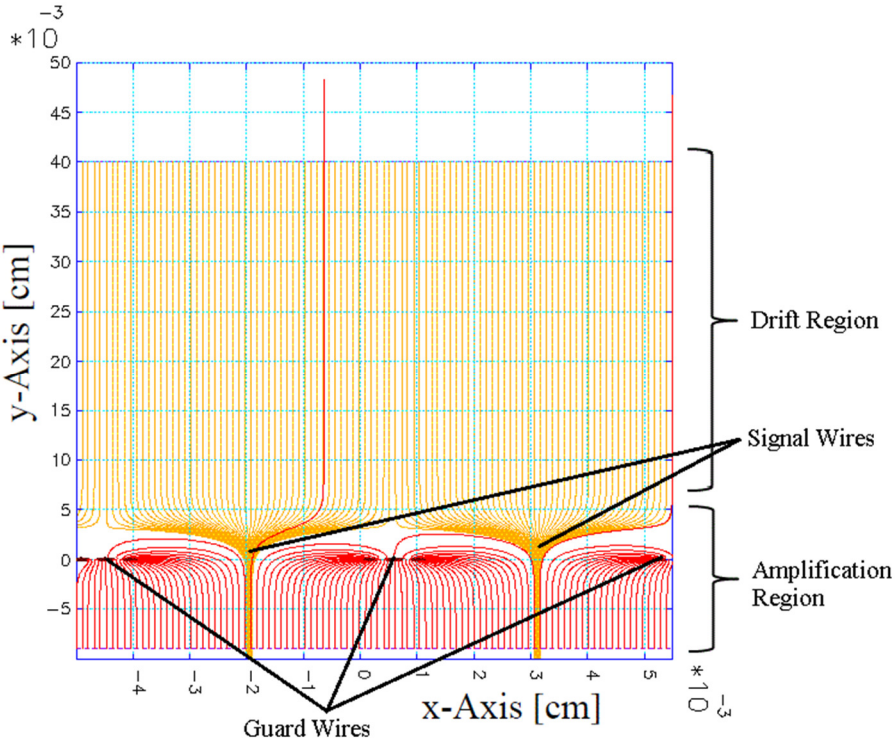

Figure 4.8: Simulation of the electric field lines set up by signal and guard wires. The wires are ~3 mm apart with the signal wires grounded and the guard wires with a potential of -500 V. It is evident that the guard wires, within the context of the simulation, are able to guide drift electrons to the signal wires.

The electric field lines that are established by the signal and guard wires can also be simulated in a three-dimensional environment. As stated earlier, it is reasonable to assume that arcing may most likely occur where the electric fields are most concentrated. The simulation in Figure 4.9 shows the extent of the electric fields and their arrangement. The simulation is calculation intensive and took multiple hours to generate. An attempt to simulate the three-dimensional fields of an entire PCB assembly, as shown in Figure 4.6, was unsuccessful given the large amount of processing necessary to compute and manipulate very large matrices in order to generate these types of figures in Garfield.

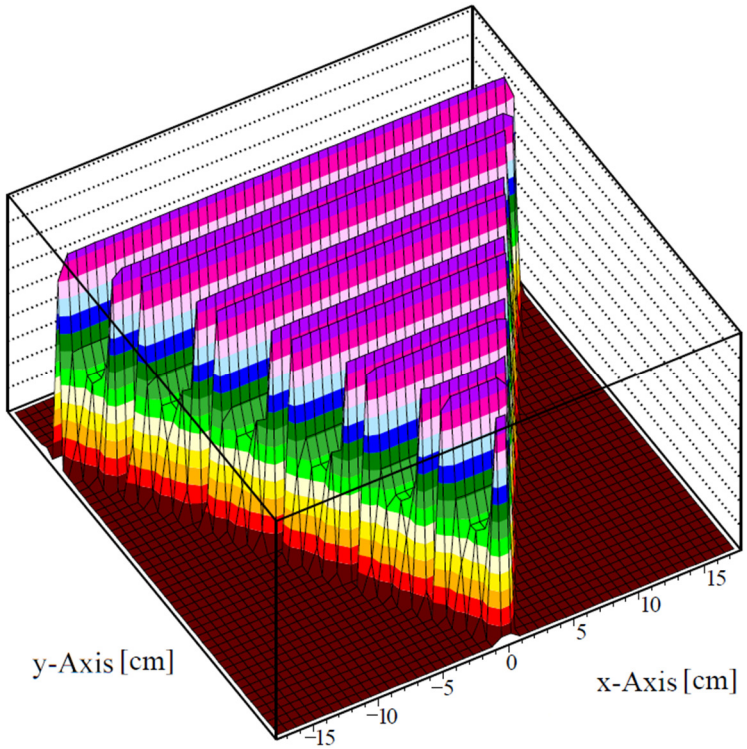

Figure 4.9: Three-dimensional simulation of the GATEAU PCB electric fields. Only one sector with twelve guard wires and eleven signal wires was feasible to simulate. It is evident that there are no extraordinarily concentrated fields that may lead to arcing.

The homogeneity of the electric field within the active region is an important aspect of GATEAU, as discussed in chapter 2. Simulations were carried out to determine whether the electric fields are homogenous at the edge of the active region. The wire-structure PCB was used in the simulation. A solid structure in the shape of the pentagonal PCB was simulated and used as the cathode. The distance between the cathode and PCB is ~10 cm since the active region can be up to 20 cm when using two PCBs. A side-view of the simulation is shown in Figure 4.10.One feature of the detector system that could not be easily replicated within the context of the simulation was the beam path through the detector system. Nevertheless, it is evident that the electric field is not even at the active-region boundary. A subsequent simulation was carried out with a field cage. The results are shown in Figure 4.10 and Figure 4.11.

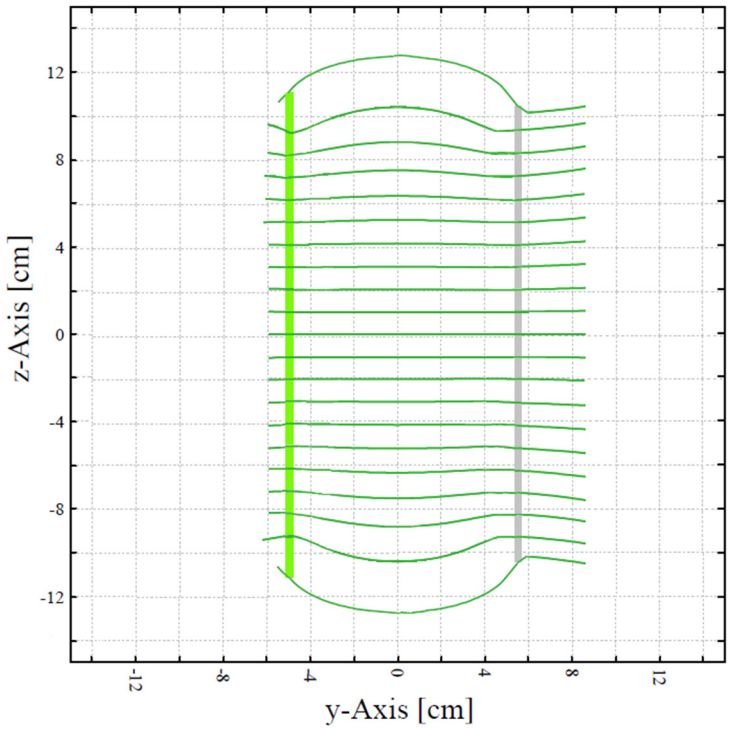

Figure 4.10: Side-view of the GATEAU drift-field simulation. The PCB is symbolised in green with the cathode in grey. A three-dimensional version of this simulation could not be executed. However, the simulation was able to indicate that a field cage was necessary for the detector system.

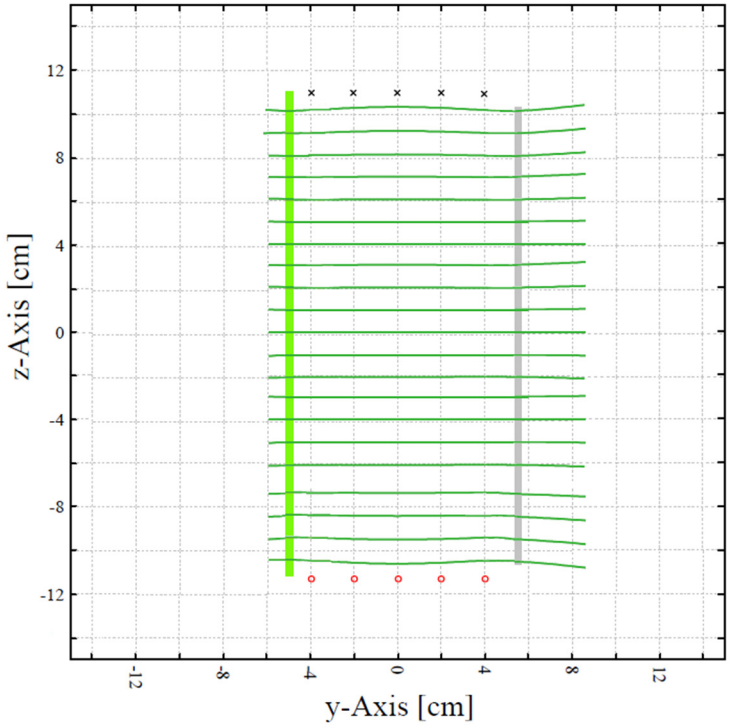

Figure 4.11: GATEAU drift-field simulation with field cage. The circles and crosses symbolise the charged wires of the field cage that go into and out of the yz-plane. The simulation shows that the addition of a field cage improves homogeneity of the electric field lines at the active-region boundary. This simulation is analogous to Figure 6.1.

It is also possible to determine various properties of the detection gas. The electron-drift velocity, drift time and diffusion coefficient can be simulated with Garfield and are shown in Figure 4.12 to Figure 4.14. It can be seen from Figure 4.12 that the increase in drift velocity is approximately linear with an increase in field strength. This deviates from Figure 2.3 given that Figure 4.12 does not include fields lower than 70 V/cm. The GATEAU drift field is 500 V/cm since the wire plane and cathode are 10 cm apart with a potential difference of 5000 V applied to the cathode.

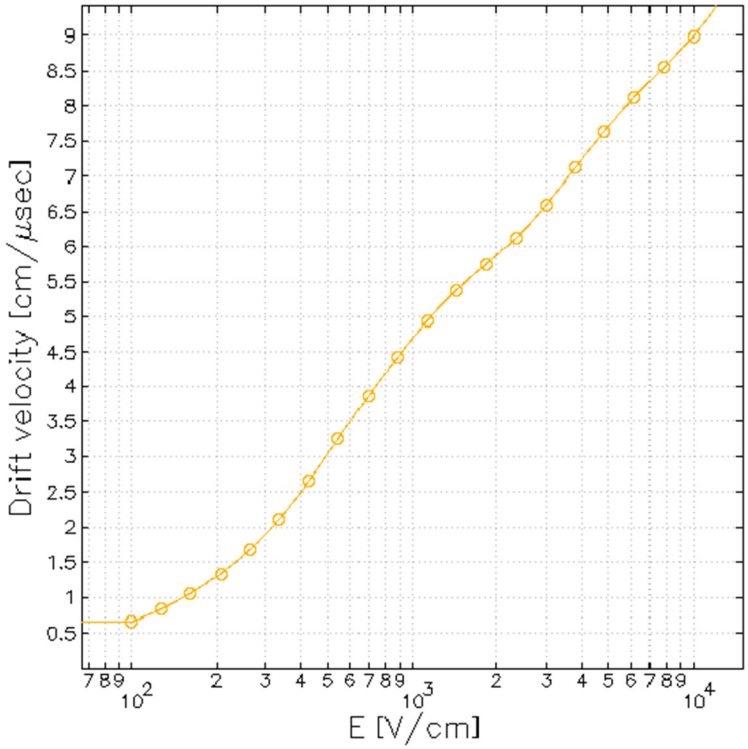

Figure 4.12: Simulation of the gas cell drift velocity. The Magboltz extension of Garfield was used to simulate a gaseous mixture of 90% Ne with 10% CO_2 at 50 mbar. The simulation agrees with the results of Figure 2.3 in predicting a 3.10 cm/μs drift velocity for an electric field of 500 V/cm.

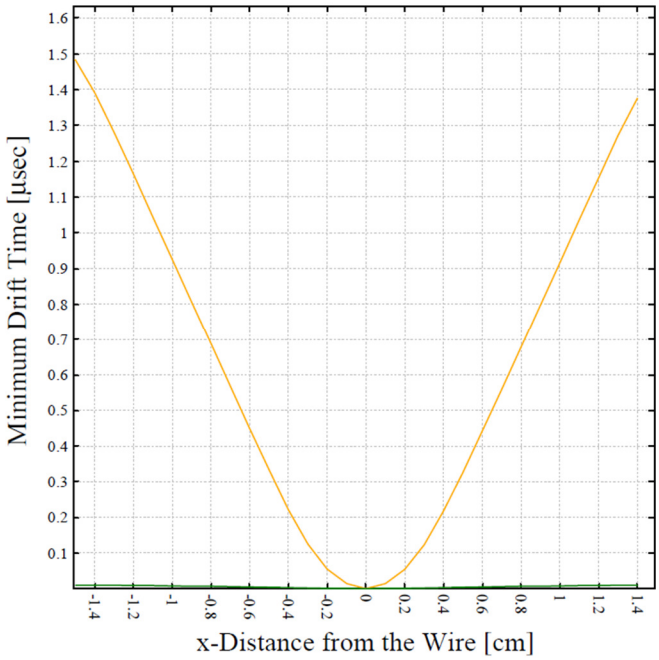

Figure 4.13: Simulation of electron drift time. It can be seen that the drift electrons accelerate as they approach the signal wires at ~0.2 cm as indicated by the graph. The graph was extended to simulate the PCB having a cathode on either side.

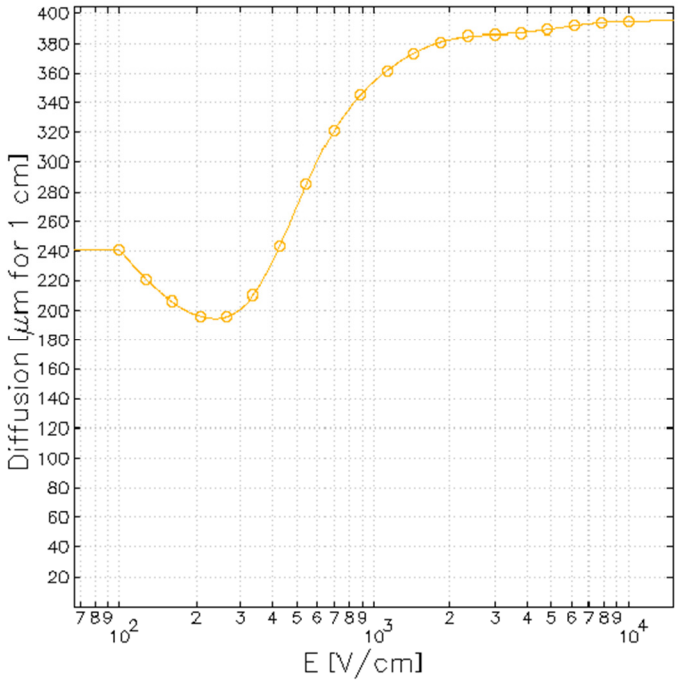

Figure 4.14: Simulation of the diffusion coefficient for a 90% Ne with 10% CO_2 gas mixture. This simulation also agrees with the results from literature [23], as shown in Figure 2.4. The diffusion coefficient is ~270 L^2T^{-1} for a drift field of 500 V/cm.

Chapter 5
Detector Construction and Gas Cell Tests

> "An expert is a man who has made all the mistakes which can be made, in a narrow field."
>
> Niels Bohr

In order to build a new detector system a problem-specific design has to be formulated. The proper implementation of that design is equally important. Many precautions were taken to build every component needed for the detector system properly and doing interim tests to ensure that all components work optimally. The equipment that was developed and built will be discussed in this chapter along with the various problems and consequent build restrictions that were encountered during assembly.

5.1 GATEAU PCB Assembly

The detector PCB was manufactured by Central Electronic Technologies after the design had been finalised. It has three component types: five 20-pin IDC connectors (20 mΩ contact resistance [57]), one Lemo HV female connector (50 Ω impedance [57]) and multiple 20-µm diameter wires. The unique structure and shape of the PCB required a new way of attaching thin detection wires to it. The solution was to manufacture a customised tool that was made in the shape of one of the trapezoidal PCB sectors. The "wiring tool", made of two separate halves, is shown in Figure 5.1.

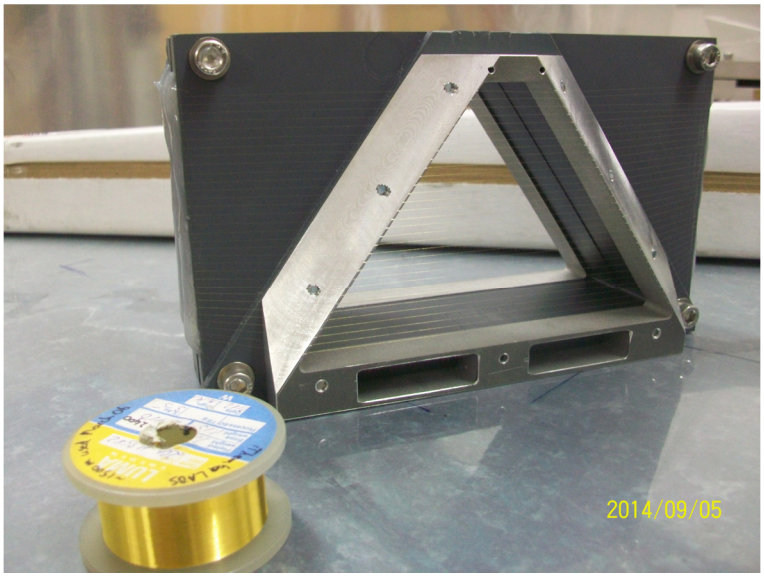

Figure 5.1: Completed wiring tool with a wire section spooled on it. The 20-µm diameter wires are spooled by hand and aligned by grooves in the tool. The tool is not effective when using 10-µm diameter wires which are too fragile.

The wiring tool design necessarily means that an unbroken wire strand has to be used. To completely spool it a 20-metre wire strand was used each time. The process begins by attaching one end of the wire to the side of the tool with a quick-setting epoxy. The other end of the wire was attached to a 60 g weight (10 g for 10-µm diameter wire) and set over a pulley. This ensures uniform tension across the wire and limits the risk of kinks which may lead to arcing when a potential is supplied to the field/guard wires. The weights used to obtain the correct tension were taken from the K600 VDC specifications [48]. The tool is then turned by hand multiple times until the end of the wire is reached at which point both edges of the tool are entirely glued with the epoxy. It is important at this stage to limit movement as much as possible. The weight stays attached to keep the tension in the wire until the epoxy has completely set.

After the wiring tool has been spooled it is separated into two. Each one of the halves is placed over an empty PCB sector which is kept in position by dowel pins. After soldering the wires to the PCB, they are still attached to the wiring tool. Long strands of excess wire extend beyond the pads as the sides are cut to separate the tool from the PCB. These have to be trimmed as close as possible to the solder, with a scalpel, to avoid sharp edges which may cause arcing.

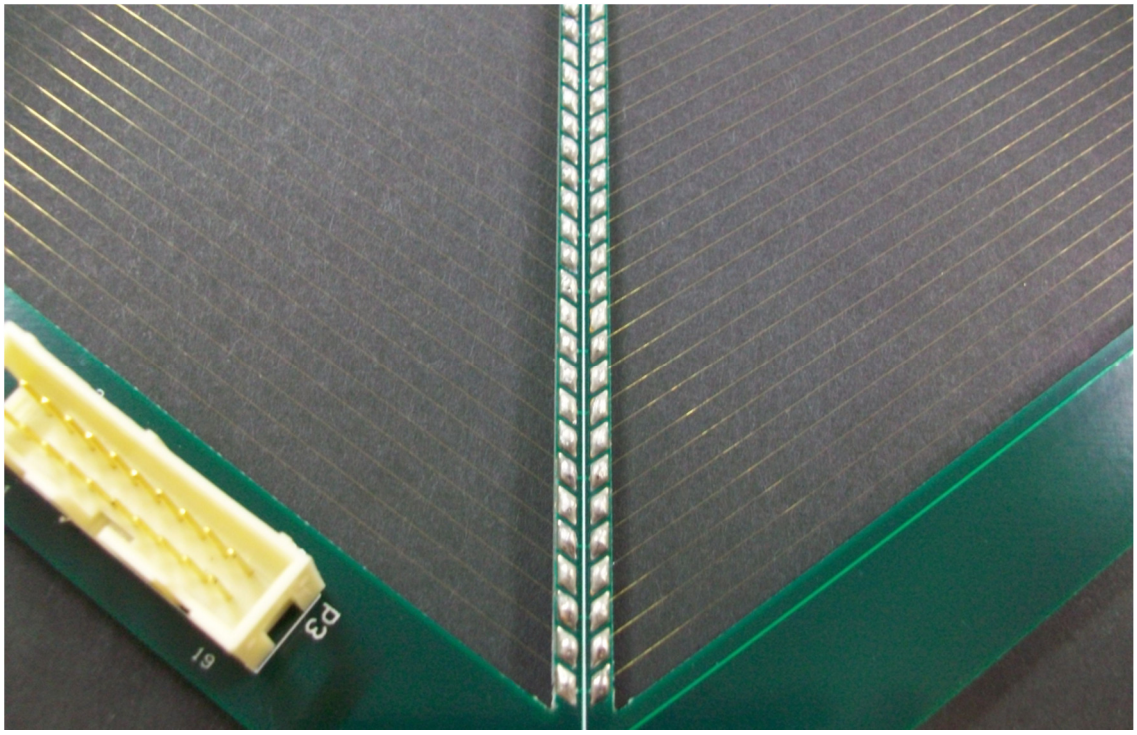

Figure 5.2: Signal and guard wires soldered onto the PCB. Great care was taken to ensure that the solder finish is smooth and that there are no protruding wire strands. The IDC pins were tested individually to ensure that each pin is electrically isolated from the others but electrically connected to the relavant signal wire. The ground pins of the IDC connectors were tested to ensure that they are electrically connected to the guard wires.

The wires used on the PCB are gold-plated tungsten alloys (3% rhenium) [58]. A lower soldering temperature of 290°C - 300°C was used in order to preserve the gold plating. For the same reason typical lead solder was not suitable. An indium alloy solder, with a lower melting point than standard lead solder, was needed to attach the signal and guard wires. One important difference beside the melting point is that it has no added flux [59]. A 5% ZnCl flux solution was added to the pads while soldering in order for the metal solder to attach to the PCB pads.

The solder flux also serves to smooth the soldering surface which helps to prevent arcing and has a reducing effect at high temperatures to remove thin oxide layers from the solder [59]. To remove the flux oil residue from the PCB, as well as dust and any other foreign contaminants, it was submerged in Safewash and rinsed with warm water. Safewash, which is an aqueous solution specifically for flux removal, consists primarily of alcohol ethoxylate, 2-aminoethanol and alkylbenzene sulphonic acid sodium salt [60].

A third, untested PCB has been constructed using 20-µm diameter guard wires and 10-µm diameter signal wires. The signal wires were mounted by hand without the use of the wiring tool since it was found that it is too fragile to spool. The use of thinner signal wires is beneficial mainly for two reasons: it decreases tension on the PCB structure and the electric field is stronger at the signal wires due to its smaller diameter (as a consequence of the $1/r^2$ dependence).

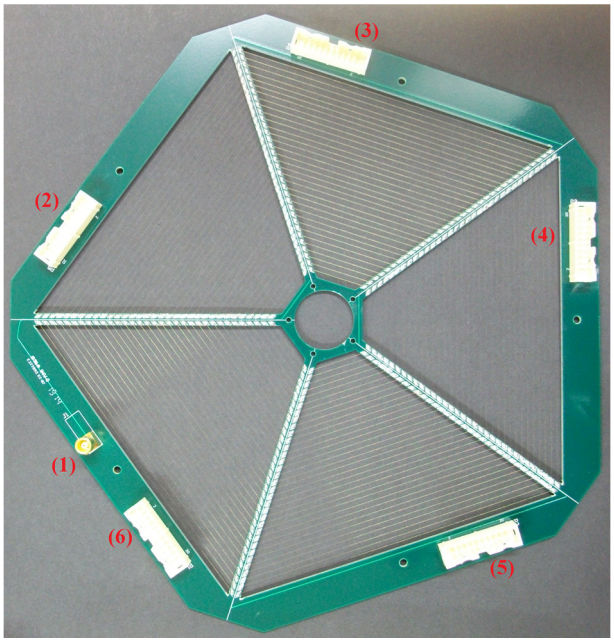

Figure 5.3: Completed 5-sector detector PCB. The PCB has one HV Lemo (1) connector that supplies all guard-wire pads with a potential difference. Each sector has one IDC connector (2)-(6) to relay signals from the 16 signal wires.

5.2 Preamplifier-Connector PCB Assembly

Each detector PCB has to have an accompanying preamplifier PCB since the current from the signal wires is very small (~μA). The preamplifier has few components but the quality grade of each component is still important. The card edge connectors, used to attach the Technoland-type preamplifier units to the PCB, needs to have contacts with low resistance. For this purpose, 34-pin CR22 type connectors with straight-through-hole pins were used. The grade-A connectors have a 2.54-mm pitch, a maximum current rating of 3A and a maximum contact resistance of 20 mΩ [61]. Standard lead solder was used for the card edge connectors and all other components on the preamplifier PCB.

Each Technoland preamplifier unit on the PCB is enclosed by copper shielding to limit electromagnetic (EM) noise pick-up. They are also electrically grounded through the shields to the preamplifier by copper contacts. When the K600 VDCs were first installed it was found that the preamplifier units are prone to EM interference which necessitated in the use of shielding [48]. The PCB preamplifier connects to a ± 5V DC power supply by a 9-pin serial connector. It also has two standard Lemo BNC connectors to connect to a wave pulse generator, for the purpose of testing the preamplifier, and a threshold supply unit. Five, 19-pin male Lemo connectors (max. current rating of 5A [62]) that carry data from the detector signal wires are connected to the 16 input channels of the five Technoland preamplifier units. A schematic of the PCB is shown in Figure 5.4. The completed preamplifier PCB assembly with the Technoland preamplifier units is shown in Figure 5.5.

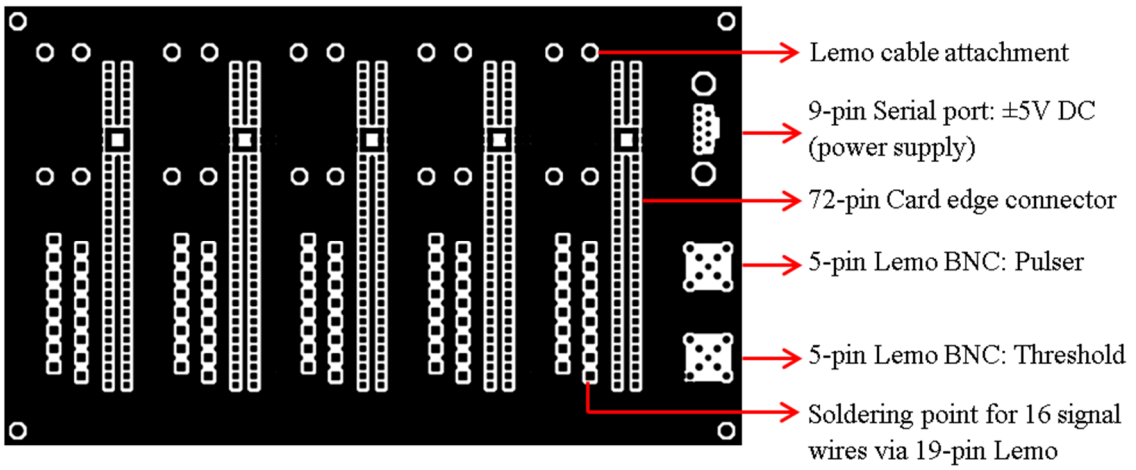

Figure 5.4: PCB schematic of the full preamplifier unit. The various contact points for the electronic components are indicated.

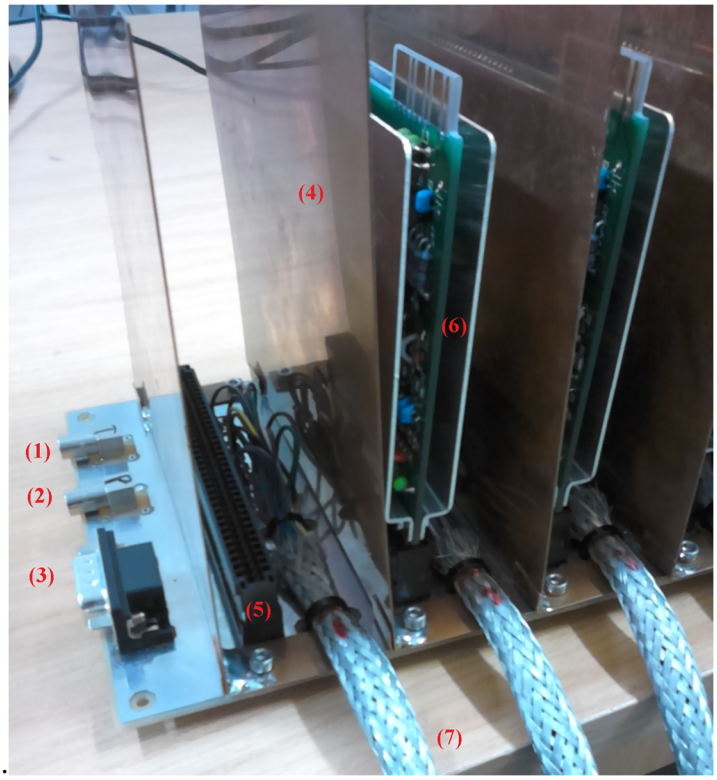

Figure 5.5: The completed preamplifier assembly. The pulser connector (1), threshold connector (2) and 9-pin serial power connector (3) are indicated. The preamplifier has six EM interference shields in the form of 0.5-mm thick copper sheets (4). It also has five card edge connectors (5) to connect to five Technoland preamplifier units (6). The Lemo cables (7) relay data from the detector PCB.

5.3 Gas Cell Tests: Gold and Carbon Microfilm

The construction of a functional gas cell for GATEAU necessitated the use of a micro-foil which would be needed as the entrance and exit windows of the gas cell. The main requirements were elemental purity, strength and to limit the leak rate of gas through the foil. Three candidates were identified: gold, carbon (as the graphite allotrope) and

Mylar. Each type is relatively inexpensive and readily available. Using an elementally pure microfilm was the primary goal. This limits the background and contamination present in in-beam data if gold and carbon were to be used. An extensive amount of work went into the investigation of suitable microfilms and their physical properties.

Carbon was quickly eliminated since a foil of ~200 µg/cm^2 was only able to withstand a differential pressure of ~1 mbar; the gas cell will have a differential pressure of at least 20 mbar relative to the beam line. Additionally, carbon foils were also unsuitable because multiple pinholes within the foils resulted in very high leak rates. Gold microfilm had a similar flaw. A gold foil of 14 mg/cm^2 was initially used and withstood a differential pressure of ~700 mbar with a low gas leak rate (~10^{-6} mbar.L/s). However, in an attempt to make the foil thinner, since beam energy loss through a 14 mg/cm^2 gold target is significant, it was rolled down to 1 mg/cm^2. For a thickness of 1 mg/cm^2 gold was already not suitable to sustain the needed differential pressure.

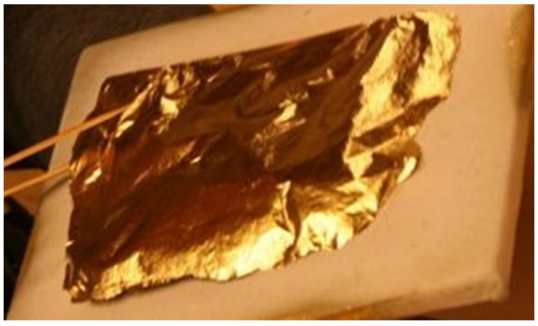

Figure 5.6: Example of the 14 mg/cm^2 gold microfilm used for the initial gas cell tests [63]. The thickness of all foils was determined by weighing a square piece on an analytical balance with a 0.1 mg resolution [64].

5.4 Poly(ethylene terephthalate) Microfilm Tests

Thin foils made of poly(ethylene terephthalate), commercially known as Mylar or PET with the chemical formula given as $(C_{10}H_8O_4)_n$ [65], was investigated as a possible solution for the gas cell entrance and exit windows. A well-known feature of Mylar is its strength, the factor absent for gold and carbon foils. However, Mylar does have drawbacks. Heating and radiation damage from a 200-MeV α beam will inhibit its ability to hold vacuum. It was known that additional tests would be necessary since it is not elementally pure like the gold and carbon microfilms and that it would have contaminants [66]. The polymeric molecular structure is shown in Figure 5.7 [65]. Various foils with thicknesses of 0.5 µm, 0.9 µm and 1.5 µm (measured as 75 µg/cm^2, 139 µg/cm^2 and 238 µg/cm^2 respectively) were tested.

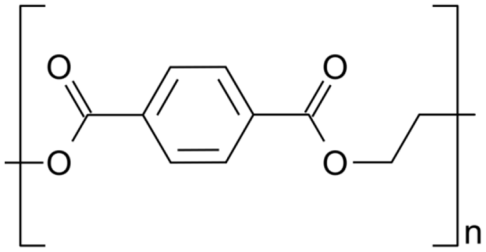

Figure 5.7: Polymeric molecular structure of poly(ethylene terephthalate) [65].

5.4.1 Differential Pressure Test

Mylar was first tested to find the typical differential pressures that each thickness could withstand. A customised experimental setup was assembled to test its potential to hold vacuum. The setup consisted of two vacuum sections with a leak valve attached to the sub-section.

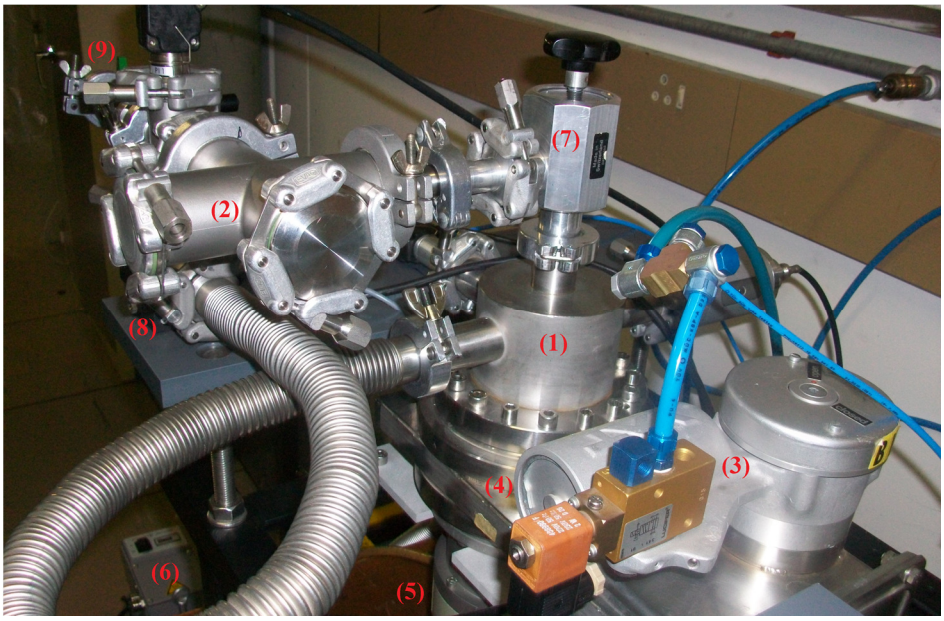

Figure 5.8: Experimental setup for the differential pressure tests. The setup is divided into a main vacuum section (1) and a sub-section (2) that are monitored by various Pirani and Penning vacuum gauges. An air valve (3) facilitated the use of a vacuum valve (4) to protect the turbo pump (5) and roughing pump (6) during tests if a foil should suddenly fail. The two vacuum compartments are regulated by hand valves (7) and (8). A leak valve (9) was used to raise the pressure in (2).

Each foil was placed between the sub-section (2) and the hand-valve (7). When the pressure reached ~10^{-5} mbar after pumping was initiated, the second hand valve (8) was closed. This, along with the foil, served to isolate the two chambers with the foil acting as a barrier between them. At this point, (4) was closed to protect the turbo pump and the leak valve was opened in order to raise the pressure of the sub-compartment slowly. Two different vacuum gauges were used in order to know the pressure of each section and to be able to measure a differential pressure. The leak valve was kept open until the foil failed.

A DN25 and DN40 connector, with openings of 25 mm and 40 mm in diameter respectively, were used to mount the foils. The leak rates were higher and the maximum differential pressures were lower when using the DN40 which is to be expected given the greater area of the opening. Only data from the DN40 tests are included since the entrance and exit window for the gas cell will have a 40 mm diameter. This is to ensure that the angular acceptance is greater than ±2° (angular acceptance of the spectrometer at 0° with a 49-mm diameter collimator). More importantly, this is to reduce scattering of α particles that have already elastically scattered from the target materials. Given that the distance between the two windows will be 20 cm, the angular acceptance will be ~±5°.

The results from the differential pressure tests are summarised in Table 5.1. The vacuum gauges use logarithmic pressure scales. Therefore the results are given to the nearest ten millibar. It is only necessary to know whether a particular foil can withstand differential pressures appreciably higher than 50 mbar, which is the limit that will be used in the gas cell. The average was taken for each foil.

Table 5.1: Results from the differential pressure tests. Each thickness that was tested is included in order to compare and contrast them. The data clearly shows that 0.5-µm thick Mylar was the best choice.

Microfilm	Thickness, µm	ΔP, mbar
Mylar	1.5	550
Mylar	0.9	390
Mylar	0.5	300

The 0.5-µm and 0.9-µm thick Mylar foils were tested further to know the rate at which gas leaks through the microfilm. It was found during the tests that some of the results showed a negative leak rate. The solution was to measure, and compensate for, the rate at which air leaks into the vacuum chamber itself. Given that the typical unit for gas leak rates is in mbar.L/s, it is necessary to note the change in pressure over a period of time. The volume of the sub-section had to be known and was measured to be 450 mL. The leak rate (LR) is given by:

$$LR = \frac{\Delta P.V}{t}, \tag{6}$$

where ΔP is the change in pressure in millibar, V is the constant volume of the sub-section in litres and t is the elapsed time in seconds, for a given pressure change. The results are shown in Figure 5.9 to Figure 5.11.

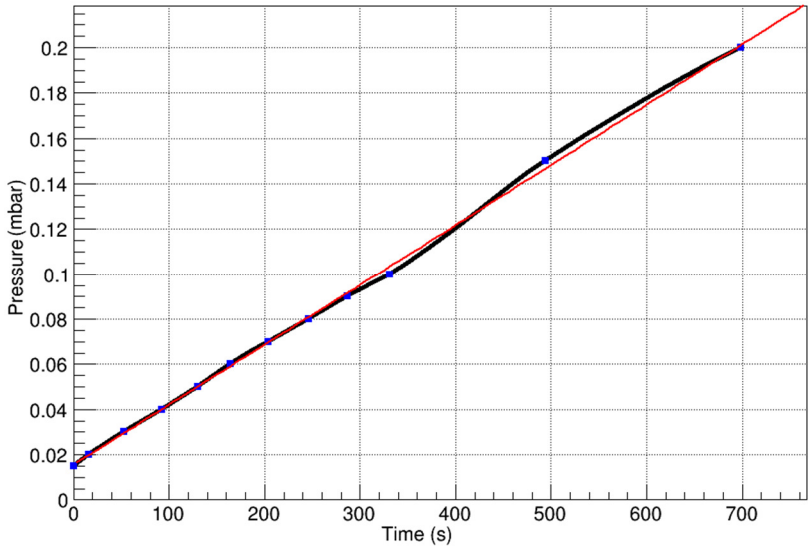

Figure 5.9: Leak rate (P vs. t) graph for the vacuum chamber.

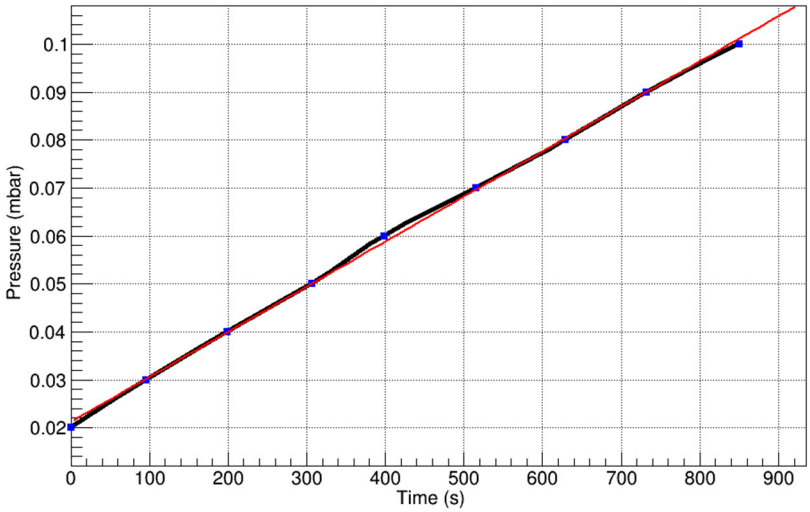

Figure 5.10: Leak rate (P vs. t) graph for 0.5-µm thick Mylar.

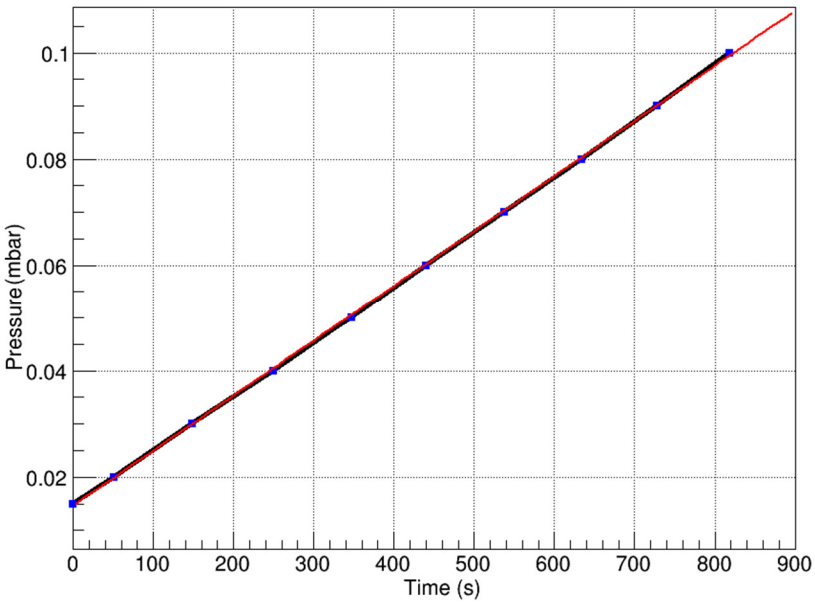

Figure 5.11: Leak rate (P vs. t) graph for 0.9-µm thick Mylar.

The linear leak rate shown in the graphs does flatten out as the two vacuum sections equilibrate. The leak rate for each foil is given by the product of the gradient and the chamber volume, subtracted from the chamber leak rate. The gradient of the linear fit taken from Figure 5.9 is 2.649 x 10^{-4}. The chamber leak rate was calculated to be $LR_{chamber}$ = 1.19 x 10^{-4} mbar.L/s. The gradient from Figure 5.10 is 9.415x10^{-5} which gives the leak rate for 0.5-µm thick Mylar: $LR_{0.5}$ = 7.66 x 10^{-5} mbar.L/s. Finally, the gradient from Figure 5.11 is 1.038 x 10^{-4} which gives the leak rate for 0.9-µm thick Mylar: $LR_{0.9}$ = 7.23 x 10^{-5} mbar.L/s. It is evident from the data that the leak rate does not scale with foil thickness. However, it shows that both foils are viable solutions for the gas cell given that the leak rates are relatively low.

5.4.2 Rutherford Backscattering Spectrometry

The Van de Graaff accelerator at iThemba LABS was used to collect RBS spectra for 0.5-µm and 0.9-µm thick Mylar. A 3-MeV proton beam was used with an average beam intensity of 1 nA. An S2-type double-sided silicon-strip detector (DSSSD) was used.

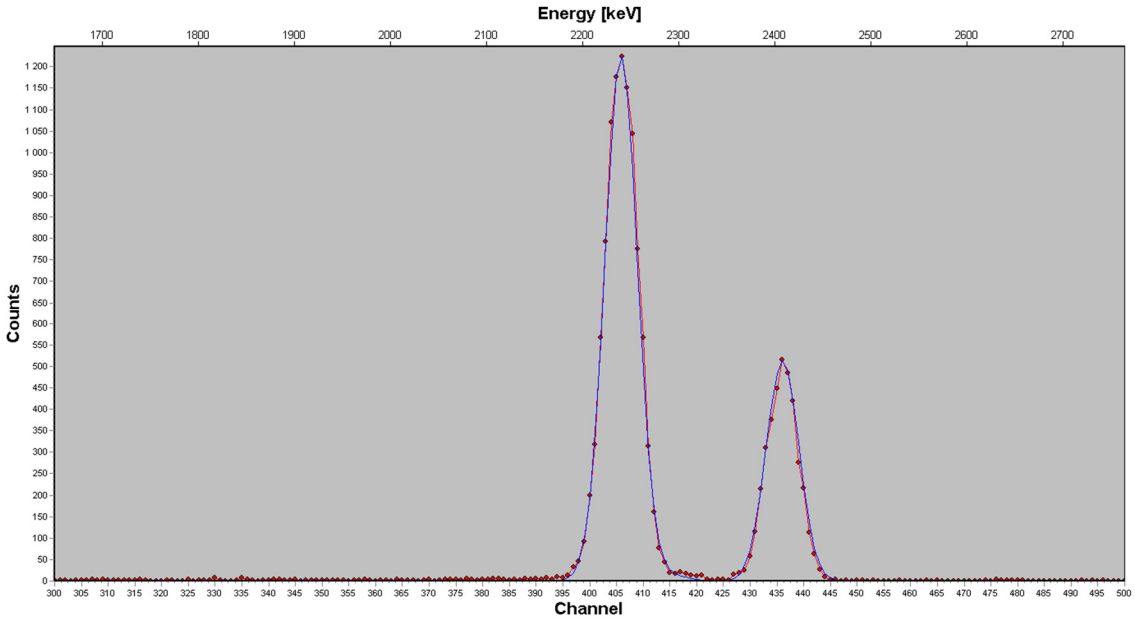

Figure 5.12: RBS Spectrum (red) of 0.5-µm thick Mylar ($C_{10}H_8O_4$) using a 3-MeV proton beam. The simulated spectrum, generated with simNRA [67], is shown in blue. The larger peak is ^{12}C and the smaller peak is ^{16}O. The relatively low background is an indication that Mylar has few contaminants. The FWHM is ~38 keV. The ^{13}C isotope can be seen as a shoulder on the ^{12}C peak. Using a molecular mass of 192.18 g.mol^{-1} for Mylar, the target thickness was determined to be 2.35 x 10^{17} atoms/cm^2.

As expected, the peaks for carbon and oxygen are dominant with the natural ^{13}C isotope also featuring in the spectrum as a shoulder on the ^{12}C peak. The background of the spectrum is low compared to the carbon and oxygen peaks. It is, therefore, evident that the number of contaminants in Mylar is low compared to carbon and oxygen. The RBS measurement was able to determine that the contaminant-level in Mylar is below ppm. This is possibly due to Mylar being a polymer. Contaminants are usually chemically inhibited from forming part of polymeric chains.

It has been observed by [66] that Mylar, besides its primary constituents, does contain chlorine as well as trace amounts of calcium and phosphorous. However, since GATEAU will be used for in-beam coincidence measurements with the K600, any contaminants introduced by the entrance and exit windows will not affect the measurements. It will be possible to gate on the events of interest with the Mylar windows lying outside the active region (see section 6.2). If the detector would have been used as a standalone detection medium, i.e. in a so-called singles measurement, a simple background subtraction would have been used. However, it is advantageous to have as few contaminant species as possible for a singles measurement. It was observed by [10] that the aramid gas-cell foils of PR196 contained many contaminants and necessitated a background subtraction that diminished the strength of the 22.5 MeV state (see Figure 1.2).

The spectrum in Figure 5.13 was taken during the ^{20}Ne(α,α')^{20}Ne* experiment of PR231 (see section 5.5). This would typically be used to do a background subtraction.

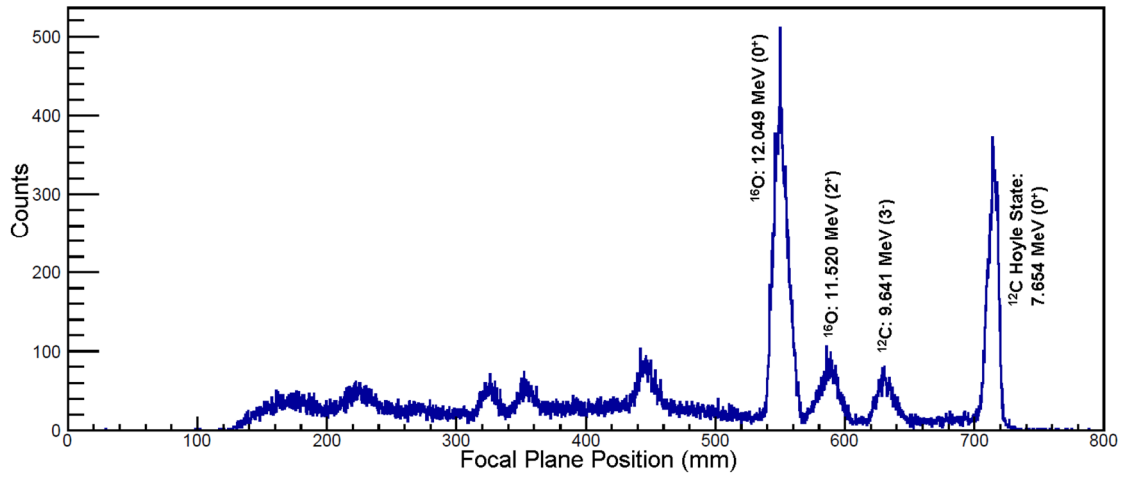

Figure 5.13: Mylar (α,α') focal plane position spectrum. T = 0 states from the primary constituents, ^{12}C and ^{16}O [1], dominate the spectrum given that (α,α') reactions are good T = 0 isoscalar probes.

5.4.3 In-Beam Foil Degradation Test

The gas cell windows will be irradiated for many hours during the course of a beam weekend by a 200-MeV α beam. Energy deposited by the beam will generate significant radiation damage within the gas cell windows. It was necessary to investigate the degradation effect of the beam upon it to know how long the windows may hold during a weekend given certain experimental conditions. If it was found that Mylar was unable to maintain proper vacuum after a few hours it would not have been a feasible solution since it would waste hours of beam time to replace them regularly. Therefore the Van de Graaff accelerator at iThemba LABS was used to investigate the radiation hardness of Mylar foils under conditions comparable to the GATEAU gas cell setup.

The experimental setup consisted of a mock-up gas cell with two guard vacuum cells on either side. The guard vacuum cells, as shown in Figure 5.14, are the physical mounts for the entrance and exit windows and were specifically designed for the

internal gas cell used in experiment PR231. The guard vacuum cell has a pipe so that the volume between the windows can be evacuated as gas leaks through the inner foils from the gas cell.

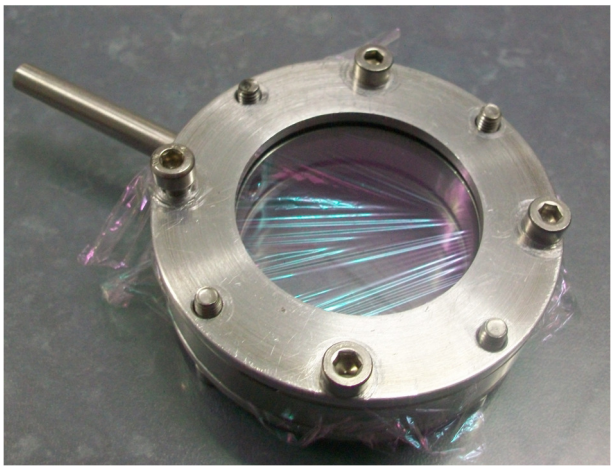

Figure 5.14: Guard vacuum cell for the internal gas cell used in PR231.

The gas cell pressure was set to equal typical in-beam experimental pressures, i.e. 20–50 mbar. A 3-MeV proton beam at an intensity of 50-60 nA was used. The basic gas cell setup within the scattering chamber is shown in Figure 5.15.

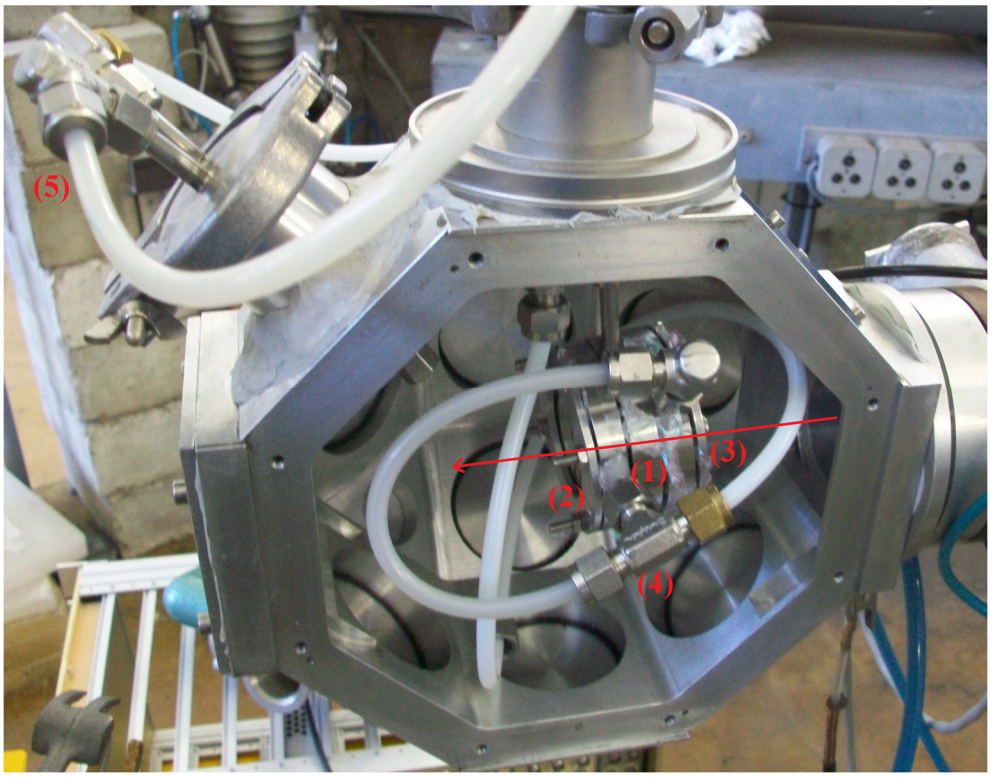

Figure 5.15: Mock-up gas cell (1) for the foil degradation test. Guard vacua on either side, (2) and (3), are shown within scattering chamber. The guard vacuum cells were connected (4) so that air that leaks from the gas cell into the guard vacua is pumped out (5). The beam direction is indicated by the red arrow.

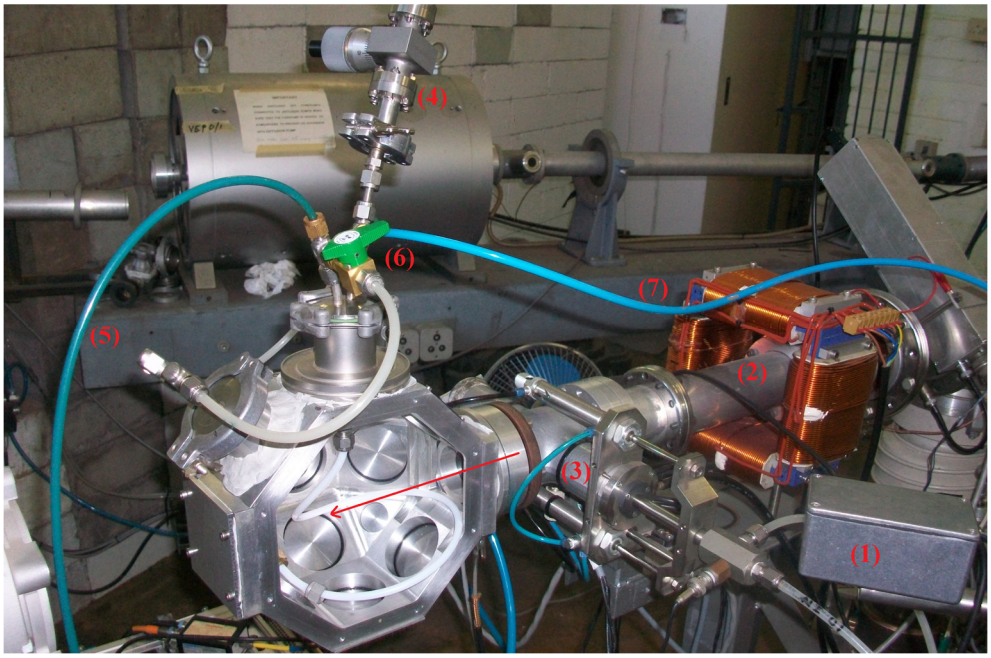

Figure 5.16: Experimental setup for the foil degradation test in the Van de Graaff accelerator D-line. The camera (1) is used along with the beam steerer (2) to align the beam, with a Faraday cup (3) to stop the beam. Air is introduced into the gas cell by means of a leak valve (4). Gas that leaks through the gas cell into the guard vacua is pumped out (5) by opening the gas valve (6). The pressure in the gas cell is monitored by Pirani gauges via the polyurethane pipes (7). The beam direction is indicated by the red arrow.

The full experimental setup outside the scattering chamber is shown in Figure 5.16. The polyurethane pipes that connect the gas cell to the roughing pump (and to the vacuum gauges) have a 0.95-cm inner diameter. Enough time was, therefore, allowed for the gas to reach equilibrium so the gauges would show the correct cell pressure. The 0.5-µm thick Mylar foils were tested. The results showed that significant damage was done to the foils in a relatively short amount of time, shown in Figure 5.17.

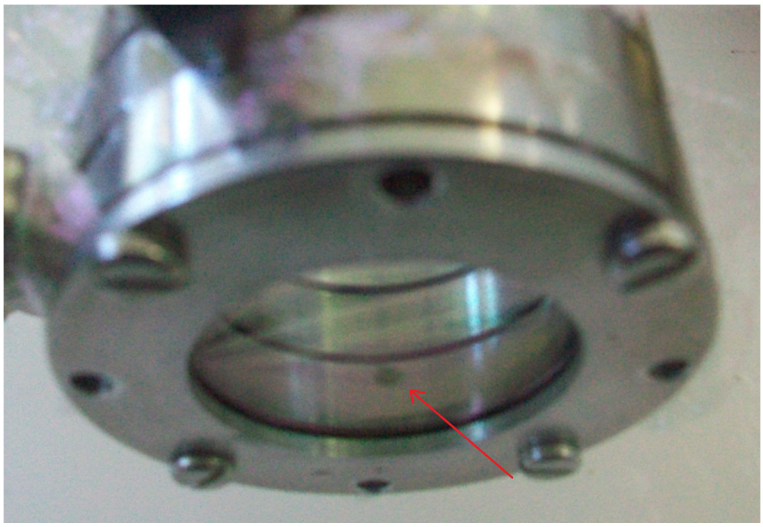

Figure 5.17: Beam damage to 0.5-µm thick Mylar. With the gas cell pressure at 50 mbar the foils held for 55 minutes while being irradiated by a 3-MeV proton beam at approximately 60 nA. The hole that was burned through the entire cell is indicated by the red arrow.

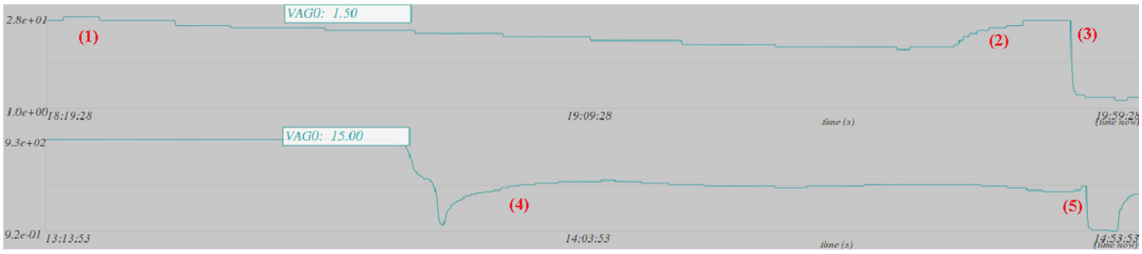

Figure 5.18: Pressure vs. Time graphs for the 20-mbar (above) and 50-mbar (below) test. For the 20-mbar test the gas cell was given approximately 28 mbar. The pressure in the gas cell dropped steadily and quickly due to radiation damage. The leak valve was opened in an attempt to raise the pressure to 20 mbar again (2) until the foil failed (3). The pressure in the next gas cell was raised to approximately 50 mbar (4). The pressure dropped steadily until it was manually raised with the leak valve (5). The foil failed shortly afterward.

The graph of the actual data taken from the experiment is shown in Figure 5.18. The pressure in the beamline was maintained at 10^{-5} mbar. The pressure in the gas cell was not precise due to the use of the leak valve. The starting point for the 20-mbar test extends beyond (1) in Figure 5.18. The beginning of the test was noted at 18:02. The time between failure and starting pressure can be seen on each graph. The primary results are summarised in Table 5.2.

Table 5.2: Main results from the in-beam foil degradation tests. The elapsed time before the foils developed a significant leak is given in column two. The failure time in column three shows the total amount of time elapsed until the foils were unable to retain any gas.

Gas Cell Pressure, mbar	Leak: Time, min	Failure: Time, min
20	115	120
50	50	55

The time measurements given in Table 5.2 are approximate. From the discussion that follows, it is shown that a 3-MeV proton beam with an intensity of 60 nA does significantly more damage than a 200-MeV α beam would at a maximum intensity of 1 nA. It is therefore only necessary to know the foil-failure time to within a few minutes.

The Bethe-Bloch Formula is used to calculate the stopping power, in MeV.cm^2/g, of a given incident beam particle onto an elemental material:

$$-\frac{dE}{dx} = \frac{4\pi e^4 z^2}{m_0 v^2} NB, \tag{7}$$

where

$$B = Z\left[\ln\left(\frac{2m_0 v^2}{I_{av}}\right) - \ln\left(1-\frac{v^2}{c^2}\right) - \frac{v^2}{c^2}\right]. \tag{8}$$

The variables are defined in Appendix A [68]. A numerical solution is implemented to calculate the stopping power in compound materials, with data fitted to experimental values at low beam energies [69], using the Bragg law. The NIST database was used for the calculations.

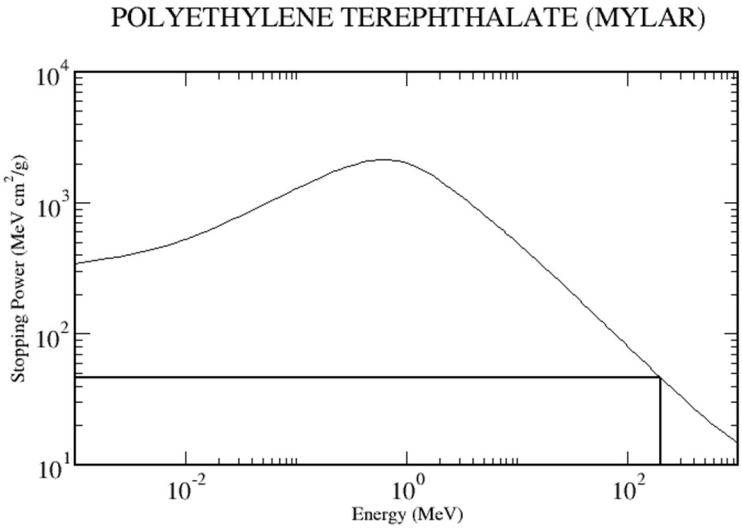

Figure 5.19: Stopping power of an α beam in Mylar. 200 MeV is indicated on the graph to show the corresponding stopping power.

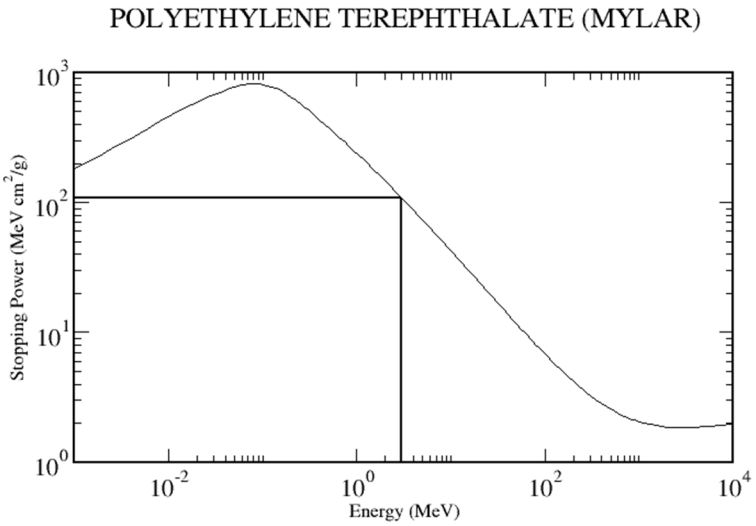

Figure 5.20: Stopping power of a proton beam in Mylar. 3 MeV is indicated on the graph to show the corresponding stopping power.

The stopping power of a 200-MeV α beam is ~48 MeV.cm^2/g (from Figure 5.19) compared to ~110 MeV.cm^2/g for a 3-MeV proton beam (from Figure 5.20), i.e. roughly two times greater. The beam intensity used during the Mylar degradation test was 60 times higher than 1 nA (absolute maximum) that will be used for in-beam tests of GATEAU. Therefore, based on radiation damage considerations, the foils should last more than 24 hours even with the gas cell at 50 mbar. This was confirmed during experiment PR231.

5.5 The PR231 ^{20}Ne(α,α')^{20}Ne* Experiment

The PR231 ^{20}Ne(α,α')^{20}Ne experiment was conducted in October 2014. The aim was to investigate the 20-25 MeV excitation region in an effort to continue the search for the 0^+ 5α cluster state. A considerable portion of time of the GATEAU project was dedicated to this experiment since it provided valuable insight into the functionality of a ^{20}Ne gas cell using Mylar entrance and exit windows with a 200-MeV α beam. The experiment was also relevant since it was a coincidence measurement with the spectrometer at 0° to investigate the dominant ^{20}Ne* decay channels. Finally, it served as the primary reason for building a specialised ancillary detection unit for the K600.

5.5.1 Experimental Setup

The experimental setup used an enriched-neon gas cell with four W1-type double-sided silicon-strip detectors (DSSSDs) inside the cell as shown in Figure 5.21.

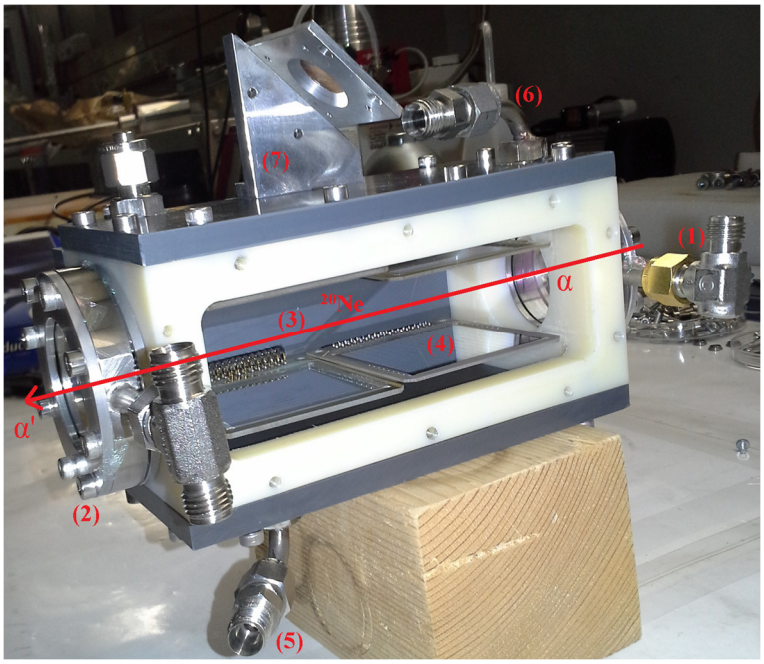

Figure 5.21: Internal gas cell for the ^{20}Ne(α,α')^{20}Ne* experiment. The gas cell has two entrance and exit windows (0.5-μm thick Mylar) on the upstream (1) and downstream guard cell (2). The ^{20}Ne volume within the cell, between the guard vacua, is defined as the target region (3) with the silicon detector array (4) surrounding it. The gas target is pumped in/out through the gas inlet (5) and outlet (6). A ZnS viewer (7) was used to tune the beam.

In this experiment the gas within the cell only served as a target. In this regard it is fundamentally different from GATEAU which uses the gas as the detection medium as well as the target. In doing so, a charged particle need only to move within the GATEAU active region after decaying from the parent nucleus. During PR231 the recoil nuclei had to move through the gas target and dead layer of the DSSSDs before being detected via the creation of electron-hole pairs. The energy threshold of silicon detectors is relatively high due to the dead layer and electronic limitations [70, 71] making it impossible to detect α particles with an energy of less than E ~650 keV. The

detection threshold of 400-µm thick DSSSDs is ~800 keV [72]. Additionally, the nuclear interaction point within the PR231 gas cell is not known making it impossible to compensate for the energy loss through the gas.

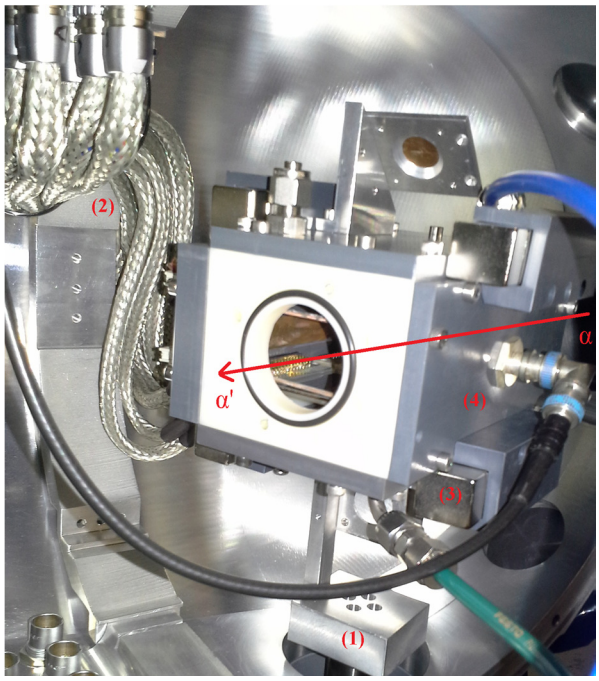

Figure 5.22: The ^{20}Ne gas cell within the small-angle mode scattering chamber. The gas cell was placed on the target ladder (1) to move it vertically for beam tuning. Each of the silicon detectors were connected to 34-pin IDC feedthroughs in order to transmit data out of the gas cell via the lemo feedthrough cables (2). Magnets (3) and an internal wire cage connected to a BNC feedthrough (4) were used to deflect high energy electrons away from the silicon detectors.

It is known that α-cluster states lie near the corresponding decay threshold [7]. The 5α decay threshold at 19.17 MeV would, therefore, be located in the 200-220 mm region in the focal plane position spectrum of PR231, as shown in Figure 5.23. At higher excitation energies many decay channels are open. It then becomes more likely that the background would shroud the decay of interest due to the overwhelming amount of unrelated events within the same energy region. All of these observations indicate that a specialised detection unit is necessary in order to study the 5α state.

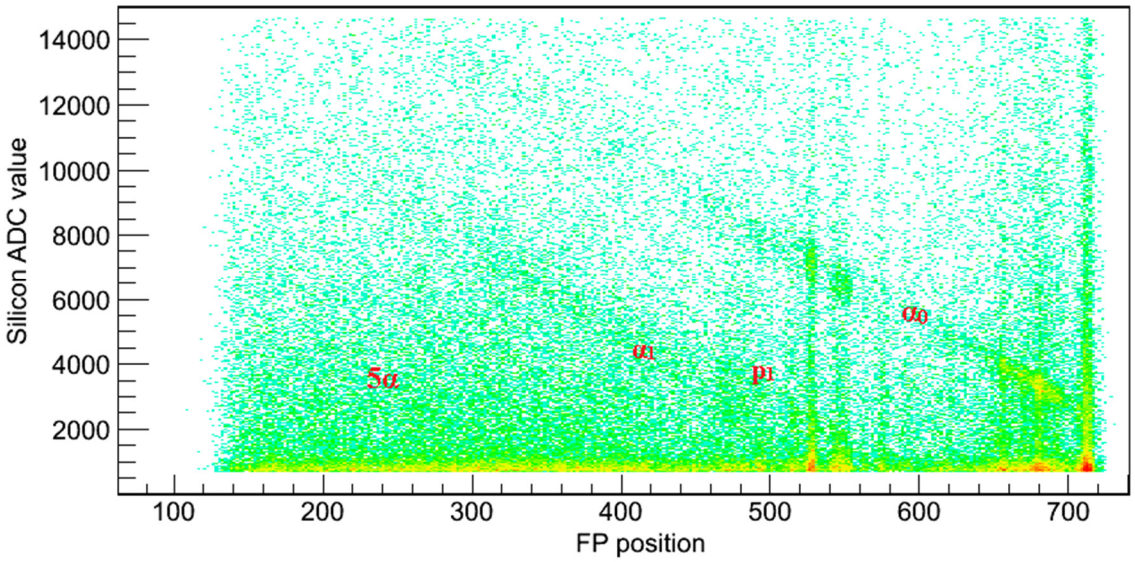

Figure 5.23: Silicon energy vs. focal plane position coincidence spectrum for ^{20}Ne(α,α')^{20}Ne*. The plot was generated during the experimental weekend with preliminary, online data. The spectrum is not time gated and without silicon front/back correlation. The various decay channels indicated are: ^{20}Ne* → ^{16}O (ground state) + α_0 and ^{20}Ne* → ^{16}O (0_2^+) + α_1 and ^{20}Ne* → ^{19}F (ground state) + p_1.

5.5.2 Gas Recycling Assembly

Enriched neon (99.5 % pure) was used for experiment PR231. It is relatively expensive at a cost of ~R2000/L. A gas recycling system was developed as a result to recycle any neon that leaks through the inner Mylar foils of the guard vacua. Natural neon that consists of 90.48% ^{20}Ne, 0.27% ^{21}Ne and 9.25% ^{22}Ne will be used for the GATEAU ^{20}Ne(α,α')^{20}Ne* experiment. It is significantly cheaper at ~R10/L and does not warrant the use of a gas-recycling setup. However, other potential isotopes that may be studied with GATEAU are listed in section 6.2.5 and include ^{21}Ne and ^{36}Ar which are very expensive and justify the use of a specialised recycling system.

The most important part of the assembly is the Zeolite molecular sieve. Type 5Å sodium-calcium aluminosilicate pellets were used for the adsorption of gaseous pollutants onto its surface. The 5Å-diameter pores are small enough to trap pollutants like O_2, CO_2, N_2 and H_2O but still large enough to poorly adsorb small, mono-atomic gasses like neon. The pellets are cylindrical with a diameter of ~1.6 mm and a length of 5-10 mm.

The process of adsorption occurs when a molecule, in gaseous or liquid form, adheres to the surface of another substance. Desorption is the opposite effect and was exploited to release pollutants from Zeolite before the experiment began. A cryogen (liquid nitrogen) was brought into contact with Zeolite to facilitate cryosorption which improves gas trapping. The adsorption potential is improved as gas is able to condense onto the cold Zeolite pellets [73].

Porous adsorbers, like Zeolite, typically have large molecular structures. A CAD drawing of the Zeolite used in the experiment is shown in Figure 5.24. It has a large internal surface area with its molecular pores in the order of atomic sizes [73]. The cavities are uniform and their size depends on the crystalline type of Zeolite used.

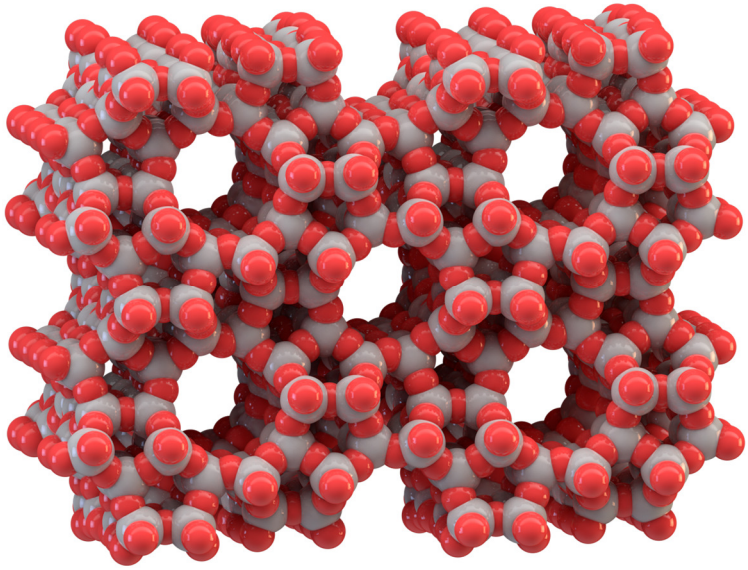

Figure 5.24: 3D molecular structure of the crystalline sodium-calcium aliminosilicate [74]. This type of synthetic Zeolite has a pore opening of 5Å. The pores are clearly visible.

Figure 5.25 illustrates the experimental setup of the assembly. The pressurised ^{20}Ne gas bottle was connected to a pressure regulator in order to maintain the gas cell pressure at ~20 mbar. Neon that leaks into the guard vacua was pumped out and into the bellow that contains the Zeolite. The recycled neon that is able to pass through the Zeolite is pumped back into the gas cell by a drag pump. A standard turbo pump was not used since drag pumps can run at higher differential pressures. The Swagelok valves in the system were set up so that the recycled ^{20}Ne is pumped into the gas cell at the required pressure which varied between 20-50 mbar. The illustration includes a residual gas analyser (RGA) that was located past the Zeolite sieve. It was used to detect the gas species that were able to pass through the Zeolite during recycling as well as to monitor gasses that were released by the Zeolite during desorption (see Figure 5.28). The assembly in Figure 5.25 includes components that were used to fill the Dewar with liquid nitrogen. Photos taken of the setup during experiment PR231 is shown in Figure 5.26 and Figure 5.27.

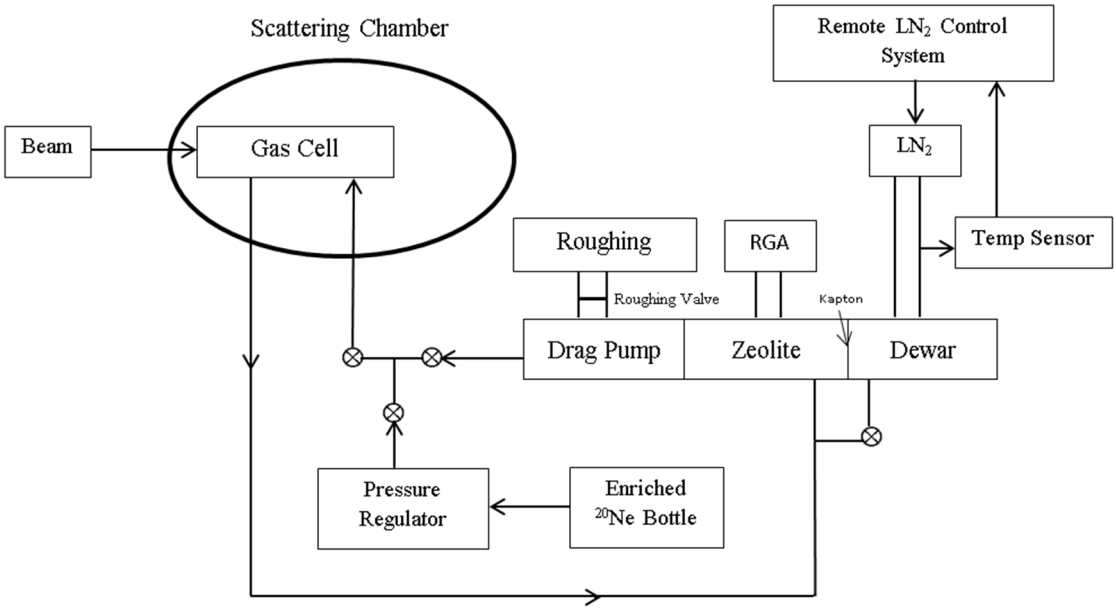

Figure 5.25: Schematic illustration of the gas recycling assembly used for PR231. Each cross represents a Swagelok valve. The arrow heads indicate the gas-flow direction. Various pressure sensors were used but are not indicated.

Figure 5.26: Gas recycling assembly for PR231. Enriched neon is fed from the gas tank (1) to the pressure regulator (2). The Zeolite pellets are placed inside the pipe (3) which is attached to the Dewar (4). The Dewar input valve and the PT100 temperature sensor are indicated as (5) and (6) respectively. Gas that is able to pass through the Zeolite sieve is monitored by an RGA (7) in order to determine whether pollutants were trapped efficiently. The gas that is able to move through the sieve is pumped back into the gas cell via the drag pump (8).

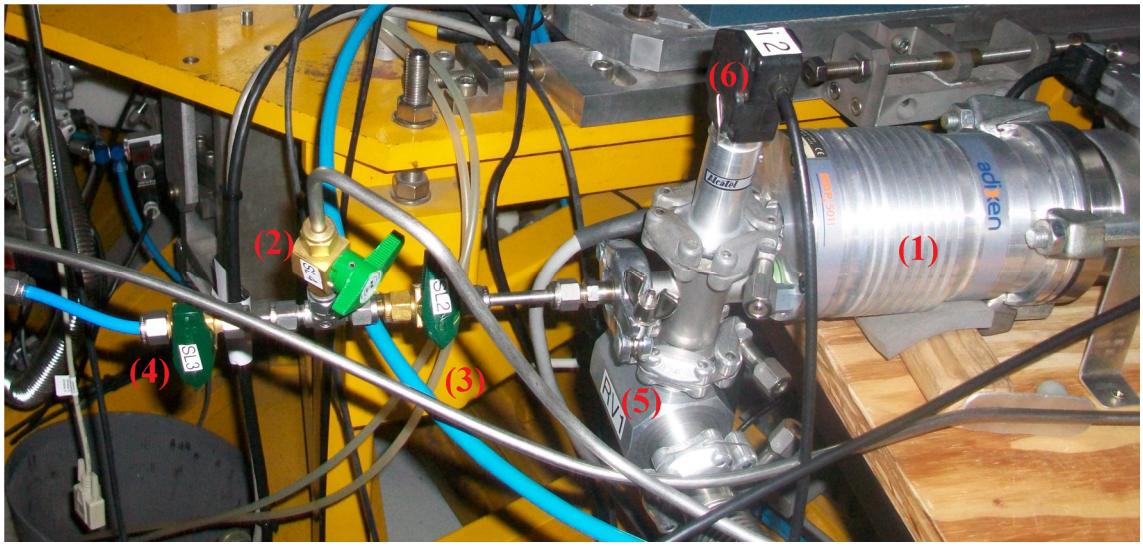

Figure 5.27: Drag pump (1) and Swagelok valve (2-4) setup of the recycling assembly. The roughing pump valve (5) is opened when the system is purged. A vacuum gauge (6) monitors the pressure of the gas that is pumped back into the gas cell. The valve at (2) is connected to the pressure regulator whereas (3) allows the recycled gas back into the system. The valve at (4) can be closed to stop gas flowing into the gas cell. This is done when an empty gas-cell run is needed.

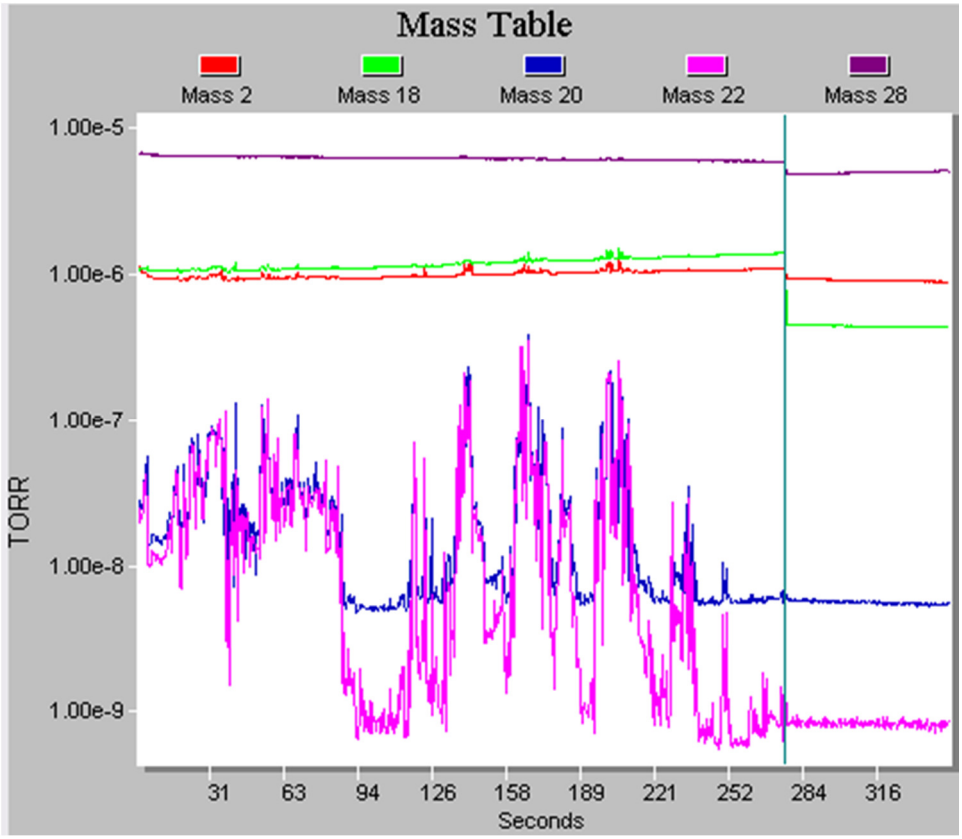

Figure 5.28: Output from the RGA during experiment PR231. The mass values correspond to the atomic masses of selected gas species detected by the RGA. Mass 2 is H_2, mass 18 is H_2O, mass 20 is ^{20}Ne, mass 22 is ^{22}Ne and mass 28 is N_2. The RGA is capable of detecting partial pressures as low as 10^{-14} Torr (1 Torr ≈ 1.33 mbar). Only gasses that can pass through the Zeolite can be detected by the RGA. In this instance, the Zeolite was being heated for the purpose of desorption before the experiment.

5.5.3 Extended Gas Cell Considerations

From observations made by [10, 11] it was known and anticipated that an extended gas cell would affect the focal plane data. The particular cell used in [10] was 10-mm thick with 6-µm thick Aramid windows. The effect was amplified for PR231 since each guard-vacuum cell was 10-mm thick with the gas cell being 17.5 cm in total length. This effect is important and relevant given that the gas cell for GATEAU will be 20–25 cm. Consider a standard scattering angle vs. focal plane position spectrum in Figure 5.29:

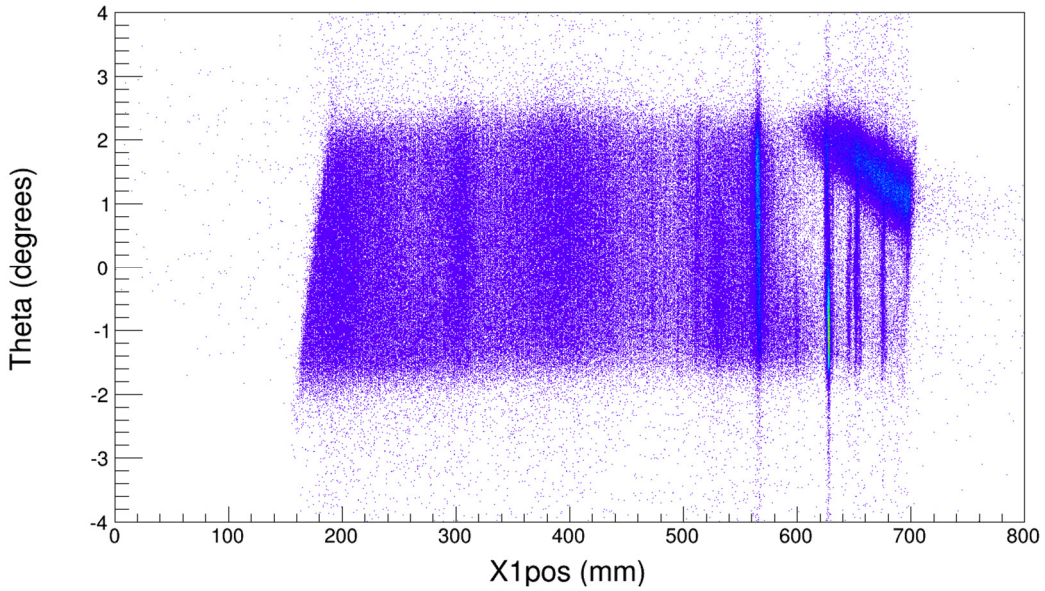

Figure 5.29: K600 scattering angle vs. focal plane position spectrum of ^{12}C. The measurements were taken with a 200-MeV α beam with the spectrometer at $\theta_{lab} = 4°$.

The Hoyle state is located at ~625 mm. The broad background at 600-700 mm and 0°-2° was due to α scattering from protons present in water vapour that was unintentionally on the target. All states appear in the spectrum as vertical lines.

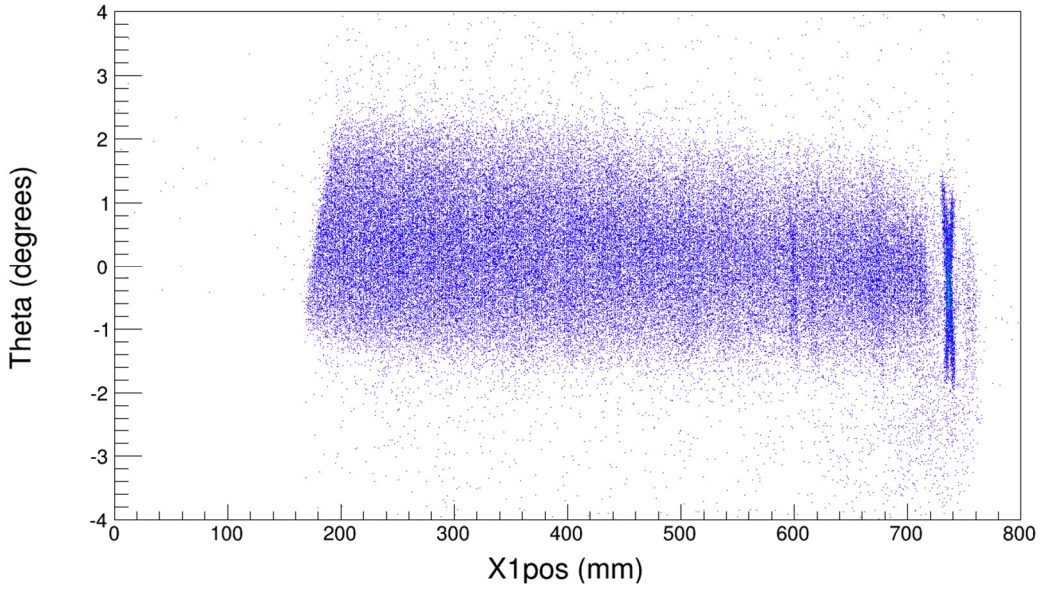

Figure 5.30: K600 scattering angle vs. focal plane position spectrum of the ^{20}Ne(α,α')^{20}Ne* reaction using the extended gas cell. The measurements were taken with a 200-MeV α beam with the spectrometer at $\theta_{lab} = 0°$.

In contrast, Figure 5.30 shows a state located at ~740 mm corresponding to an element in the two foils of the gas cell, crossing each other. This is due to the extended gas cell. Figure 5.31 shows the gated spectrum that reveals another defect which is a direct result of the gas cell as well. Each peak is broadened since the interaction point of the beam can occur at any point along the beam axis within the gas cell.

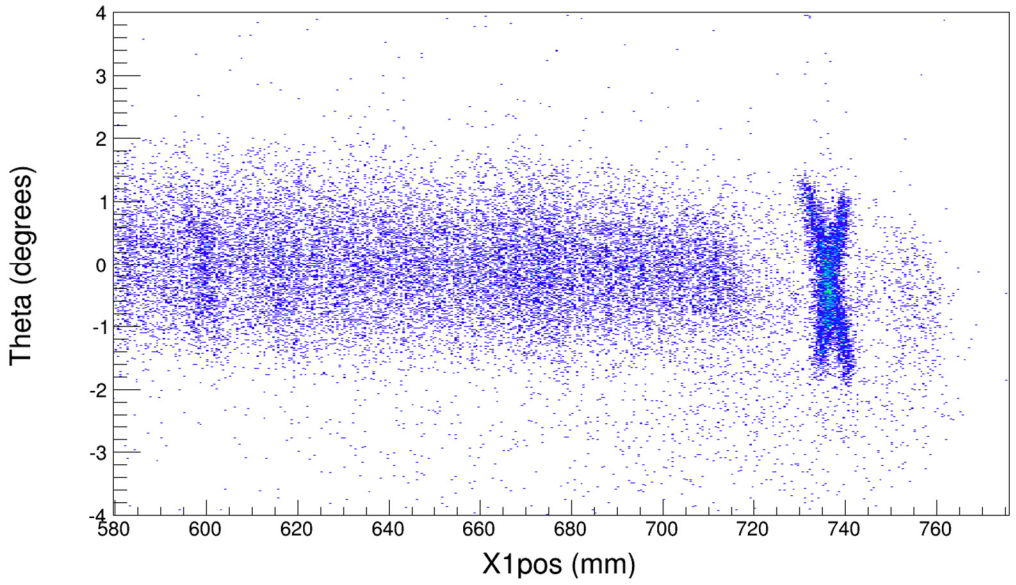

Figure 5.31: Gated scattering angle vs. focal plane position spectrum of the ^{20}Ne(α,α')^{20}Ne* reaction using the extended gas cell.

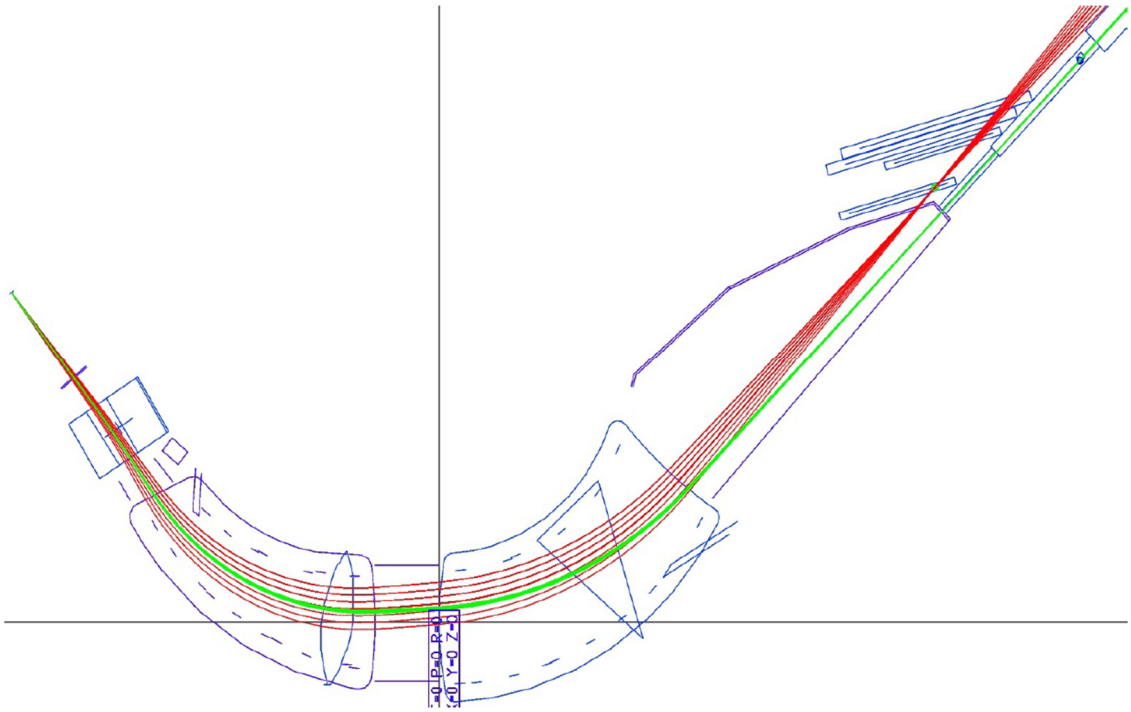

Figure 5.32: TRACK 8.6 simulation of a 0° (p,p') reaction in the K600 magnetic spectrometer [75].

The primary cause of this effect relates to the focal point of the scattered particles. A typical TRACK 8.6 simulation is shown in Figure 5.32. The beam target is a standard thin film in this illustration. The simulation shows the transport of scattered particles within the spectrometer (see Figure 3.1 for K600 illustration). The triangular K-coil, which has a dipole and quadrupole moment, is responsible for focussing scattered particles at the focal plane [48]. The interaction point of the beam with the target varies in a gas cell since it can be anywhere along the beam path within the gas cell. Figure 5.33 to Figure 5.35 are TRACK 8.6 simulations of the focal point of scattered particles for various target positions [76]. The target position in the simulation was moved 5 cm backward and forward to illustrate the effect that an extended gas cell has on the focal point at the VDC wire planes.

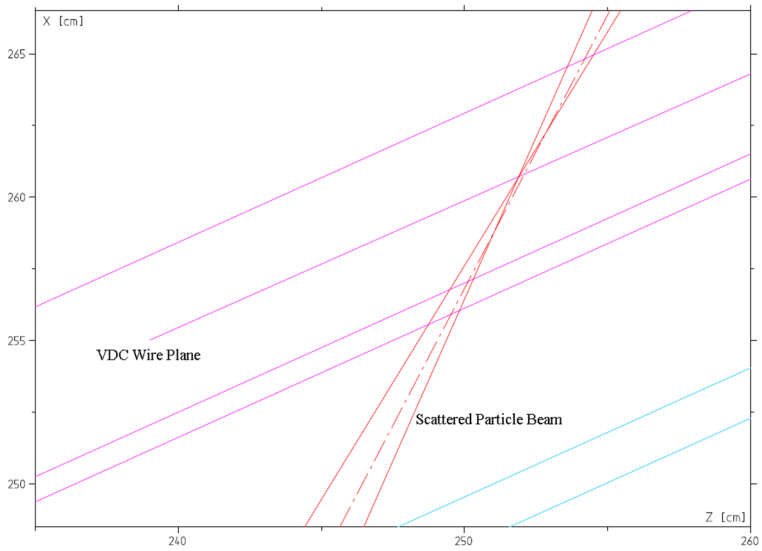

Figure 5.33: TRACK 8.6 simulation of a standard K600 event. The beam target is centred within the scattering chamber so that the focal point is at the VDC wire plane. The wire plane and beam of scattered particles is indicated. The dotted line is a standard reference in TRACK simulations.

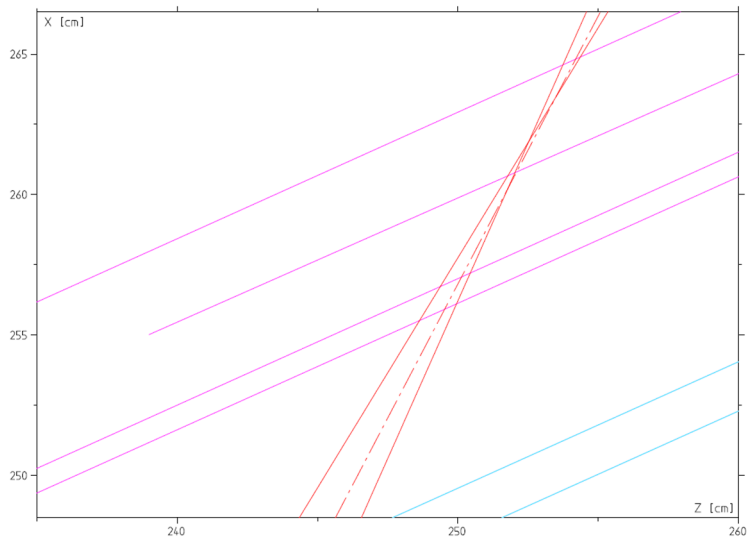

Figure 5.34: TRACK 8.6 simulation of a K600 event with the target shifted 5 cm forward. Moving the beam interaction point forward simply moves the scattered particle focal point forward as well.

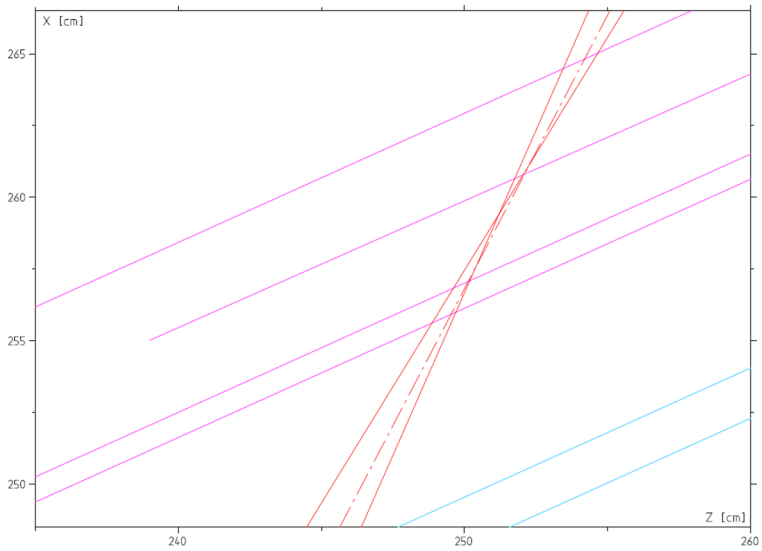

Figure 5.35: TRACK 8.6 simulation of a K600 event with the target shifted 5 cm backward. Moving the beam interaction point backward moves the scattered particle focal point backward.

The relative position of the focal point with regard to the VDC wire planes is the cause of the aberration seen in Figure 5.31. Figure 5.36 and Figure 5.37 explain that the relative focal plane position between X_1 and X_2 is the direct cause of the slanted state in the spectra.

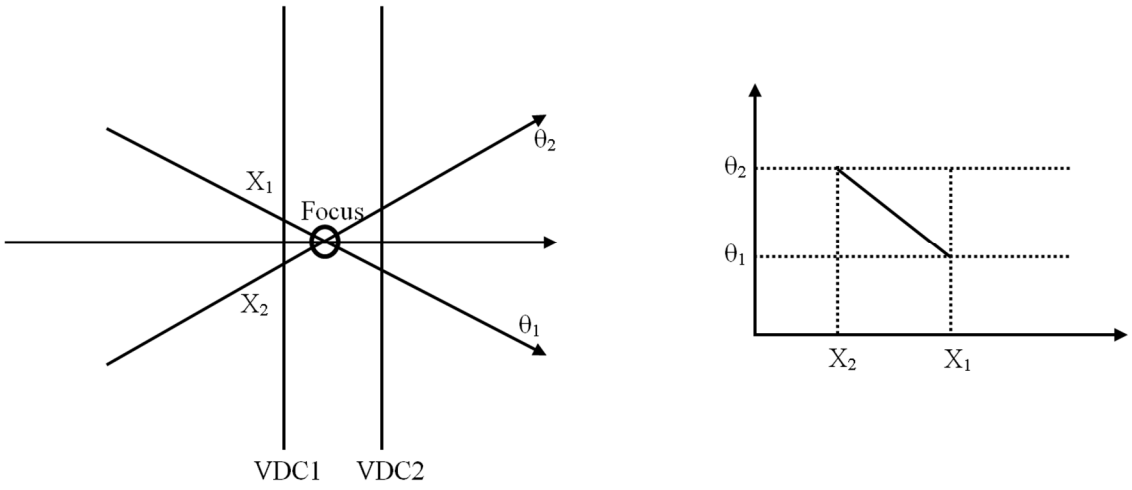

Figure 5.36: Explanation as to the cause of the angled states in the scattering angle vs. focal plane position spectra. The vertical lines represent the wire planes of VDC1 and VDC2. The arrows indicate the beams of scattered particles. The focal plane position is given by X and the angle of the scattered-particle beam is given by θ.The right-hand figure shows that the effect can be recreated if the points (X_1,θ_1) and (X_2,θ_2) are plotted. When the focal point is on either one of the wire planes, then $X_1 = X_2$ and the effect is neutralised.

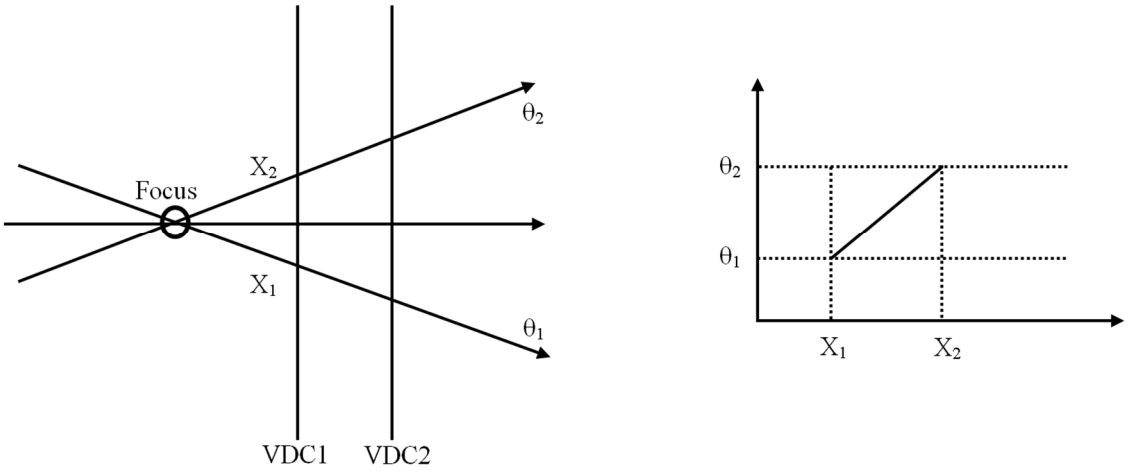

Figure 5.37: Explanation as to the cause of the angled states in the scattering angle vs. focal plane position spectra. If the right-hand figure is combined with the one in Figure 5.36, it will give the cross seen in Figure 5.31.

The impact of an extended gas cell on beam optics can be overcome. GATEAU is capable of full kinematic reconstruction to replicate the track of a decay particle moving through the active region (see Figure 6.6). The tracks can be used to locate the nuclear interaction point by extrapolating the reconstructed particle track to intersect with the beam axis running through the detector. This can in turn be used to correct the aberrations in beam optics to recover energy resolution that is lost as a result of the extended gas cell.

Chapter 6
GATEAU Tests

"If your experiment needs statistics,
you ought to have done a better experiment."

Ernest Rutherford

The definitive part of any detector development is testing. A full, standalone test was conducted after each component of the detector system had been tested separately. Standalone tests presented a data acquisition challenge because the GATEAU system does not have an inherent data trigger. This chapter will discuss the experimental setup used for the standalone test and the results thereof. Additionally, the future in-beam test and motivation thereof will be discussed along with possible experiments for which GATEAU, in coincidence with the K600 magnetic spectrometer, is well-suited.

6.1 Standalone GATEAU Test

GATEAU is a unique active-target detection system in that it is a wire-chamber detector. As discussed previously, the predominant method of detection in active-target systems have been by way of residual energy measurements using DSSSDs, GEMs and CsI detectors that are not suited for particle tracking. The idea for the unique active-target wire-chamber PCB stems from the design of the K600 VDC detectors. This presents a known starting point for the standalone tests in that the parameters of the VDCs, such as detection gas and detector bias, can be applied to GATEAU. The standard VDC detection medium of 90% Ar quenched with 10% CO_2 was used. The readout electronics that were used is identical to that of the VDC electronics. The guard wires had an applied potential of -500 V with the detector cathode at -8 kV.

6.1.1 Experimental Setup

Figure 6.1 illustrates the experimental setup for the standalone GATEAU test (not to scale), along with a representation of the nuclear instrumentation modules (NIMs) used to build a trigger-or system (see section 6.1.2).

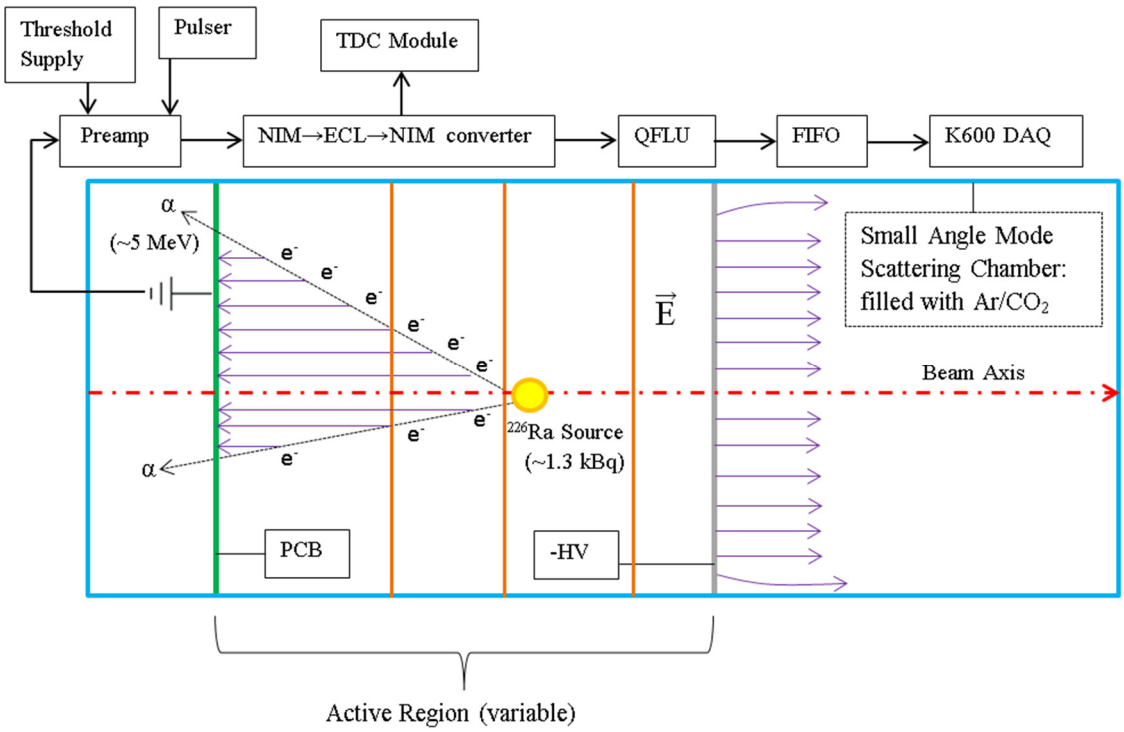

Figure 6.1: Illustration of the experimental setup used to test GATEAU. A ^{226}Ra source was used as an α emitter. The active region is defined as the volume of Ar/CO_2 gas within the confines of the field cage, high-voltage cathode and PCB anode. A diagram of the modules used to build a trigger is included (see section 6.1.2).

The illustration shows the active region that is established between the PCB and high-voltage (HV) cathode within the scattering chamber. The cathode is a single piece of stainless steel manufactured to mirror the exact shape of the PCB wire sections. The detector field cage is represented by the vertical orange lines. Three, 100-µm thick copper wires were used to encircle the active region. The wires were connected in series to each other and the cathode via 1 GΩ resistors. The last wire was connected to a scattering chamber BNC feedthrough and terminated. The field cage improves the homogeneity of the electric field at the boundary of the active region.

For the purpose of the standalone test, a ^{226}Ra α-particle emitter (4.78 MeV, $T_{½}$ = 1600 years) was used. The ^{222}Rn (5.49 MeV, $T_{½}$ = 3.8 days) and ^{218}Po (6.00 MeV, $T_{½}$ = 3.05 minutes) daughters in the decay chain are also α-particle emitters [1]. The radioactive source was one of the limitations of the standalone test. The low-energy threshold cannot be tested since there are no natural ~500 keV α-particle sources. A photo of the complete experimental setup for the standalone test is shown in Figure 6.2.

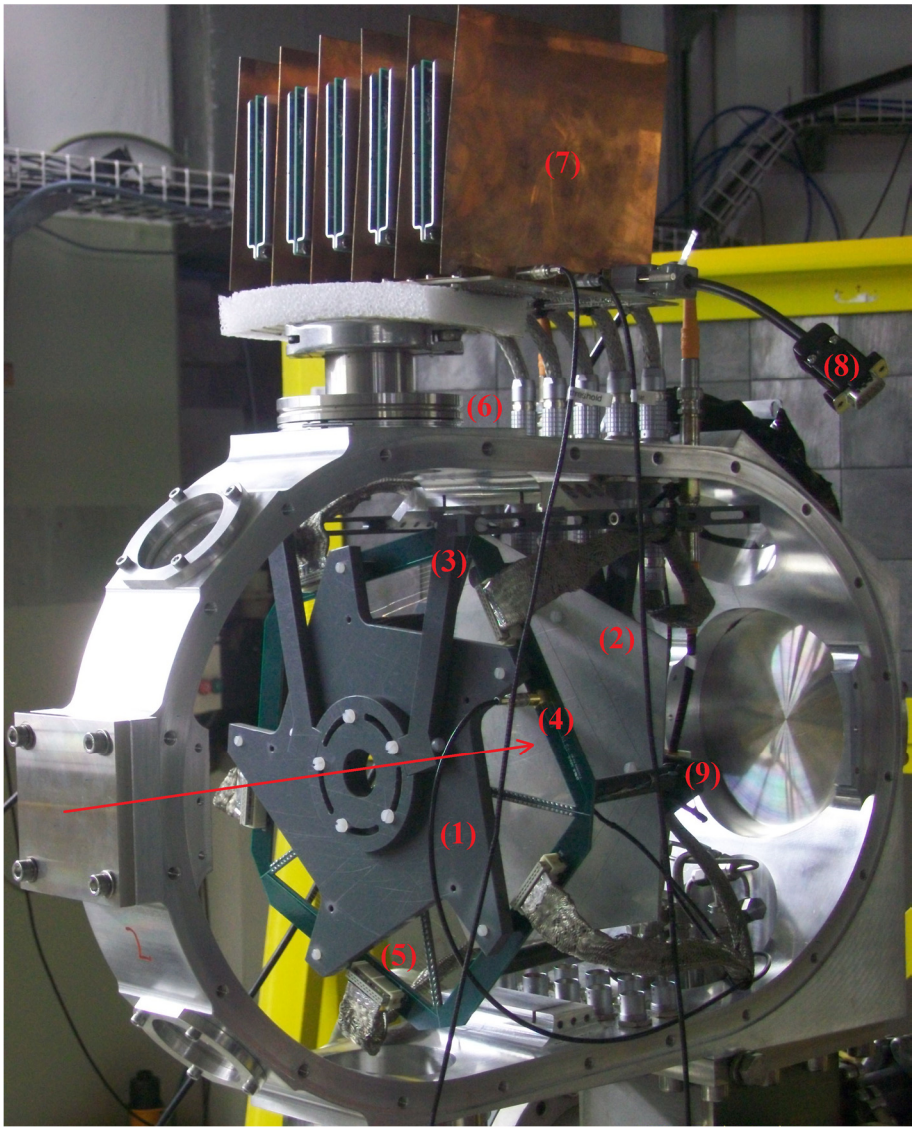

Figure 6.2: Experimental GATEAU setup for the standalone test. The PCB (1) and cathode (2) are mounted on PVC brackets that are connected to the railings (3). The BNC Lemo connector (4) supplies the PCB with power. The 19-pin Lemo female (5) and 19-pin Lemo male (6) cables connect the PCB to the preamplifier (7). The 9-pin serial connector (8) supplies power to the preamplifier. PVC pillars (9) were used to mount the field-cage wires. The beam direction is indicated by the red arrow.

6.1.2 Experimental Method

The PCB guard wires had a potential of -500 V supplied by a Mesytec high voltage power supply that can monitor leakage currents in the order of nano-Ampere. The cathode had a potential of up to -8 kV, supplied by a FUG power supply that monitors leakage currents in the order of µ-Ampere. Monitoring the leakage currents indicated whether the components were electrically discharging or whether the electric fields were being maintained. The active region was varied throughout the test by moving the wire plane closer to the cathode. The field cage was removed entirely in order to replicate the VDC electric field of ~0.5 MV/m by spacing the PCB 1.6 cm from the cathode. No arcing between the PCB and cathode occurred.

The detection gas used during the test had a composition of 90% Ar to 10% CO_2 with a purity of 99.995%, where CO_2 is used as the quenching agent [48]. The spectrometer gas supply system was removed from the VDCs and attached to the scattering chamber. The pressurised cylinder forces gas through the series of polyurethane pipes into the chamber, which is initially evacuated at a pressure of ~10^{-6} mbar. The gas was circulated through the chamber during the test to prevent build-up of gaseous impurities. This was done by opening the vent valve of the chamber as gas was flowing in.

The gas supply contains trace amounts of various atmospheric gas species: O_2 (< 5 ppm), H_2O (< 5 ppm), N_2 (< 20 ppm) and other simple hydrocarbons (< 1 ppm) [48]. Build-up of gaseous impurities within the chamber will cause the electron drift and avalanching processes to break down. Oxygen contamination was the primary concern since it is highly electronegative and consequently restricts electron drift. The solution was to use the Hydrosorb and Oxisorb filters in the spectrometer gas line that remove water vapour and oxygen, respectively. It is known from problems experienced with the VDCs in the past that this type of contamination, which is usually introduced by air leaks, causes the detector efficiency to drop and eventually makes it non-operational. According to [21], if the gas volume is polluted to the point where the composition contains 1% air, 33% of the drift electrons are lost for 1 cm drift distance due to the presence of electronegative elements such as O_2 and H_2O.

The small-angle mode scattering chamber has a number of Lemo feedthrough connectors and various other features making it very versatile (see section 3.2). However, scratches to the aluminium surface and the feedthroughs resulted in various chamber leaks limiting detector functionality. The chamber pressure was improved from ~2×10^{-4} mbar to ~3.8×10^{-6} mbar which helped improve the detector functionality.

The nuclear instrumentation modules (NIMs) used to build the trigger are illustrated in Figure 6.1 and in Figure 6.3. The system uses “or-logic” since any signal wire can trigger the system. It was necessary to assemble this system as GATEAU does not have a trigger to signal the K600 data acquisition system (DAQ) to take data. The detector preamplifiers were connected to four NIM-to-ECL-to-NIM converters through 34-pin ribbon cable connectors. NIM signals are defined as having a digital representation of “1” when the signal voltage is between -0.8 V and -1.0 V. If the signal voltage is exactly zero the digital representation of the NIM signal is “0” [50]. Emitter-Coupled Logic signals are defined by the value of the signal current where signals are represented by the voltage and current: ECL ≡ (V, I) [50].

The converters were needed for two purposes. They were used to split the input signal into two and to convert the NIM signal from the preamplifier into an Emitter-Coupled Logic (ECL) signal for the logic units. The ECL output signal (via Lemo BNC cables) was used to trigger the DAQ and the NIM output signals were used to supply the time-to-digital converter (TDC) modules. The K600 TDC that was used had a 100 ps time resolution with a clock pulse of 40 MHz. A TDC is used to give a digital

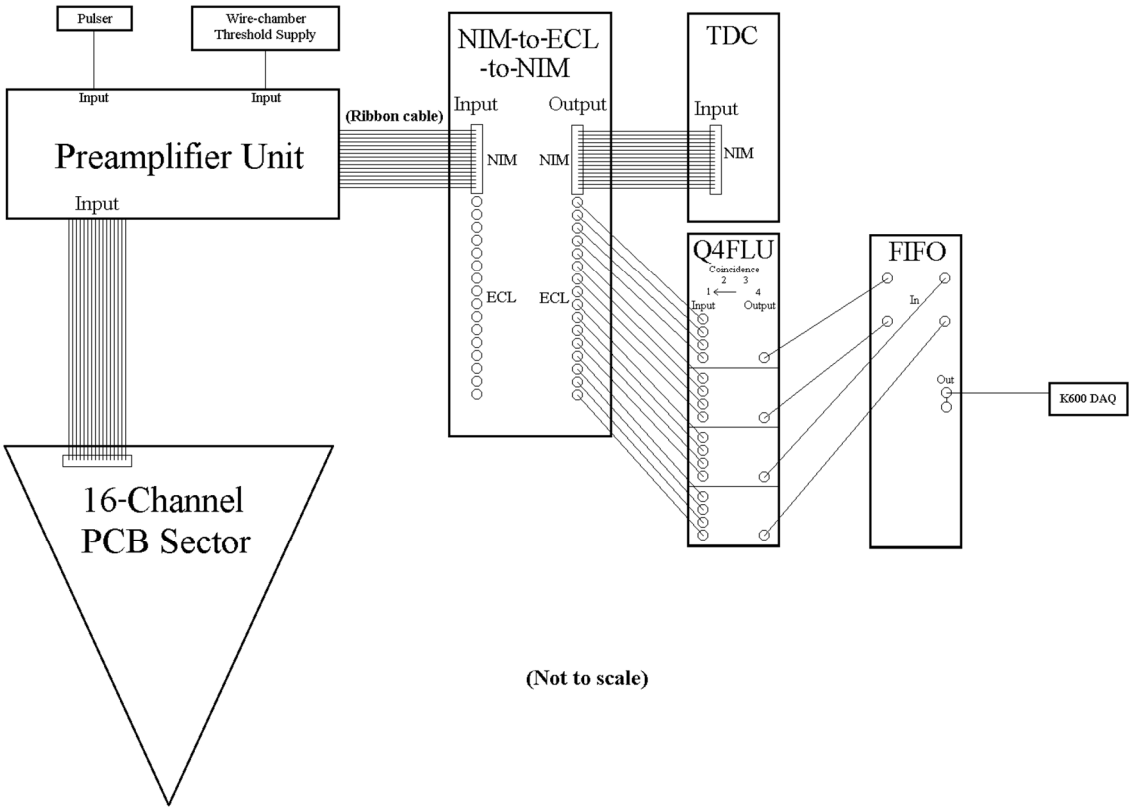

Figure 6.3: Trigger-or system for the GATEAU standalone test. The diagram shows the scheme for triggering on one PCB sector. The full system had four NIM-to-ECL-to-NIM converters. Four four-fold logic units (4FLU) and two quad four-fold logic units (Q4FLU) were used. Two Fan-In Fan-Out (FIFO) modules were used to group the signals and provide a single data trigger. The trigger could only test four PCB sectors at once since there were only four converters available.

record of the relative timing between events in a given coincidence window. It is also capable of giving the absolute time reference of a particular coincidence window.

The ECL signals from the converters were connected to the 4FLUs and Q4FLUs by Lemo BNC cables. The logic units are all set for singles which allows the trigger-or system to signal the DAQ if an electron avalanche occurs on any one of the eighty signal wires on the PCB. The signals from the logic units are grouped by the FIFOs to have a single cable as the DAQ trigger. This is problematic since the sector where the track is detected is possibly not the sector of the triggered wire. The limitations of the trigger-or system are numerous and justify the need for an in-beam test. When using the trigger-or there is also no absolute time reference when analysing the signals from standalone tests since it is used to trigger the DAQ while supplying the TDC with data. This can be seen in Figure 6.4 and Figure 6.5.

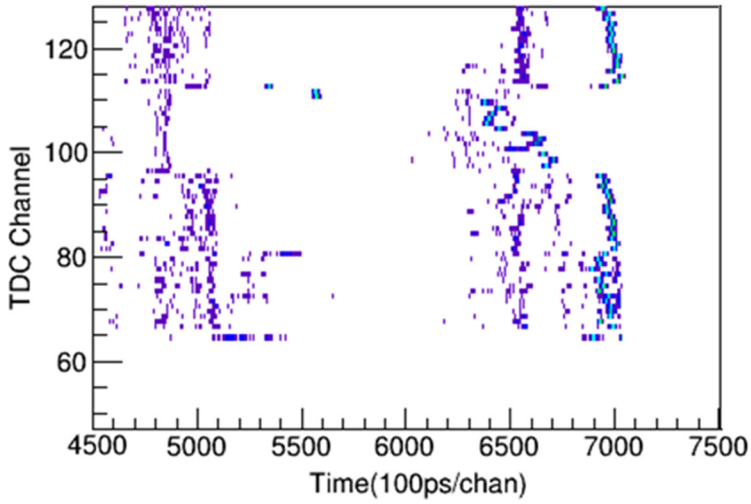

Figure 6.4: TDC spectrum of a noisy, pulser data run. The pulse wave had a rise time of 500 ns.

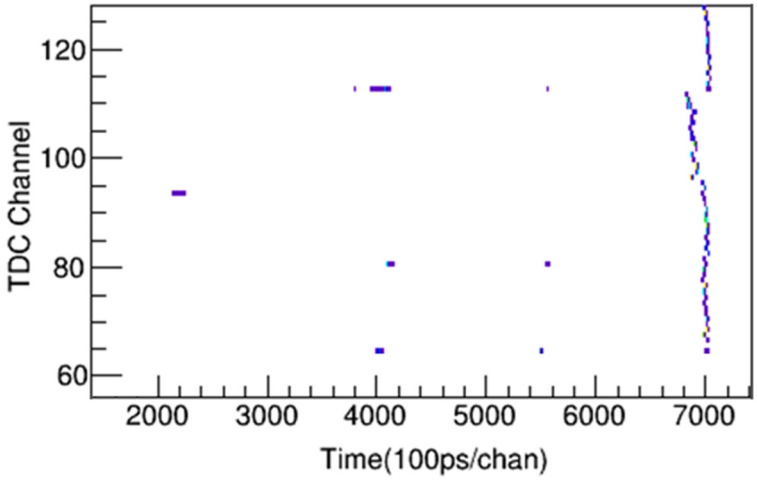

Figure 6.5: TDC spectrum of a pulser data run. The pulse wave had a rise time of 125 ns.

The time reference in both TDC spectra for the two pulser runs differ from each other. The excessive amount of events in Figure 6.4 was a consequence of electronic ringing and the effect was neutralised when the rise time of the pulser was shortened from 500 ns to 125 ns (ringing explained in section 4.1). Regardless, GATEAU was still able to detect various particle tracks.

6.1.3 Standalone Test Results

The standalone test was successful in reconstructing α-particle tracks, as shown in Figure 6.6. The experiment was run with the chamber at ~1 bar. The PCB had a potential of -500 V and the cathode had a potential of -8 kV. The wire-chamber threshold supply was set to a value of 60% with the ^{226}Ra source being used.

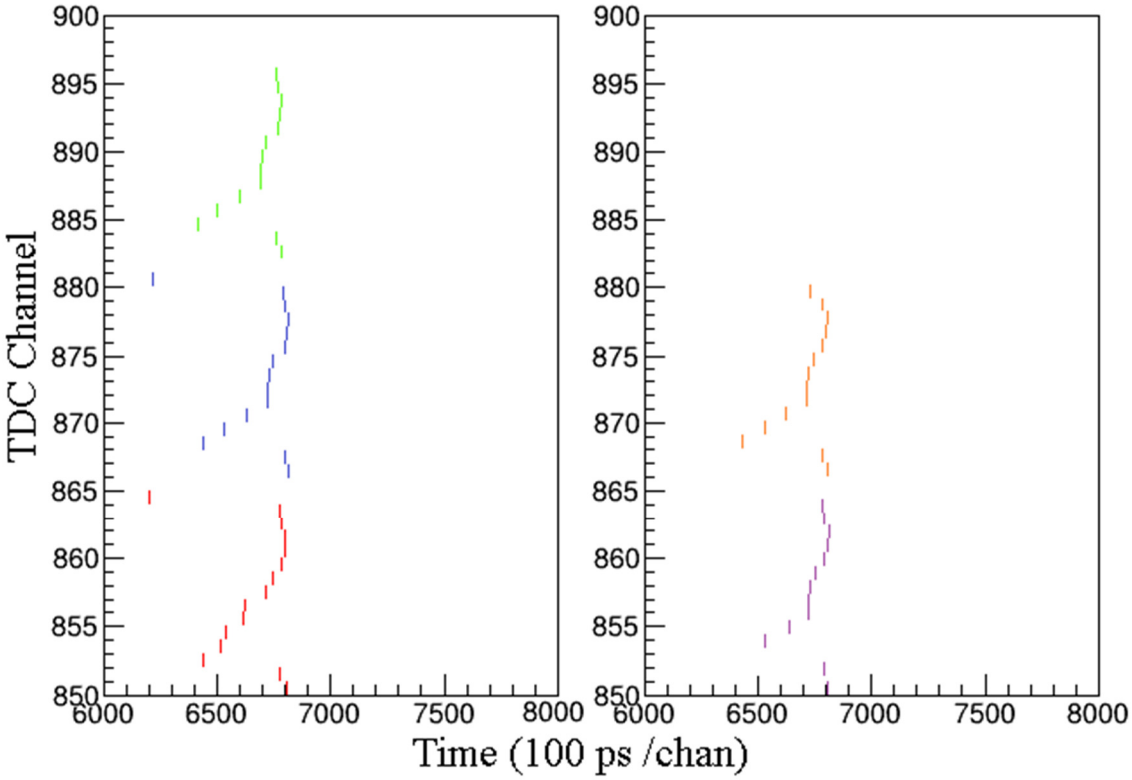

Figure 6.6: α-particle tracks as detected by GATEAU. The standalone detector test concluded with data tracks being reconstructed from the TDC spectra. Arbitrary events were selected from different sectors on the detector PCB. A consistent pattern is evident from the particle tracks. Each colour corresponds to a different PCB sector.

Each set of sixteen TDC channel numbers correspond to different PCB sectors and contain information regarding the azimuthal and polar angle of the particle track (θ and φ in Figure 6.7). The number of signal wires that were triggered gives the polar angle (defined in Figure 6.7 for explanatory purposes). GATEAU has limited azimuthal angular resolution as shown Figure 6.8. Some of the TDC channels for tracks in Figure 6.6 are the same because not all sectors could be tested at once due to the limited number of NIM-to-ECL-to-NIM converters. A standard particle track will have its drift electrons detected in succession, one after the other. The results show that deviations exist, specifically for the first and last few signals of each track. This is the effect that an inhomogeneous electric field has upon the results. The field cage was not in use for the run since the PCB was 1.6 cm from the cathode in order to replicate the VDC drift field of ~0.5 MV/m.

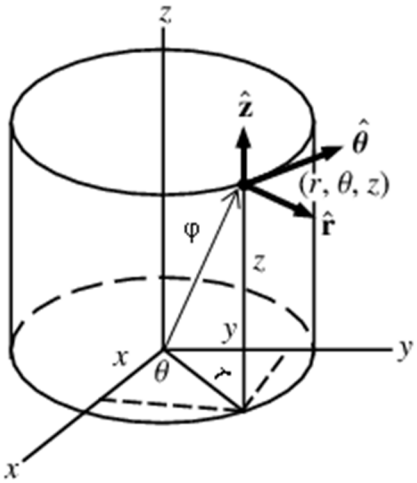

Figure 6.7: Representation of cylindrical coordinates [77] with the polar angle having been added. The azimuthal angle is defined as θ, which is the angle in the xy-plane from the x-axis. The polar angle is defined as φ, the angle from the positive z-axis.

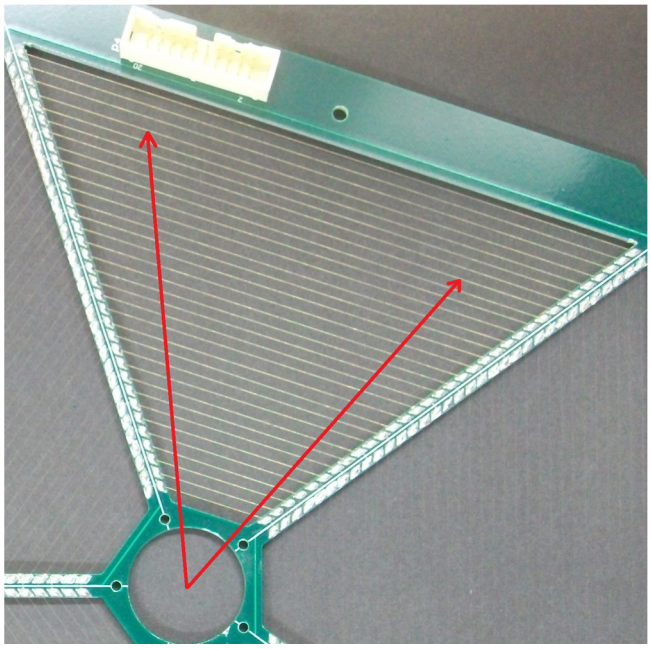

Figure 6.8: One sector detecting two different particle tracks. If a PCB sector hypothetically detects two different particle tracks it would not be able to distinguish between the azimuthal angle of the two events. GATEAU can only distinguish between the polar angle of the events given that they would trigger a different number of signal wires.

The standalone test was unable to determine the low-energy detection limits of GATEAU. The test also lacked a suitable data trigger. It was not possible to see how GATEAU reacts to a large amount of ionising radiation that an in-beam run characteristically would produce. Various experimental limitations were encountered during the standalone test given that the detector is specifically built for in-beam coincidence measurements. As a result, one experimental test weekend was proposed to the iThemba LABS programme advisory committee (PAC). The proposal was accepted and the experiment is scheduled for the weekend of 11-14 December 2015.

6.2 Outlook: In-Beam GATEAU Test

The in-beam test will have GATEAU used as an ancillary detector with the K600 spectrometer for the first time. It has been proposed that the detector will be tested in two different phases: the time projection principle will be tested first and a natural progression towards the active-target principle will follow. To test the TPC principle, a solid ^{12}C target mounted on a modified, non-metallic target ladder will be used. The gas will be used as the detection medium in this case. Since a solid target implies a single locus, all decay particle tracks must converge to the in-beam position of the ^{12}C target when reconstructed. Afterward, the target will be moved out of the active region so that the beam may interact exclusively with the gas to test the active-target principle.

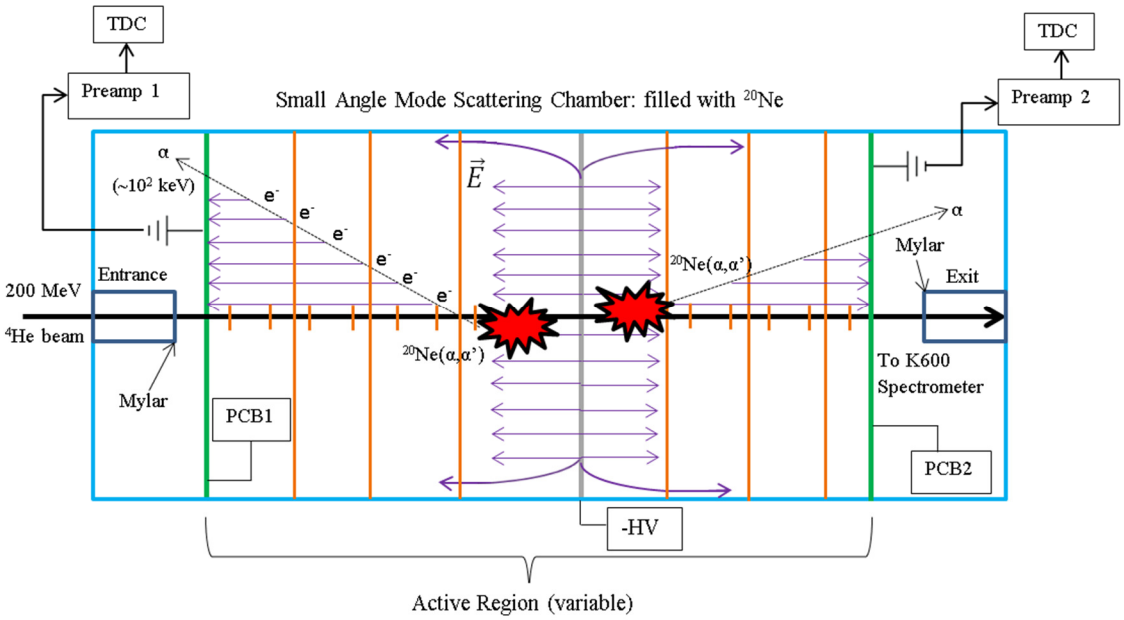

Figure 6.9: GATEAU setup for in-beam experiments. Two PCB anodes will be used to maximise detection efficiency. An additional inner field cage will be developed to prevent ionising radiation, incident with the α beam, from overwhelming inner PCB signal wires. Mylar entrance and exit windows will be mounted within the chamber. The preamplifiers will connect directly to the TDC modules.

In order to improve detection efficiency, two detector PCBs will be used to maximise the active region within the scattering chamber. The experimental setup that will be used is shown in Figure 6.9 (not to scale). The Mylar windows will be mounted on modified guard-vacuum cells that connect to the upstream and downstream chamber entrances (see section 6.2.1). The gas target for the in-beam test would have been CO_2. However, it is generally used as a quenching agent in gas detectors. This may inhibit GATEAU from functioning properly by limiting electron drift and avalanching within the active region. It was decided that 90% natural neon quenched with 10% CO_2 will be used.

Furthermore, the candidate 4α state in ^{16}O is only 660 keV above the break-up threshold of 14.437 MeV [72] making it difficult to test the low-energy threshold of GATEAU. The average α-particle energy would be ~165 keV and possibly below the

energy detection threshold. GATEAU would only be able to detect the $^{16}O^* \rightarrow {}^{12}C + \alpha$ decay modes. A similar argument holds for ^{12}C given that the 0_2^+ 3α Hoyle state at 7.65 MeV is near the 7.36 MeV decay threshold [1]. However, using CO_2 as a quenching agent may make it remotely possible to observe the 3α and 4α states given that a few of the nuclear interactions within the gas target may occur with CO_2.

6.2.1 Future Developments

Testing the detector setup revealed limitations of some of the components. Experiment PR231 revealed limitations of the gas cell and the entrance/exit windows. Moreover, the standalone tests showed that an improved field cage is needed for an in-beam run in addition to improving the detector gas purity. Various hardware and software developments are underway in preparation for the in-beam test.

An internal gas cell, such as the one used in PR231, is not suitable for the GATEAU PCBs. The entire scattering chamber will act as a gas cell. New guard-vacuum cells, analogous to those used in PR231, are being developed that can be mounted on the chamber entrance and exit. The cells will be connected to remotely controlled, electronic actuators that can move the foils while the experiment is running. Two actuators are used for each cell to move the foils in a plane. This will spread the radiation damage across a larger area making it possible to run an entire weekend without breaking vacuum. As discussed in section 6.1.2, the gas purity in drift chamber detectors is crucial and maintaining continuous flow of detection/target gas for the entire weekend is a priority.

Gas going into the chamber will be controlled by the pressure regulator and the flow rate controller. The pressure regulator connects to the gas feed and maintains the gas cell pressure at a pre-set value. The flow rate controller maintains the rate at which gas is evacuated from the system. Both components will be controlled remotely.

Many elements of the detector system will be controlled remotely to improve experimental stability and reproducibility which will also limit the amount of wasted beam time. The Experimental Physics and Industrial Control System (EPICS) is a real-time computer I/O interface to enable the remote-control of certain GATEAU elements. Elements being coded into EPICS include the flow rate controller, the pressure regulator, the guard cell actuators and the detector bias (two units for two detector PCBs and one high-voltage unit for the cathode).

The solid targets and ZnS viewer to be used have to be mounted on a target-ladder frame. The viewer is needed for beam optics considerations since it is used to tune the α-beam. A shortened, non-metallic target-ladder frame is being developed. It will be located beneath the detector field cage and needs to retract completely to preserve homogeneity of the electric field. Various high-voltage components in the system require the target ladder to be non-metallic to prevent arcing.

Two additional detector PCBs with 10-µm diameter signal wires and 20-µm diameter guard wires have to be made. As beam time is limited, extra PCBs are needed since they

take a long time to repair if damaged which is highly likely since the 10-µm diameter signal wires are extremely fragile. Furthermore, thinner signal wires imply improved detection capabilities, as discussed in section 5.1. A new high-voltage cathode mesh has to be developed. A solid cathode plate is not suitable since it may inhibit the flight path of decay particles in the active region.

A new inner field cage and improved outer field cage have to be made. It has to be easily modifiable since the need may arise during testing to increase or decrease the active region. PVC equivalents of the PCBs will be used to mount each segment of the field cage. The PVC structures will be connected to the sliding guard rails in the scattering chamber. Finally, software developments, apart from EPICS, will include updating the K600 online analyser to include C code classes for the GATEAU sort code. The primary focus will be to have a preliminary version running for the beam weekend for real-time analyses to plot coincidence spectra.

6.2.2 Beam Time Objectives

There are various unknown effects that in-beam runs may have on GATEAU which is why it has to be tested before running $^{20}Ne(\alpha,\alpha')^{20}Ne^*$. The main objective for the test will be to determine in-beam functionality, i.e. using the new GATEAU sort code to reconstruct decay particle tracks with the spectrometer in coincidence. Elastic scattering from the windows and ^{20}Ne gas is a concern since the scattering products may overwhelm the detector. If this is a limiting factor, the beam current will be adjusted accordingly to faint beam mode which, in turn, will limit the count rate.

The effect that ionising radiation like x-rays, γ-rays and δ-electrons have on the background has to be investigated as well. Electrons that are removed from their atomic orbitals by high-energy, α-beam particles are referred to as δ-electrons. They consequently travel along the beam direction and may overwhelm inner signal wires. This is one of the motivating factors for the inner field cage.

6.2.3 Beam Requirements and Event Rate Estimation

Standard α-beam requirements, relative to the K600, will be used for the test. One weekend of α particles at E_{lab} = 200 MeV will be required which equates to a maximum of 60 hours of beam time. The α-particles will be completely ionised and, therefore, have a charge state of +2. The use of the small-angle mode scattering chamber and the nature of the experiment necessarily imply that the K600 will be at $\theta_{lab} = 0°$, with the standard 49-mm diameter collimator being used. Low halo is required in order to have a relatively clean energy spectrum in terms of background since zero-degree mode will be in operation. A pulse selection of 1 in (3, 4, 5) will be required to minimise constraints on beam operation and have enough time between coincidence events. During experiment PR236 the energy resolution was 70 keV for 4 pnA (also with a 200-MeV beam) which would be ideal for the GATEAU in-beam test. Faint beam mode will initially be used to determine preliminary detector functionality. The beam current will

be increased gradually up to a maximum of 2 pnA to evaluate where GATEAU becomes saturated.

Rate estimation:

The typical yield that can be expected in the K600 focal plane is given by:

$$Y = N\, I\, \Delta\Omega \frac{d\sigma}{d\Omega} \eta. \tag{9}$$

The total yield is given by Y with the integrated current given by I. The yield per second, y, can be determined if the current is given in particles per second. In this instance: I = 1 nA (~$6x10^9$ pps). The K600 VDC efficiency is high and conservatively estimated to be η ~80% (typical efficiencies during experiments range from 85%-95%). The solid angle is $\Delta\Omega$ = 3.48 msr. This is fixed for the spectrometer at 0° with the standard 49-mm diameter collimator 735.5 mm away from the target plane.

The differential cross section normally has a range of $d\sigma/d\Omega$ ~10-1000 µb/sr. A conservative cross section of ~100 µb/sr is assumed which is typical in the case of inelastic scattering. The effective gas-target thickness will affect the count rate as well. The number of target atoms per cm^2, N, is calculated by a modified version of the ideal gas law. From $PV = Nk_BT$, it follows that:

$$\frac{N_B}{V} d = \frac{P}{k_B T} d \equiv \nu, \tag{10}$$

where d is the beam path length through the gas cell which is equal to 20 cm. The areal density (in particles per unit area) is defined as ν which is equal to N in equation 9. The variable for the number of atoms in the Boltzmann equation is symbolised by N_B. A complete definition of the variables is given in Appendix A. The effective target thickness μ is given by:

$$\mu = \upsilon m, \tag{11}$$

with m the mass of the ^{20}Ne nucleus in kilogram. The mass of a single nucleon is ~$1.67x10^{-27}$ kg. The areal density of a ^{20}Ne target at 20 mbar was determined to be: $\nu(^{20}Ne) = 2.62x10^{23}$ m^{-2}. This results in an effective target thickness of $\mu(^{20}Ne)$ = 0.875 mg/cm^2. Using the areal density the count rate (per nuclear state) in the K600 focal plane was determined:

$$y \approx 0.017 \text{ counts/s} = 61 \text{ counts/h}.$$

The calculation was performed assuming that the gas cell will only contain neon gas at a constant pressure and temperature.

6.2.4 SRIM Simulations

The SRIM (Stopping Range In Matter) program [78, 79] was used to simulate the straggling effect when impinging an α-beam into the gas cell. The target definition used in SRIM had one 1-µm thick Mylar foil at the beam entrance and one at the beam exit. A gas mixture of 90% natural neon and 10% CO_2 was defined between the two foils. The beam path length through the cell for the simulation was taken to be 25 cm which is the approximate path length that will be used for the in-beam test.

Roughly five millions events were simulated over a period of three days. The predominant form of beam energy loss through the gas cell will be as a result of ionisation. Simulations showed that 99.96% of energy loss is due to ionisation. Recoil reactions and lattice vibrations in the form of phonons were the additional forms of energy loss. Each contributed 0.02% to the energy loss. The results show that there will be a significant amount of straggling. This divergence of the initial focussed beam occurs due to continuous Coulomb scattering and collisions by the α-particles as they move through the gas. However, the collimator will stop any of these beam particles from entering the spectrometer. Figure 6.10 shows the straggling effect with Figure 6.11 showing the transverse view. The simulation has a relatively high degree of accuracy as suggested by Figure 6.12.

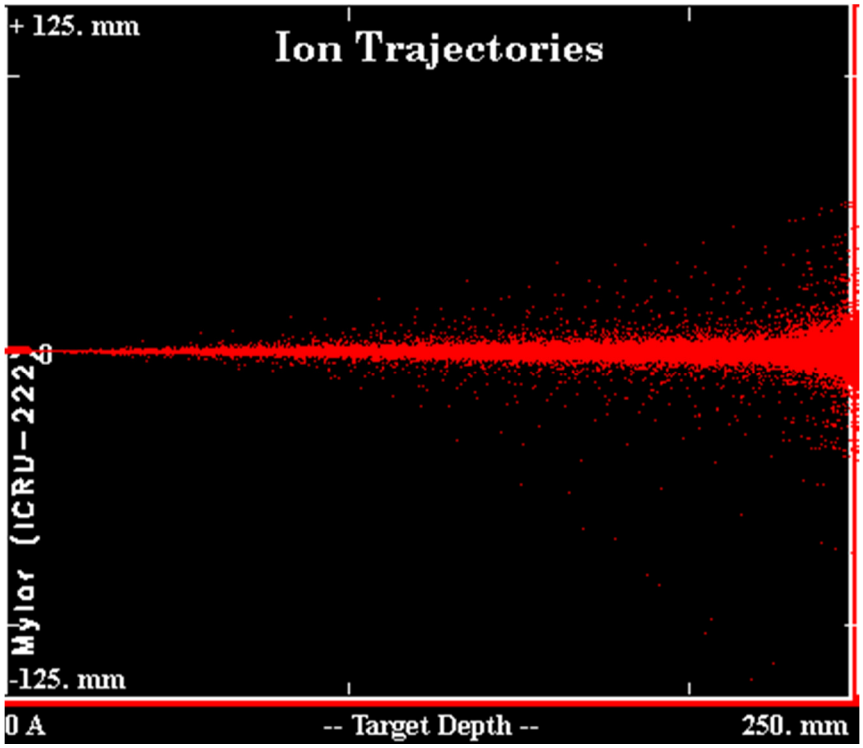

Figure 6.10: SRIM simulation of the in-beam gas cell. A 200-MeV α beam was used. The entrance and exit windows are defined as 1-µm thick Mylar foils, rather than defining two 0.5-µm thick foils, since it does not alter the results of the simulation in any way.

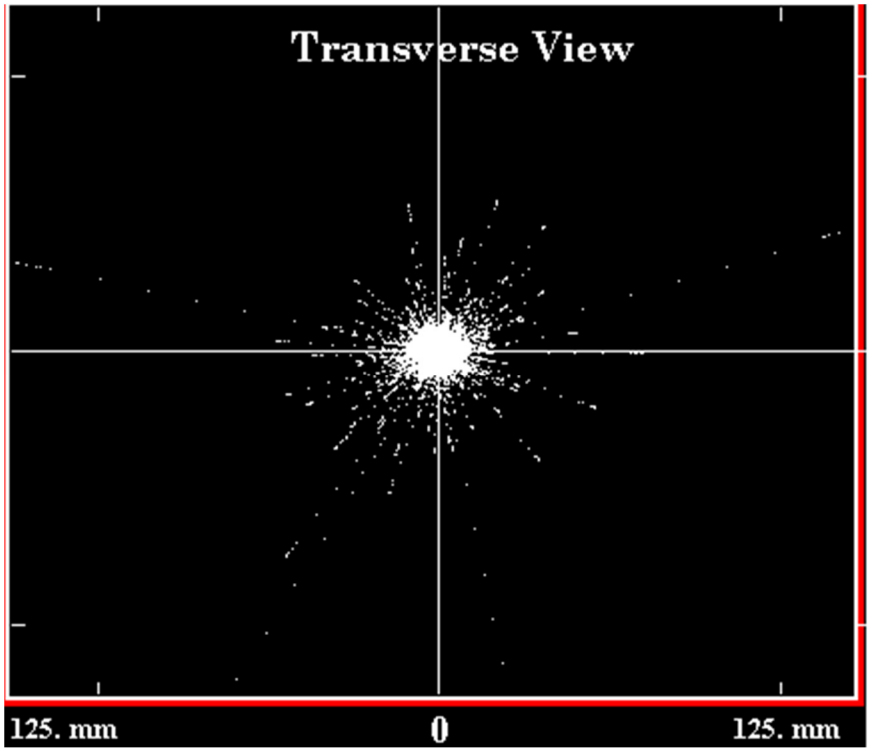

Figure 6.11: SRIM simulation of the in-beam gas cell. A 200-MeV α beam was used. The target definition is the same as in Figure 6.10. The figure shows the transverse view of the beam straggling through the gas cell. The central beam spot shows that most of the events undergo minimal straggling.

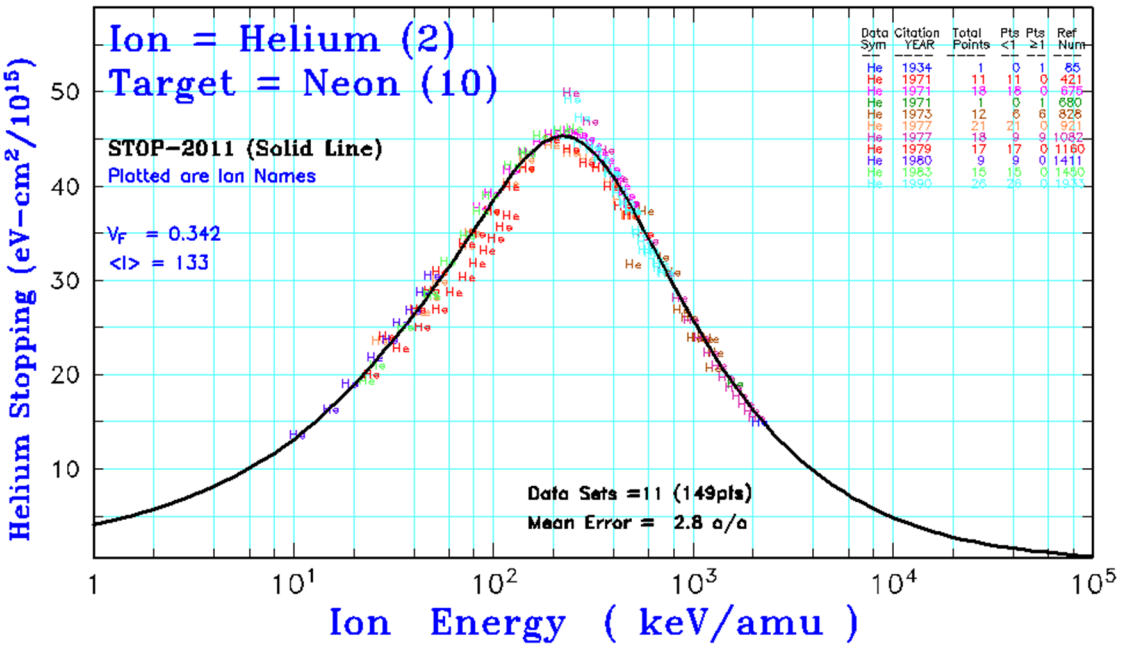

Figure 6.12: Beam stopping power versus ion energy in a neon target. Each He point within the plot is the literature value for that specific ion energy. The Gaussian curve is fitted to experimental observations and represents the stopping power values that SRIM uses to execute its simulations.

6.2.5 Potential Experiments with GATEAU

A significant amount of resources have been invested into the GATEAU detector development. The intention is to use the detector for other studies apart from $^{20}Ne(\alpha,\alpha')^{20}Ne^*$ should in-beam tests prove to be successful. Combining GATEAU with the K600 magnetic spectrometer will result in a detection system that is capable of high-energy resolution measurements with a low-energy and low cross section threshold for decay particles from recoil nuclei. This combination will allow the study of various nuclides from solid and gaseous targets at 0° with (p,p') and (α,α') reactions. Nuclides that can be studied include, but are not limited to, $^{12,14}C$, $^{16,17,18}O$, $^{20,21,22}Ne$ and ^{36}Ar. The PR231 recycling assembly will be used for expensive and exotic gaseous targets like ^{21}Ne and ^{36}Ar. The ^{22}Ne (9.25% natural abundance) gas used in [10] was bought for ~R10000/L. High purity ^{21}Ne and ^{36}Ar, with a natural abundance of 0.27% and 0.337% respectively, will therefore be very expensive to use [80].

GATEAU can also be used in the study of astrophysically important resonances. The $^{15}O(\alpha,\gamma)^{19}Ne^*$ reaction can be studied indirectly through the $^{21}Ne(p,t)^{19}Ne^*$ reaction since $^{19}Ne^*$ decays via the emission of low-energy α particles with $E_\alpha \sim 10^2$ keV. The typical cross section is also expected to be low. The detector may also be used in thick-target mode to look at various resonant states. As the target is impinged upon, the beam energy will degrade and various states are populated as a function of beam energy. The gas would typically be at 1 atmosphere which implies a larger drift field. The gas cell windows would have to be revised should such an experiment come to fruition.

The Coincidence Array for K600 Experiments (CAKE) is a silicon detector array that consists of five, 400-μm thick MMM-type double sided silicon strip detectors (DSSSDs). The actual setup within the small-angle mode scattering chamber is shown in Figure 6.13. Four detectors were used during this particular experiment. Another potential prospect is the combination of CAKE together with GATEAU as ancillary units for the K600. A CAD drawing of this potential setup is shown in Figure 6.14. The pentagonal GATEAU PCB design was chosen so that CAKE and GATEAU could be combined.

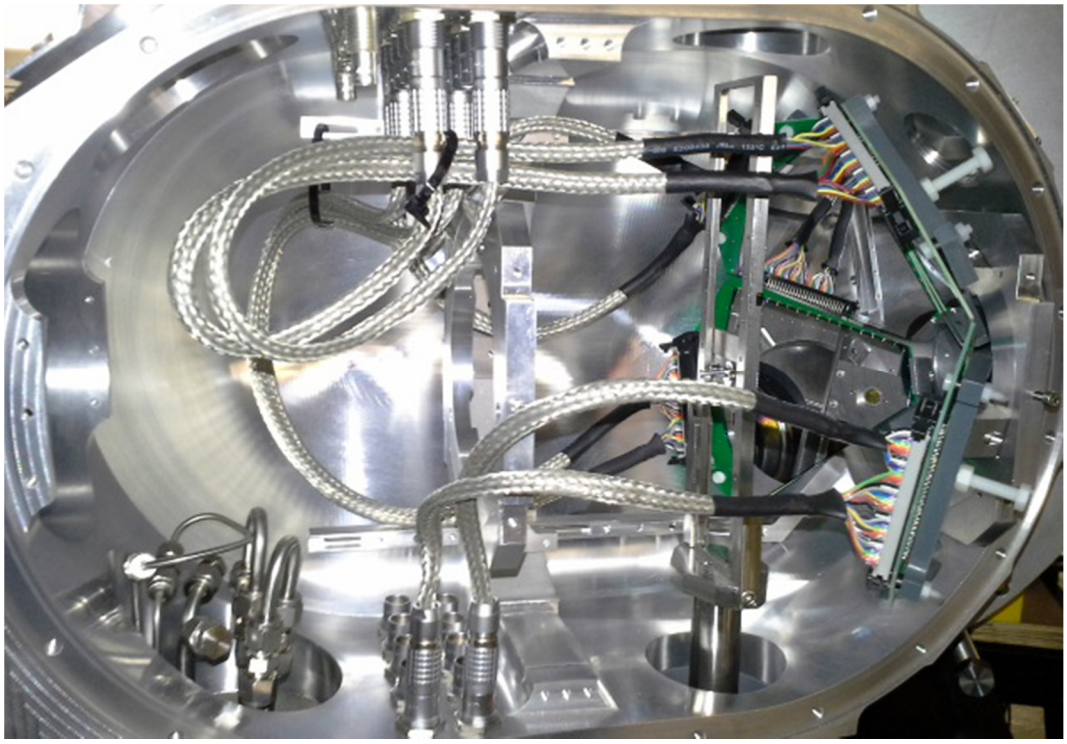

Figure 6.13: CAKE silicon detector setup inside the small-angle mode scattering chamber.

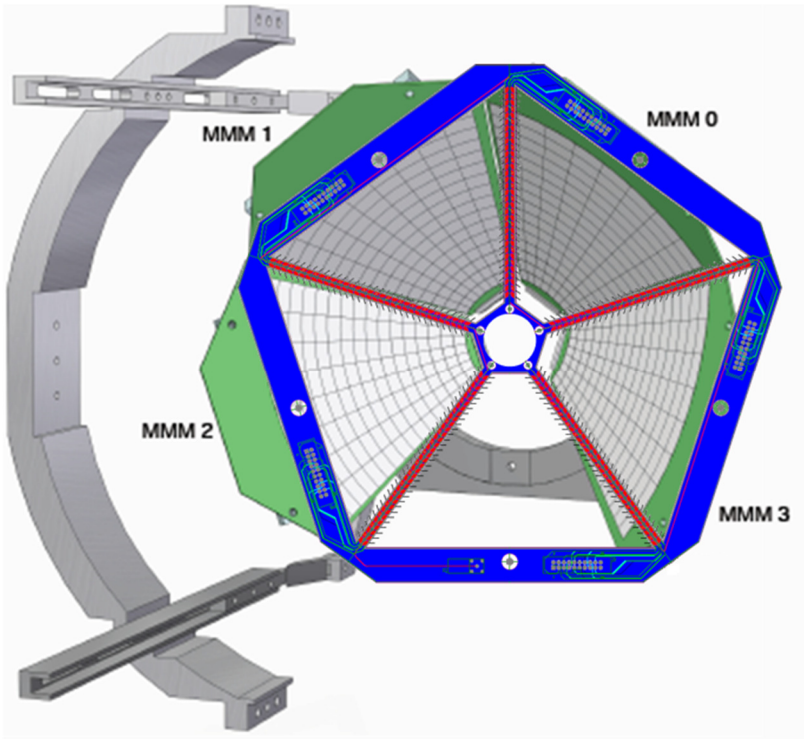

Figure 6.14: Possible combination of the CAKE and GATEAU ancillary detectors. The MMM-type detectors are segmented into sectors (vertical columns) and rings [49]. Decay particles would create drift electrons while they move through the active region. As the PCB wires are passed, the particles would go on to hit the silicon detector array. The nuclear interaction point can be reconstructed with GATEAU and fed into data from the CAKE array to compensate for energy loss through the gas. This is potentially a powerful detection method.

Conclusion

"If I have seen a little further it is by standing on the shoulders of giants."

Isaac Newton

Time projection chambers and active-target detectors have been used to address some of the more challenging and interesting experimental observations in nuclear and particle physics. The ability of indirect particle identification and kinematic reconstruction has established these detectors as powerful auxiliary detection units.

An active-target detector was designed, built and successfully tested for the study of the ^{20}Ne(α,α')^{20}Ne* reaction. It will be used to study the Hoyle-like state in ^{20}Ne that was identified as a possible candidate at E_x = 22.5 MeV and $J^{\pi} = 0^+$. The problem was addressed by formulating a hypothetical detector system and testing it by means of simulation. Existing active-target collaborations from various laboratories were investigated in order to be familiarised with problems that these detector systems encounter. The nature of the ^{20}Ne Hoyle analogue and (α,α') reaction were also investigated to determine the detection constraints.

In addition, the study has found that 40-mm diameter Mylar entrance and exit windows do not add to beam halo or interfere with background conditions. A subsequent evaluation on the effect of extended gas cells on beam optics was performed. It has also been found that the gas-target purity plays an important role and ultimately influences detector functionality. This study has also facilitated the development of a low-pressure gas system. Moreover, a multi-layer PCB has been developed successfully along with a specialised way of mounting thin detection wires.

Subsequent standalone tests demonstrated that GATEAU has the ability to retrace α-particle tracks for the purpose of kinematic reconstruction. Future developments will include various hardware and software alterations to establish GATEAU as a functional, in-beam detector system.

Appendix A

The Bethe-Bloch Formula is defined as:

$$-\frac{dE}{dx} = \frac{4\pi e^4 z^2}{m_0 v^2} NB, \tag{7}$$

where

$$B = Z\left[\ln\left(\frac{2m_0 v^2}{I_{av}}\right) - \ln\left(1-\frac{v^2}{c^2}\right) - \frac{v^2}{c^2}\right]. \tag{8}$$

The variables in the Bethe-Bloch formula are defined as follows: the incremental energy loss over an incremental distance is given by dE/dx. The standard unit of charge is given by e with the atomic number of the incident particle given by z. The atomic number of the target is Z. The rest mass of an electron is m_0. The velocity of the incident beam particle is v. The volumetric density of the target is N in atoms/cm^3. The speed of light is symbolised by c and I_{av} is the average ionisation potential of the target. Finally, E is the energy of the incident beam particle.

The areal density equation:

$$\frac{N_B}{V} d = \frac{P}{k_B T} d \equiv \nu, \tag{10}$$

The variable for the number of atoms in the Boltzmann equation is symbolised by N_B. The areal density, in particles per unit area, is symbolised by ν. The beam path length through the gas cell is defined as d, given in cm. The total path length through the gas cell for an in-beam test will be equal to 20 cm. The Boltzmann constant is $k_B = 1.380\text{x}10^{-23}$ J/K. The pressure P is given in Pascal where P = 2000 Pa (pressure in the gas cell during the in-beam test). The temperature is kept relatively constant in the K600 vault at T = 293.15 K. The volume V of the scattering chamber can be determined through analysis of the CAD drawings thereof but it is not needed to calculate the areal density.

Acronyms and Abbreviations

4FLU: 4-Fold Logic Unit
ANASEN: Array for Nuclear Astrophysics and Structure with Exotic Nuclei
CAD: Computer Assisted Design
CAKE: Coincidence Array for K600 Experiments
CPSPC: Central Position-Sensitive Proportional Counter
CsI: Caesium Iodide
DAQ: Data Acquisition System
DSSSD: Double-Sided Silicon-Strip Detector
ECL: Emitter-Coupled Logic
EDF: Energy-density Functional
EM: Electromagnetic
EPICS: Experimental Physics and Industrial Control System
FIFO: Fan-In Fan-Out
GATEAU: Gaseous Active-TargEt Ancillary Unit
GEM: Gas Electron Multiplier
IUCF: Indiana University Cyclotron Facility
keV: kiloelectron Volt
LABS: Laboratory for Accelerator Based Science
MeV: Megaelectron Volt
nA: nano-Ampere
NIM: Nuclear Instrumentation Module
PAC: Programme Advisory Committee
PCB: Printed Circuit Board
PMT: Photomultiplier Tube
pnA: particle nano-Ampere
ppm: parts per million
pps: particles per second
PSSBA: Position-Sensitive Silicon-Barrel Array

Q4FLU: Quad 4-Fold Logic Unit

RBS: Rutherford Backscattering Spectrometry

RGA: Residual Gas Analyser

RIB: Radioactive/Rare Ion Beam

RMS: Root Mean Square

SM: Shell Model

SR: Shockley-Ramo

SRIM: Stopping Range In Matter

SSC: Separated-Sector Cyclotron

TACTIC: TRIUMF Annular Chamber for the Tracking and Identification of Charged particles

TDC: Time-to-Digital Converter

TPC: Time Projection Chamber

VDC: Vertical Drift Chamber

Bibliography

[1] National Nuclear Data Center website, Brookhaven National Laboratory, http://www.nndc.bnl.gov, accessed on 25 July 2015.

[2] C.W. Cook *et al.*, *^{12}B, ^{12}C, and the Red Giants*, Phys. Rev. **107** (1957) 508.

[3] F. Hoyle, *On nuclear reactions occurring in very hot stars. I. The synthesis of elements from carbon to nickel,* Astrophys. J. Suppl. **1** (1954) 121.

[4] E.M. Burbidge, G.R. Burbidge, W.A. Fowler and F. Hoyle, *Synthesis of the Elements in Stars,* Rev. Mod. Phys. **29** (1957) 547.

[5] C. Rolfs and C.A. Barnes, *Radiative Capture Reactions in Nuclear Astrophysics*, Ann. Rev. Nucl. & Part. Sci. **40** (1990) 45-78.

[6] J.A. Weinman, *Techniques for the Study of Radiative Alpha-Capture Reactions,* Nucl. Instr. Meth. **24** (1963) 390-394.

[7] K. Ikeda, N. Takigawa and H. Horiuchi, *The Systematic Structure-Change into the Molecule-like Structures in the Self-Conjugate 4n Nuclei,* Suppl. Prog. Theor. Phys. **02** (1968) 464-475.

[8] Tz. Kokalova, M. Freer, N. Curtis *et al.*, *Yield measurements for resonances above the multi-α threshold in ^{20}Ne,* Phys. Rev. C **87** (2013) 057309.

[9] New Scientist website, www.newscientist.com, accessed on 25 March 2015.

[10] J.A. Swartz, B.A. Brown, P. Papka *et al.*, *Spectroscopy of narrow, high-lying, low-spin states in ^{20}Ne*, Phys. Rev. C **91** (2015) 034317.

[11] J.A. Swartz, *Search for low-spin states above the 5-α break-up threshold in ^{20}Ne*, Ph.D. thesis, Stellenbosch University, April 2014.

[12] T. Kawabata *et al.*, *2α + t cluster structure in ^{11}B*, Phys. Let. B **646** (2007) 6–11.

[13] H. Horiuchi, K. Ikeda and K. Kato, *Recent Developments in Nuclear Cluster Physics*, Prog. Theor. Phys. Suppl. **192** (2012) 1.

[14] Y. Kanada-Enyo and H. Horiuchi, *Structure of Light Unstable Nuclei Studied with Anti-symmetrized Molecular Dynamics*, Prog. Theor. Phys. Suppl. **142** (2001) 205-263.

[15] T. Neff and H. Feldmeier, *Cluster and Shell Structures in the Fermionic Molecular Dynamics Approach*, Int. J. Mod. Phys. E **17** (2008) 2005-2013.

[16] R.H. Spear, *Static quadrupole moments of first 2^+ states in the 2s-1d shell: A review of experiment and theory*, Phys. Rep. **73** (1981) 369.

[17] M. Freer, *The clustered nucleus – cluster structures in stable and unstable nuclei*, Rep. Prog. Phys. **70** (2007) 2149-2210.

[18] J.P. Ebran *et al.*, *How atomic nuclei cluster*, Letters to Nature **487** (2012) 341-344.

[19] Linear Collider TPC website, http://www.lctpc.org/e8/e57671/, accessed on 11 May 2015.

[20] L. Musa *et al.*, *The time projection chamber for the ALICE TPC,* Nucl. Phys. A 931 (2014) 1152-1157.

[21] A. Breskin *et al.*, *Further Results on the Operation of High-Accuracy Drift Chambers*, Nucl. Instrum. Meth. **119** (1974) 9-28.

[22] Ix-B Garcia Ferreira, J. García Herrera and L. Villasenor, *The Drift Chambers Handbook, introductory laboratory course*, J. Phys. Conf. Ser. **18** (2005) 346-361.

[23] Y. Assran and A. Sharma, *Transport properties of operational gas mixtures used at LHC*, unpublished internal CERN report.

[24] J. Wiechula *et al.*, *High-precision measurement of the electron drift velocity in Ne-CO_2*, Nucl. Instrum. Meth. A **548** (2005) 582-589.

[25] B. Ketzer *et al.*, *A time projection chamber for high-rate experiments: Towards an upgrade of the ALICE TPC*, Nucl. Instrum. Meth. A 732 (2013) 237-240.

[26] J. Alme *et al.*, *The ALICE TPC: A large 3-dimensional tracking device with fast readout for ultra-high multiplicity events*, Nucl. Instrum. Meth. A 622 (2010) 316-367.

[27] Z. He, *Review of the Shockley-Ramo theorem and its application in semiconductor gamma-ray detectors,* Nucl. Instrum. Meth. A 463 (2001) 250-267.

[28] W. Shockley, *Currents to conductors induced by a moving point charge*, J. Appl. Phys. **9** (1938) 635.

[29] S. Ramo, *Currents induced by electron motion*, Proc. I.R.E. (1939) 584.

[30] W. Mittig *et al.*, *Active-target detectors for studies with exotic beams: Present and next future*, Nucl. Instrum. Meth. A **784** (2015) 494-498.

[31] G.F. Grinyer, J. Pancin and T. Roger, *Active Targets and Time Projection Chambers for Experiments in Nuclear Physics*, unpublished.

[32] H. Savajols *et al.*, *MAYA: An active-target detector for the study of extremely exotic nuclei,* Nucl. Instr. Meth. B **266** (2008) 4583-4588.

[33] S.P. Fox *et al.*, *TACTIC: A new detector for Nuclear Astrophysics Experiments,* J. Phys.: Conf. Series **312** (2011) 052007.

[34] Dupont website, http://www.dupont.com/products-and-services/membranes-films/polyimide-films/brands/kapton-polyimide-film.html, accessed on 22 July 2015.

[35] A.M. Laird *et al.*, *Status of TACTIC: A detector for nuclear astrophysics,* Nucl. Instrum. Meth. A **573** (2007) 306-309.

[36] C.A.B. Oliveira *et al.*, *Simulation of VUV electroluminescence in micropattern gaseous detectors: the case of GEM and MHSP*, J. Instrum. **7** (2012) 09006.

[37] C.E. Demonchy *et al.*, *MAYA, a gaseous active target*, Nucl. Instrum. Meth. A **573** (2007) 145-148.

[38] C.E. Demonchy *et al.*, *MAYA: An active-target detector for binary reactions with exotic beams*, Nucl. Instrum. Meth. A **583** (2007) 341-349.

[39] J. Blackmon *et al.*, *Array for Nuclear Astrophysics Studies with Exotic Nuclei*, 2009 workshop presentation, DREB VI: Int. workshop on direct reactions with exotic beams.

[40] M. Matos *et al.*, *The Array for Nuclear Astrophysics Studies with Exotic Nuclei (ANASEN)*, Proc. of 14th Symp. on capture Gamma-ray Spec. (2013) 481-486.

[41] T. Kobayashi *et al.*, *SAMURAI Spectrometer for RI Beam Experiment,* Nucl. Instr. Meth. B **317** (2013) 294-304.

[42] Y. Mizoi *et al.*, *Multiple-sampling and tracking proportional chamber for nuclear reactions with low-energy radioactive isotope beams*, Nucl. Instr. Meth. A **431** (1999) 112-122.

[43] D. Suzuki *et al.*, *Resonant α scattering of ^{6}He: Limits of clustering in ^{10}Be*, Phys. Rev. C **87** (2013) 054301.

[44] M.N. Harakeh and A. Van der Woude, *Giant Resonances: Fundamental High-Frequency Modes of Nuclear Excitation,* Oxford: Clarendon Press; 2001.

[45] T. Yamada *et al.*, *Isoscalar monopole excitations in ^{16}O: α-cluster states at low energy and mean-field-type states at higher energy*, Phys. Rev. C **85** (2012) 034315.

[46] T. Yamada and P. Schuck, *Dilute multi-α cluster states in nuclei*, Phys. Rev. C **69** (2004) 024309.

[47] iThemba LABS K600 website, http://www.tlabs.ac.za/facilities/k600, accessed on 17 June 2015.

[48] R. Neveling, F.D. Smit, H. Fujita and R.T. Newman, *Guide to the K600 Magnetic Spectrometer*, revised edition: 30 July 2014, unpublished.

[49] Private communication, K.C.W. Li.

[50] G.F. Knoll, *Radiation Detection and Measurement*, 3rd ed., John Wiley and Sons Inc., New York (2000).

[51] FreePCB CAD website, http://www.preepcb.com/, accessed on 20 August 2013.

[52] Altium CAD website, http://www.altium.com/, accessed on 15 February 2014.

[53] Private communication, C. van Tubbergh.

[54] D.J. Griffiths, *Introduction to Electrodynamics*, 3rd Edition (1999) 98-103.

[55] Private communication, G.J. Louwrens.

[56] The CERN Garfield website, http://garfieldpp.web.cern.ch/garfieldpp, accessed on 10 June 2013.

[57] The RS components website, http://za.rs-online.com/web/, accessed on 23 October 2014.

[58] Luma metals website, http://www.luma-metall.com/, accessed on 10 June 2015.

[59] Indium corporation website, http://www.indium.com/, accessed on 10 June 2015.

[60] Farnell Material Safety Datasheet website, www.farnell.com/datasheets/1525677.pdf, accessed on 23 March 2015.

[61] Hirose Connectors website, http://www.hirose-connectors.com/connectors, accessed on 22 October 2014.

[62] Lemo website, http://www.lemo.com/lemocusto/catalog/unipole_multipole.pdf, accessed on 17 October 2014.

[63] Science Learn website, http://sciencelearn.org.nz/Contexts/Just-Elemental/Sci-Media/Images/Gold-foil, accessed on 10 May 2015.

[64] Sartorius website, https://www.sartorius.com/en/products/laboratory/laboratory-balances/analytical-balances/, accessed on 05 August 2015.

[65] H. Szczepanowska and W. Wilson, *Permanency of Reprographic Images on Polyester Film,* Journal of the American Institute for Conservation, vol. **39**, No. 3 (1998) Art. 5.

[66] R.J. Southworth-Davies *et al.*, *The Characterisation of Contaminant-free Support Film for MicroPIXE Analysis of Biological Samples*, PIXE 2007 Conf. Proc.

[67] The simNRA website, http://home.rzg.mpg.de/~mam/, accessed on 10 September 2014.

[68] H. Bethe and J. Ashkin, *Experimental Nuclear Physics*, John Wiley & Sons, New York (1953) 253.

[69] M.J. Berger *et al.*, *Stopping-Power and Range Tables for Electrons, Protons and Helium Ions*, NISTIR 4999, ASTAR Program, NIST website, http://www.nist.gov/physlab/data/star/index.cfm, accessed on 30 March 2015.

[70] Mesytec website, http://www.mesytec.com/silicon.htm, accessed on 05 August 2015.

[71] Micron Semiconductor Ltd. website, online catalogue, http://www.micronsemiconductor.co.uk/pdf/cat.pdf, accessed on 28 July 2015.

[72] J.J. van Zyl, P. Papka, R. Neveling *et al.*, Research Proposal to iThemba LABS: *In search of alpha-cluster states in ^{20}Ne at excitation energies above 20 MeV*, September 2013.

[73] M.H. Hablanian, *High-Vacuum Technology: A Practical Guide*, 2nd ed. (1997) 156.

[74] Scientific illustration website, http://www.scistyle.com/, accessed on 20 August 2015.

[75] R. Neveling, *The K600 Magnetic Spectrometer*, 2012 Workshop Presentation, unpublished.

[76] Private communication, R. Neveling.

[77] Wolfram Mathworld website, http://mathworld.wolfram.com/CylindricalCoordinates.html, accessed on 12 August 2015.

[78] The SRIM website, http://www.srim.org, accessed on 20 April 2012.

[79] J.F. Ziegler, *The Stopping Power and Ranges of Ions in Matter*, Pergammon Press, New York (1977).

[80] Sigma-Aldrich website, http://www.sigmaaldrich.com/catalog/, accessed on 14 August 2015.

■ QED